Biophysical cues in breast cancer metastasis and dormancy

vorgelegt von
Dipl. Ing.
Hubert Mordehaï Taïeb
ORCID: 0000-0002-7530-8988

an der Fakultät III - Prozesswissenschaften
der Technischen Universität Berlin
zur Erlangung des akademischen Grades

Doktor der Ingenieurwissenschaften
– Dr.-Ing. –

genehmigte Dissertation

Promotionsausschuss:

Vorsitzende: Prof. Dr. Sina Bartfeld
Gutachterin: Dr. Amaia Cipitria
Gutachter: Prof. Dr. Roland Lauster
Gutachter: Dr. Tom Robinson

Tag der wissenschaftlichen Aussprache: 24.02.2022

Berlin 2022

Zusammenfassung

Das Wiederauftreten von Brustkrebs und die Bildung von Metastasen sind oft mit einer schlechten Prognose verbunden. Die Ausbreitung von Krebszellen in sekundäre Organe ist sehr häufig und die zehnjährige Verzögerung, die beim Wiederauftreten beobachtet wird, ist ein Zeichen für eine Ruhephase, in der die Zellen in einem Wachstumsstillstand verharren, darauf wartend durch einen Auslöser in ihrer Mikroumgebung reaktiviert zu werden. Während der Invasion sekundärer Organe bewegen sich die Zellen durch Kapillaren, die durch Gradienten sowohl im osmotischen Druck als auch im Flüssigkeitsstrom gekennzeichnet sind. Wir stellen die Hypothese auf, dass diese beiden biophysikalischen Faktoren die Ruhephase von Krebszellen beeinflussen könnten, indem sie die Progression des Zellzyklus anpassen.

Daher brauchen wir eine Möglichkeit, die Dynamik des Zellzyklus unter kontrollierten Bedingungen zu überwachen. Dank technisch ausgereifter Systeme wie dem fluoreszierenden ubiquitinierungs-basierten Zellzyklus-Indikator (FUCCI) ist es heute möglich, Zellproliferation, Migration, Veränderungen der Kernmorphologie und die Dynamik einzelner Zellzyklen markierungsfrei und quantitativ in Echtzeit zu untersuchen. Es fehlt jedoch noch eine automatisierte und standardisierte Methode zur Verarbeitung der umfangreichen Datenmenge (Zeitraffer-Multikanalaufnahmen). In dieser Arbeit stellen wir die dafür von uns entwickelte Software vor: FUCCItrack, eine halbautomatische All-in-One-Software zur Segmentierung, Verfolgung und Visualisierung von FUCCI-modifizierten Zelllinien. Eine benutzerfreundliche, vollständig grafische Benutzeroberfläche ermöglicht die Aufzeichnung und quantitative Analyse der kollektiven Zellproliferation, als auch einzelner Zellinformationen, einschließlich Migration und Veränderungen der Zellkern- oder Zellmorphologie in Abhängigkeit vom Zellzyklus. Um eine vollständige Kontrolle über die Analyse zu ermöglichen, enthält FUCCItrack auch Funktionen zur Identifizierung von Fehlern und manuellen Korrekturen. Wir glauben, dass mit dieser Software eine neue Gruppe von

Anwendern, die mit der Bildverarbeitung nicht vertraut sind, von den großartigen FUCCI-Systemen und anderen Zellzyklusreportern profitieren kann.

Als nächstes konzentrierten wir uns auf die Rolle des osmotischen Drucks im Zusammenhang mit der Ruhephase von Brustkrebszellen, wobei wir die Zelllinie MDA-MB-231, die wir genetisch mit FUCCI2 (MDA-FUCCI2) modifiziert haben, als Modell für stark metastasierenden Brustkrebs verwendeten. In der Tat moduliert der osmotische Druck die Vermehrung und den Wachstumsstopp von Bakterien, Hefezellen und Samen. In Geweben erfolgt die osmotische Regulierung über Blut- und Lymphkapillaren und auf der Ebene der einzelnen Zelle spielen Wasser- und Osmoregulation eine entscheidende Rolle. Die Auswirkungen des osmotischen Drucks auf die Dynamik des Zellzyklus einer einzelnen Zelle sind jedoch nach wie vor nur unzureichend bekannt. Ausgestattet mit dem von uns entwickelten Werkzeug untersuchen wir die Auswirkungen des osmotischen Drucks auf die Dynamik des Zellzyklus, das Kernwachstum, die Proliferation, die Migration und die Proteinexpression einzelner Zellen durch quantitative Zeitrafferaufnahmen mit dem FUCCI2-System, einer Variante des ursprünglichen FUCCI-Systems mit anderen Fluorophoren. Die Einzelzelldaten zeigen, dass sich unter hyperosmotischem Stress verschiedene Zellsubpopulationen mit beeinträchtigtem Kernwachstum, verzögertem oder wachstumsgestopptem Zellzyklus und verminderter Migration entwickeln. Dieser Zustand ist bei leichtem hyperosmotischem Stress reversibel. Die Zellen kehren dann zu ihrer normalen Zellzyklusdynamik, Proliferation und Migration zurück. Somit kann der osmotische Druck den reversiblen Wachstumsstillstand und die Reaktivierung von menschlichen proliferativen Zellen modulieren.

Schließlich wollten wir untersuchen, wie metastatische Krebszellen auf eine Flüssigkeitsströmung reagieren, die den Bereich der sinusförmigen Kapillaren nachahmt. Daher beobachteten wir die Auswirkungen einer solchen Strömung und der daraus resultierenden Scherspannung, die aus der numerischen Strömungsmechanik abgeleitet wurde, auf den Verlauf des metastatischen Zellzyklus, die Migration, das Zell- und Kernvolumen sowie die Form. Einzelne FUCCI2-Zellen werden mit einer maßgeschneiderten mikrofluidischen Vorrichtung eingefangen und verschiedenen laminaren Strömungen ausgesetzt. Die quantitative Zeitraffer-Bildgebung mit 2D-Epifluoreszenz- und 3D-Konfokalmikroskopie wird mit FUCCItrack, unserer selbst entwickelten Software, durchgeführt, während die 3D-Zeitraffer-Segmentierung der Zellen und Kerne mit Deep Learning erfolgt, um die Bildverarbeitung zu optimieren.

Wir zeigen, dass auf der Ebene einer einzelnen Zelle eine Erhöhung des Flüssigkeitsstroms zu einer kürzeren S/G2/M-Phase, einer etwas längeren G1-Phase und einem insgesamt kürzeren Zellzyklus führt. Die Zunahme des Flüssigkeitsstroms beschleunigt die Zellmigration, ohne dass eine Vorzugsrichtung in Bezug auf die Stromlinien des Flusses besteht. Die konfokale 3D-Zeitraffer-Bildgebung von MDA-FUCCI2-Zellen zeigt keine signifikanten Auswirkungen des Flüssigkeitsstroms auf das Zell- und Kernvolumen während des gesamten Zellzyklus. Die Formanalyse zeigt jedoch eine leichte Abnahme der Kernausdehnung, die jedoch nicht mit einer Abnahme der Zellausdehnung einhergeht. Insgesamt bieten diese Daten neue Einblicke in die potenziellen Auswirkungen des Flüssigkeitsstroms auf der Ebene der einzelnen Zelle, aber sie liefern keine Beweise dafür, dass der sinusförmige Flüssigkeitsstrom ein biophysikalischer Hinweis ist, der die Ruhephase ermöglicht.

Abstract

Breast cancer recurrence and metastasis are often followed by a poor prognosis. Dissemination of cancer cells to secondary organs is very frequent and the decade delay observed in recurrence is a sign of dormancy, where cells stay in a growth arrested phase, waiting for a trigger in their microenvironment to reactivate them. During the invasion of secondary organs, cells travel through capillaries, which are characterized by gradients in both osmotic pressure and fluid flow. This thesis hypothesizes that these two biophysical factors could influence cancer dormancy by modulating cell cycle progression.

Hence, we need a way to monitor cell cycle dynamics under controlled conditions. Thanks to sophisticated systems, such as the fluorescent ubiquitination-based cell cycle indicator (FUCCI), it is now possible to study cell proliferation, migration, as well as changes in nuclear morphology and single cell cycle dynamics, all label free and quantitatively in real time. However, an automated and standardized method to process the large dataset (time lapse imaging with multiple channels) is still missing. In this work, we introduce the software we developed: FUCCItrack, an all-in-one, semi-automated software to segment, track and visualize FUCCI modified cell lines. A complete user-friendly graphical user interface is presented to record and quantitatively analyze both collective cell proliferation as well as single cell information, including migration and changes in nuclear or cell morphology as a function of cell cycle. To enable full control over the analysis, FUCCItrack also contains features for identification of errors and manual corrections. We believe that with this software, a new slew of users not familiar with image processing could profit from the great FUCCI systems, as well as other cell cycle reporters.

Next, we focused on the role of osmotic pressure in the context of breast cancer cell dormancy using the MDA-MB-231 cell line, which we genetically modified with FUCCI2 (MDA-FUCCI2) as model of highly metastatic breast cancer. Indeed, osmotic pressure modulates proliferation and growth arrest of bacteria, yeast cells, and seeds. In tissues, osmotic regulation takes place through blood and lymphatic capillaries and, at a single cell level, water and osmoregulation play a critical role. However, the effect

of osmotic pressure on single cell cycle dynamics remains poorly understood. Equipped with this new tool we developed, FUCCItrack, we investigate the effect of osmotic pressure on single cell cycle dynamics, nuclear growth, proliferation, migration and protein expression, by quantitative time lapse imaging of single cells using the FUCCI2 system, which is a variant of the original FUCCI, using different fluorophores. Single cell data reveals that under hyperosmotic stress, distinct cell subpopulations emerge with impaired nuclear growth, delayed or growth arrested cell cycle and reduced migration. This state is reversible for mild hyperosmotic stress, where cells return to regular cell cycle dynamics, proliferation and migration. Thus, osmotic pressure can modulate the reversible growth arrest and reactivation of human proliferative cells.

Finally, we aimed to investigate how metastatic cancer cells would react to fluid flow, mimicking the region of sinusoidal capillaries. Hence, we observed the effect of such flow, and its resulting shear stress derived from computational fluid dynamics, on metastatic cell cycle progression, migration, cell and nuclear volume, as well as shape. FUCCI2 cells are trapped to capture single cells using a customized microfluidic device and exposed to different laminar flows. Quantitative time lapse imaging in both 2D epifluorescence and 3D confocal microscopy is performed using FUCCItrack, our own developed software, while 3D time lapse cell/nuclear segmentation is done with deep learning to streamline the image processing. We show that at a single cell level, increase in fluid flow leads to shorter S/G2/M phase, slightly longer G1 phase and an overall shorter cell cycle. Increase in fluid flow accelerates cell migration without any preferential direction with respect to the flow streamlines. 3D time lapse confocal imaging of MDA-FUCCI2 cells reveals no significant effect of fluid flow on cell and nuclear volume throughout the cell cycle. However, shape analysis reveals a slight decrease in nuclear elongation, which is not accompanied by a decrease in cell elongation. Collectively, those data provide new insights into the potential impact of fluid flow at a single cell level but does not support evidence for the sinusoidal fluid flow as a dormancy permissive biophysical cue.

Acknowledgements

First of all, I want to express my deepest gratitude for the great opportunity I had to conduct my doctoral research at the Max Planck Institute of Colloids and Interfaces (MPICI) as an IMPRS fellow. I really enjoyed my time spent in this scientific and friendly atmosphere that I already knew from my previous experience as an intern with Prof. John Dunlop and afterwards as a master student with Dr. Michaela Eder.

I would like to thank Dr. Amaia Cipitria (first supervisor) and Dr. Tom Robinson (second supervisor) for providing this excellent research subject that I took great pleasure to dive into for the last three years, as well as their valuable guidance, advice and support.

I want to thank Prof. Roland Lauster from TU Berlin, who accepted to take me as a student for the doctoral procedure. I also would like to thank Prof. Peter Fratzl, Prof. Emanuel Schneck and Dr. Luca Bertinetti for being part of my mentoring committee. Discussing with you always was beneficial and greatly improved the quality of my research throughout the years and is reflected in this thesis.

More specially with you Amaia. I feel so grateful for the immense amount of trust, rigor, freedom and time you gave me during my research. You always had an open ear to discuss the so many (yes, way too much) questions and ideas that came on our way, and you always let me pursue them at my will while providing a safe place in parallel. You always dedicated your time, brain and energy to teach me, improve, revise and strengthen my research while being so patient with me, and I am glad that you did. It is undeniable that without your unconditional help, this thesis and all the work inside would have never been as good as it is now.

I thank you so much too, Tom. As you know, we already had some scientific exchanges before I applied for the IMPRS since you helped me with my first internship at the MPICI. I thus knew when I applied that I will be working with a trustworthy person, honest and always keen to help and it gave me great confidence to take part in this amazing experience that is a PhD. Your knowledge and expertise for the microfluidic and confocal imaging, as well as your scientific rigor and sharp eye was crucial to the success of this thesis, and I thank you for that too. Being a member of your group in a

completely different department at the MPICI always was a really great experience since it opened my scientific horizons and allowed me to meet incredible people.

Looking back, I thank the numerous helpful discussions and amazing teamwork with all the current and former members of my two groups in the Biomaterials and Theory & Bio-Systems department. Especially I would like to thank Daniela who was always there to help me with the FUCCI and Sarah who helped me to understand (or at least learn) the different aspects of the biology in my project in more detail. I also thank you Sarah for being so thorough while being partner in crime for PhDNet and sharing some ideals of scientific integrity with me. Of course, I thank you Sadra for helping me with the cell work and all the many discussions we had about the FUCCI among other topics. It is mainly thanks to you that I had a glimpse of science collaboration from inside and outside the institute and I thank you for this. I also thank you Anna-Dorothea, Nicky and Claudia, Vikki, Di, Inés and all members of the Biomicrofluidic systems group, especially Julia who helped me so much while learning the wafer and microfluidic preparation, Tina for always being there in case I needed help and Sunidhi for being such a nice and fun person to be around.

An immense thank you goes to Christine who taught me literally everything I know about cell culture and working properly with biological samples in the lab. You are so knowledgeable, down to earth and a great person to rely on!

I'd further like to thank the people from the mechanical workshop, especially Jan for helping me with the development of my custom-made holder for the microfluidic experiments. I also thank very much René Genz and Paul Meißner from the IT for their unconditional help and many discussions, often late in the evening. I am really grateful to Silke and Annette from the library for always being present when I needed them and their work to discuss open science in the institute.

Many thanks go to so many current and former members of the Biomaterials department with whom I now shared almost 5 years of my life. My sincere gratitude goes to my office mates Sebastian, Jessica, Daniel, Adrien, Anna-Dorothea and Charlett. My dearest friend Anna-Maria I cannot imagine this adventure without you, I thank you for the amazing times we had after work and in other countries. I also warmly thank my amazing penguin friend Guillaume, who came to work with me for three months at a moment when I truly needed a friend.

I would like to thank my parents, brother and sisters as well as nephews and nieces who helped me go through this period of my life.

Last but not least, I want to thank Yves Bréchet, who gave me the opportunity to follow one of my dreams by coming to the MPICI 5 years ago for the first time.

Contents

List of figures

List of publications

Publications as first author originating from this thesis

1) Hubert M. Taïeb, Daniela S. Garske, Jörg Contzen, Manfred Gossen, Luca Bertinetti, Tom Robinson & Amaia Cipitria. Osmotic pressure modulates single cell cycle dynamics inducing reversible growth arrest and reactivation of human metastatic cells. *Scientific Reports* **11,** 13455 (2021). 10.1038/s41598-021-92054-w. Incorporated as part of Chapter 4.

H.M.T., L.B., T.R. and A.C. conceived the idea and designed the experiments. H.M.T. performed the experiments. D.S.G., J.C. and M.G. performed the FUCCI2 genetic modification. H.M.T, L.B., T.R. and A.C. analyzed and discussed the data. H.M.T. and A.C. wrote the manuscript.

2) Hubert M. Taïeb, Luca Bertinetti, Tom Robinson & Amaia Cipitria. FUCCItrack: an all-in-one software for single cell tracking and cell cycle analysis. *PLOS one.* **Currently under review**. Incorporated as part of Chapter 3.

H.M.T. and A.C. conceived the idea and designed the experiments. H.M.T. performed the experiments. H.M.T. wrote the source code and designed the software. H.M.T and A.C. wrote the manuscript. T.R. and L.B. discussed the software and the results.

3) Hubert M. Taïeb, Guillaume Herment, Tom Robinson & Amaia Cipitria. Effect of sinusoidal capillaries fluid flow and shear stress on single cancer cell cycle dynamics, migration, volume and shape. Lab on a chip, special issue “AI in Microfluidics”. **Currently in preparation.** Incorporated as part of Chapter 5.

H.M.T., T.R. and A.C. conceived the idea and designed the experiments. H.M.T. performed the experiments. H.M.T. and G.H. designed the simulation workflow. H.M.T, T.R. and A.C. analyzed and discussed the data. H.M.T. and A.C. will write the manuscript.

Publications during the candidature as a result of collaboration with other related projects

1) Sadra Bakhshandeh, Hubert M. Taïeb, Raimund Schlüßler, Kyoohyun Kim, Timon Beck, Anna Taubenberger, Jochen Guck and Amaia Cipitria. Optical quantification of intracellular mass density and cell mechanics in 3D mechanical confinement. *Soft Matter* **17**, 853–862 (2021). doi.org/10.1039/D0SM01556C.

H.M.T. participated to the experiments and wrote the MATLAB code for image processing and data analysis.

2) Sadra Bakhshandeh, Hubert M. Taïeb, Adithi R. Varadarajan, Sarah M. Hücker, Xin Lu, Daniela S. Garske, Sarah A. E. Young, Jörg Contzen, Manfred Gossen, Stefan Kirsch, Jens Warfsmann, Kamran Honarnejad, Christoph A. Klein & Amaia Cipitria. Quiescence-inducing 3D-engineered matrix uncovers drug protective signaling pathway of dormant cancer cells. *Nature Materials.* **Currently submitted.**

H.M.T. wrote the MATLAB code for image processing and data analysis.

3) Sarah A. E. Young, Maximilian Rummler, Hubert M. Taïeb, Daniela S. Garske, Agnes Ellinghaus, Georg N. Duda, Bettina M. Willie & Amaia Cipitria. *In vivo* microCT based time lapse morphometry reveals anatomical sites-specific differences in bone (re)modeling serving as baseline measures to detect early pathological events. **Currently in preparation for resubmission.**

H.M.T. helped to adapt an already existing MATLAB code for data analysis.

4) Agnese Codutti, Mohammad A. Charsooghi, Elisa Cerdá-Doñate, Hubert M. Taïeb, Tom Robinson, Damien Faivre & Stefan Klumpp. Single-cell motion of magnetotactic bacteria in microfluidic confinement: interplay between surface interaction and magnetic torque. *eLife.* **Currently under revision.**

H.M.T. wrote a MATLAB code for imaging processing of the magnetotactic bacteria.

List of appendices

Chapter 1 Background and significance

"The seeds are invisible. They sleep in the secret of the earth
until one of them takes a fancy to wake up."

Le petit prince, Antoine de Saint-Exupéry

This chapter gives an overview of the necessary concepts to understand this thesis as well as a review of the current literature. The chapter describes the motivation to investigate breast cancer metastasis and specifically, cellular dormancy, with a focus on the interaction with the microenvironment and the biophysical cues associated with it.

1.1 Breast cancer metastasis, dormancy and biophysical cues

Despite the immense effort, resources and scientific progress in the last decades, most cancer deaths can be attributed to metastases [1]. Tumor metastasis entails a suit of specific biological processes that ultimately disseminate tumor cells from a primary site to a distant location [2]. Tumor cells must invade surrounding tissue from the primary tumor, escape to the lymphatics or the bloodstream (intravasation), survive until they physically arrest somewhere to extravasate into a tissue and finally grow at the new site (Figure 1-1) [3]. Recurrence is often observed for breast cancer, both with (41 %) and without treatment (54 %) and even after the surgical removal of the primary tumor [4]. Bone is among the preferred target sites for metastasis in advanced breast cancer and is rarely curable occurring for more than with 70 % of patients with metastatic breast cancer [5, 6].

Interestingly, the recurrence is extremely variable in time with a delay ranging from months up to decades after initial primary tumor removal [4], and with rare recurrence after 25 years [7]. The term dormancy was coined to describe the state of non-proliferation of disseminated tumor cells (DTCs) maintained by different pathways [8-10]. In particular, cellular dormancy corresponds to a reversible growth arrest strongly regulated by the interaction of isolated DTCs with their microenvironment [9, 11].

Indeed, dormancy permissive locations in the body, or niches have been found to restrain tumor growth or induce dormancy [12], such as the perivascular region in the case of breast tumor dormancy [13]. Preclinical models are now targeting specifically this step of the metastatic process to understand how dormant cells avoid classical therapy [14] since the years before recurrence offer a therapeutic window to avoid or delay clinical detectable metastasis. Other translational approaches are to target signaling pathways that could maintain a dormant state [15] or, in contrast, to develop synthetic lethal drugs to target dormant tumor cells [16].

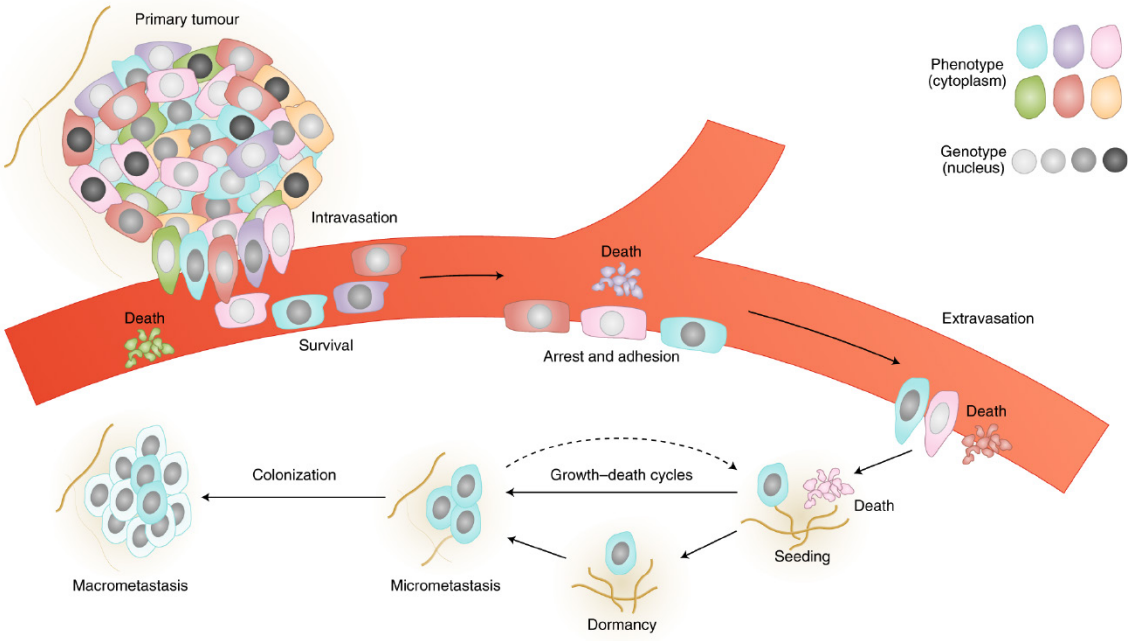

Figure 1-1 The metastatic progression of cancer.

Reproduced with permission from Springer Nature.

It is fascinating to note that more than a hundred years ago, Stephen Paget described the tumor cells as the “seed” and the host environment as the “soil” and hypothesized that their interaction could determine metastatic outcome [17]. Understanding the homing to a new microenvironment and how this new biophysical soil contributes to progression of cancers (particularly breast cancer) is of great importance and has been documented before [13, 18-20]. It was thus shown that microenvironmental conditions such as upregulation of signaling factors like transforming growth factor (TGF)-βII [21], interferon-γ [22], or bone morphogenetic protein 4 (BMP4), as well as BMP7 [23] were involved in cancer dormancy. Today more than ever, understanding the

microenvironment and its impact on cellular dormancy to prevent metastasis occurrence remains an ongoing challenge that is being tackled by many researchers [10]. Even though It is not yet completely clear how DTCs can use ECM-derived cues to trigger dormancy, and eventually maintain it upon reactivation, recent work discovered that dormant cancer cells can build a type III collagen-enriched ECM niche to sustain tumor dormancy [24].

Despite the staggering amount of literature on biochemical on dormancy, very little is known about the impact of the different biophysical cues in breast cancer cell dormancy. It has been shown that increased hypoxia from the primary tumor could trigger a dormant phenotype [25] and create a subpopulation of dormant DTCs evading therapy, eventually leading to cancer relapse. Investigation on other cues such as osmotic pressure or fluid flow and their role in cellular dormancy remains unexplored.

However, the role of the local biophysical microenvironment in cellular function and processes has been increasingly acknowledged. Beyond genetically driven intracellular factors, biophysical cues regulate cell metabolism, growth arrest and proliferation [26-28]. It has been shown that compressive mechanical force inhibits spheroid growth due to volume constraints [29]. At a single cell level, mitotic cells in three dimensional (3D) microenvironments generate protrusive forces that deform the ECM, and failure to do so arrests mitosis [30]. For this reason, the deformability and viscoelastic properties of the 3D confining matrices play a key role on cell cycle progression, whereby fast stress relaxation favors cell cycle progression and spheroid growth [31]. Stiffness of the ECM, topography and biomechanical force have gained traction in the recent years for their role in modulating fundamental cell properties, such as cell fate, self-renewal, motility or homing [32].

Other cues such as osmotic pressure can modulate proliferation and growth arrest of diverse organisms such as bacteria [33], yeast cells [34], and seeds [35, 36]. Moreover, in tissues, osmotic regulation takes place through blood and lymphatic capillaries which are also important cell niches likely to harbor non-cycling quiescent stem cells [37, 38]. Thus, how osmotic regulation affects breast cancer cell dormancy is yet to be discovered (please refer to the introduction of Chapter 4 for more details).

One other important aspect of metastasis and dormancy is the ability of DTCs to resist a large range and variation of fluid flow and shear stress when passing through blood vessels or the lymphatic system before extravasation [39] (Figure 1-2). Especially, extravasation of DTCs occurs mainly in capillaries which are regions that permits cell

physical arrest, and this can be by mainly two ways. Firstly, DTCs can arrest by occlusion (Figure 1-2A1), but potentially causing cell cluster squeezing (Figure 1-2A2), or they can actively adhere with endothelial cells (Figure 1-2B). These arrested cells will suffer from an increased levels of shear stress that can cause cell fragmentation (Figure 1-2C) and an alteration of the vessel permeability. Subsequently, several extravasation alternatives are possible. Cancer cells could pass through the walls of the blood-vessels without visible rupture, thus undergoing diapedesis (Figure 1-2D), be extruded through flow-dependent endothelial remodeling (Figure 1-2E) or stay and divide to form intraluminal metastases (Figure 1-2F). After extravasation, certain cancer cells will remain dormant for years to decades (Figure 1-2G). Please refer to the introduction of Chapter 5 for more details.

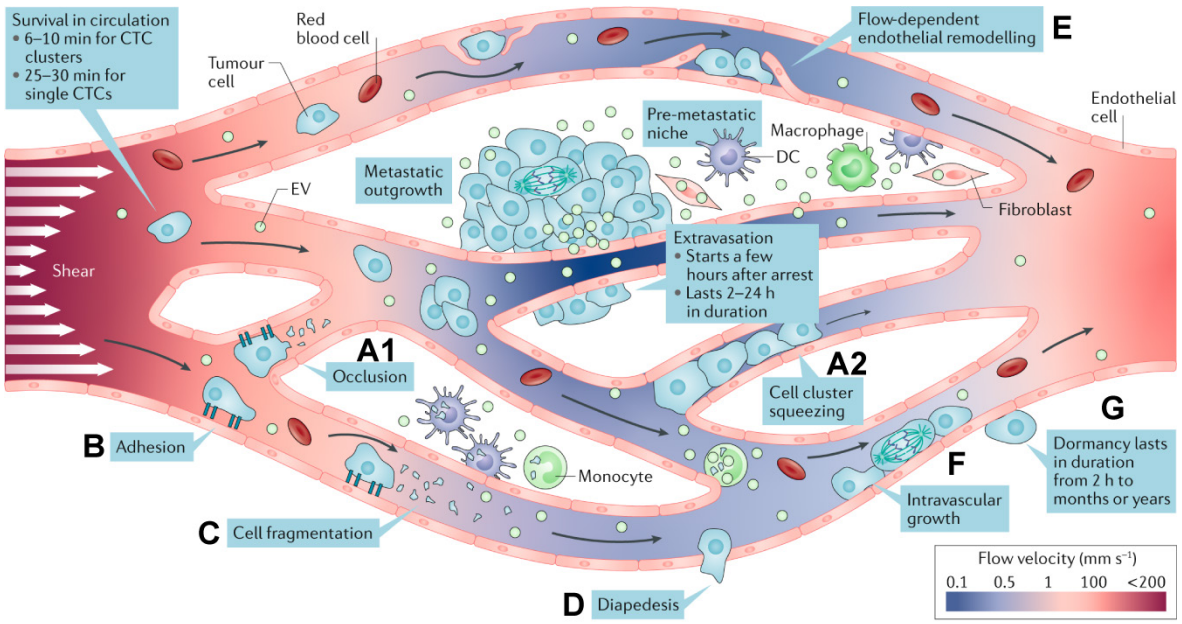

Figure 1-2 Tumor cell extravasation is a flow-dependent process.
Reproduced [39] with permission from Springer Nature.

From the primary tumor site to the metastatic niche, DTCs go through a cascade of changes in the environment that surrounds them. In this thesis, we focus on two biophysical cues, namely: osmotic pressure and fluid flow and we investigate their impact on cell cycle progression and dormancy.

1.2 FUCCI (Fluorescent Ubiquitination-based Cell Cycle Indicator)

Real time analysis of cell cycle dynamics in proliferating cells has proven difficult in the past because common cell markers such as 5-ethynyl-2'-deoxyuridine (EdU), PCNA or Ki67 require fixation of the sample and rely on immunofluorescent stainings [40]. Several cell cycle reporters emerged in the last decade [41-47] to monitor in real time cell cycle phases and partially address the sample fixation requirement. In this section, we focus on reviewing what are the common cell cycle reporters and introducing FUCCI, the most promising one [48], that is at the center of our work.
In this thesis, FUCCI can refer to the FUCCI technology in general or the original FUCCI reporter, and FUCCI2 to a sub type of FUCCI, used for this work.

1.2.1 Common cell cycle indicators

Several methods have been developed to see and determine the cell cycle status using fluorescent proteins. Observing mitotic cells in real time has proven possible thanks to functional nuclear proteins such as histone H2B attached to green fluorescent protein (GFP) [41]. Building on this construct, red fluorescent protein (RFP) was tagged to cytoplasmic proteins by others, to monitor the nuclear and cytoplasmic interaction during mitosis [43]. This improvement over the initial histone H2B provided more information but still lacked the potential to resolve cell cycle phases. Nuclear localization signal (NLS) was then used to visualize the cell cycle transition from G1 phase to S phase in real time [42, 47]. To resolve the S to G2 phase in real time, PCNA linked to fluorescent proteins was used in further approaches [44, 46]. Förster or fluorescence resonance energy transfer (FRET) sensors have also been coupled to cyclin-dependent kinases (CDKs) to monitor cell cycle transition [45]. One common characteristic of all the above-mentioned methods is that they allow visualization of parts of the cell cycle, but never the whole cycle in real time.

1.2.2 FUCCI history

Only in the last decade has the FUCCI system emerged [49], which allows imaging of cell cycle dynamics by visualizing individual G1 and S/G2/M phases both *in vitro* and *in vivo*, in real time and without external label [50-52]. This enables a wide range of studies aimed at understanding cell behavior in more depth such as cell deformability and proliferation as a function of cell cycle dynamics [53] or tumor spheroid growth

within compliant vs. stiff hydrogels [54]. Additionally, mathematical models of FUCCI systems are created to relate cell migration [55] or tumor spheroid formation [56] with cell cycle dynamics. The original FUCCI probe used mKO2-hCdt1 (30/120) for the G1 phase and mAG-hGeminin (1/110) for the S/G2/M phase [49]. This was later improved with the FUCCI2 cell cycle reporter, which employed mCherry-hCdt1 (30/120) for G1 and mVenus-hGeminin (1/110) for S/G2/M phase (Figure 3-4A) [57]. FUCCI2 offers enhanced contrast and the possibility to spectrally distinguish the signals from the widely used fluorophore GFP for applications such as parallel monitoring of protein subcellular localization and/or signaling events [57]. However, FUCCI or FUCCI2 cannot be used to separate the cells in the G0 phase from those in G1 since Cdt1 is thought to be expressed in both phases [49]. This led to the development of new systems adding to the original FUCCI system, whereby cells in the G0 phase were separated from those in G1. This construct used mVenus-p27K$^-$ for G0, mCherry-hCdt1 (30/120) for G1 and AmCyan-hGem (1/110) for S/G2/M [58]. Other groups also developed FUCCI4, a set of four fluorescence indicators that could resolve independently every single phase of the cell cycle (G1, S, G2 and M) [59], which traditional FUCCI or FUCCI2 could not separate. To the best of our knowledge, FUCCI is the most useful and complete tool to visualize all phases of the cell cycle dynamics in real time [60].

1.3 Imaging techniques & artificial intelligence

1.3.1 Epifluorescence microscopy

Epifluorescence microscopy (EM), also referred as wide-field fluorescence microscopy (WFM), is one of the most frequently used techniques in cell biology. It is similar to conventional light microscopy but with additional specific features suitable for fluorescence imaging. In EM, both the illuminated and emitted light are traveling through identical objective lens. The source (mercury lamp or more recently LEDs) passes through an excitation filter which only allows a band of wavelength corresponding to the excitation wavelength of the fluorophore. The illuminated light (high intensity) then passes through the objective lens, illuminates the sample and excites the fluorophore in the sample that would subsequently emit light (weak intensity). This emitted light travels back to the objective lens and through a dichroic mirror, whose purpose is to separate the high intensity illuminated light from the weak

intensity emitted light. The emission filter then ensures that only the wavelengths emitted from the specific fluorophore pass through. This then reaches the camera where an image is captured. This setup ensures the darkest background for fluorescence imaging to obtain the best contrast image from the emitted light. EM are usually cheaper and more accessible than more advanced techniques such as confocal microscopy but have the disadvantages of collecting light from many focal planes.

1.3.2 Confocal microscopy

Confocal microscopy (CM) has been developed to overcome the limitations of conventional EM. CM eliminates the out of focus light and therefore improves the 3D sectioning capabilities compared to wide-field microscopy [61]. Laser scanning confocal microscopy (CLSM) is a common CM configuration based on point illumination. It generates images by scanning a focused laser beam inside the specimen and rejecting out of focus light by using a pinhole, thereby collecting only information from the focal area and increasing axial resolution. The resulting two-dimensional (2D) sections of multiple depths are combined to create a 3D image, often also referred to as z-stack. As a limitation, the optical arrangement of rejecting out of focus light and hence detecting only a portion of the emitted light ultimately can lead to excessive photo bleaching or even photo toxicity on living cells [61].
The spatial resolution of a confocal microscope depends on the numerical aperture (NA) of the objective, the size of the pinhole and the wavelength of the excitation light. The axial resolution of a confocal fluorescence microscope is lower than along the lateral direction due to diffraction. However, diffraction can be reduced using objective lenses with high NA at the expense of shorter working distances.

1.3.3 From imaging to automatic segmentation

The impressive advances in imaging techniques and fluorescent probes recently shaped a new area in biological sciences where researchers can access temporal and spatial variations in living organisms. Dynamic measurements are now possible in living cells in real time ranging from single molecules [62] to multi-channel fluorescent probes such as FUCCI [49], and for an extended periods of time *in situ* [63]. In parallel to the technological improvements and higher number of dimensions imaged (2D, 3D and 3D time lapse), there is an increasing demand in the field of image analysis to

quantify these large data sets. Image segmentation is a task defined by an identification of parts of an image corresponding to a distinct feature or object such as the nucleus or the cell membrane in living cells.

Recently, image segmentation in living science has been well performed by deep learning techniques where classical imaging processing methods sometimes showed their limits. In addition, the recent technological improvement of hardware and software have dramatically improved deep learning (DL) performance and training time [64].

Deep learning is a type of machine learning in which a mathematical model or “neural network” with many parameters is being optimized to perform classification tasks directly from images, text or sound. When applied to images, deep learning algorithms can be used to extract certain features of the original image in what is called semantic segmentation. The term "deep" refers to the number of layers in the mathematical model or network - the more layers, the deeper the network. A layer is a group of different mathematical functions (linear or not) that are being applied to an image to extract features presented during the training of the network. The layers are interconnected via nodes with each layer using the output of the result from the mathematical operation of previous layers as its input.

Convolutional neural networks (CNN) are often used for image recognition because of their performance [65]. In these networks, individual nodes are sensible only in a restricted region of the total image (receptive field), which means the image is divided in patches for feature extraction. Moreover, the receptive fields of diverse nodes partially overlap such that they cover the entire image.

A CNN needs to be trained (please see the section 5.2.8 for more details on training of our network). Briefly, users present to the DL algorithm two inputs. One is the raw images such as fluorescence images that contains spatial features such as a nucleus, or a cell membrane. The second is a binary image that corresponds to the segmentation of the raw image for the targeted feature (called ground truth and often obtained manually). Initially, the DL algorithm will run the raw image through the untrained network and compare the output which is the segmentation with the ground truth. An optimization function is then used to modify the parameters of the network to reduce as much as possible the difference between the output segmentation and the ground truth (the training).

Many of researchers in the field of biology and biomedical imaging now use the neural network U-net [66, 67] because of its excellent segmentation result with only few initial images needed for training [68-70].

Chapter 2 Objectives and thesis structure

"I am nothing, I know, but I compose my nothing with a little piece of everything."

Le Rhin – Lettres à un ami, Victor Hugo

The overall goal of this work is to elucidate the role of biophysical cues, in particular osmotic pressure and fluid flow, on cell cycle progression in the context of breast cancer dormancy and metastasis. This thesis has three specific objectives.

The **first goal** is to provide an open-source software for analysis of cell cycle reporters, FUCCItrack, which includes a graphical user interface to make it accessible to the highest number of researchers. It is meant to provide an efficient, reliable, standardized and automatic way to analyze quantitatively time lapse images. This is covered in the **third chapter,** which begins with a summary of the functionality and then presents the results that can be obtained with FUCCI time lapse cell culture experiments. The Appendix A includes a complete user guide of the software.

Every chapter contains its own introduction, methods, results, discussion and limitation section.

The **second goal** is to use this software to investigate the behavior of metastatic breast cancer cells under two biophysical cues, osmotic pressure and fluid flow, and discover their influence on breast cancer dormancy. This is described in the **fourth chapter**, which documents the effect of osmotic stress on breast cancer cell behavior using quantitative FUCCI2 time lapse imaging on collective and single cell. In the **fifth chapter**, we present our approach to use a microfluidic device along with computational fluid dynamics (CFD) to study the interaction of breast cancer cells with fluid flow. Using FUCCI2 time lapse imaging in 2D, the first part explores the effects of single cell cycle dynamics and migration. With FUCCI2 time lapse imaging in 3D, the second part focuses on time-resolved volume and shape dynamics analysis of the cell and the nucleus under flow.

Finally, the **third goal** of this thesis is to provide evidence that new deep learning methods and 3D confocal microscopy, coupled with an automated simulation

framework, can be beneficial to produce a more accurate model of mechanical stress impacting breast cancer cells under flow. This is described in the **fifth chapter**.
The thesis ends with the **sixth chapter** that is a summary and final discussion of the main results and an outlook towards possible future directions.

Chapter 3 FUCCItrack: one software to track them all

"One ring to rule them all, one ring to find them, one ring to bring them all and in the darkness bind them."

The Fellowship of the Ring, J. R. R. Tolkien

All the work presented in the thesis takes advantages of the FUCCI2 system. Because there is a lack of automated tools to process FUCCI/FUCCI2 related data, the following chapter is intended to provide an overview on the software that was developed for the analysis of quantitative FUCCI2 time lapse imaging. We introduce FUCCItrack, an all-in-one, semi-automated software to segment, track and visualize FUCCI2 modified cell lines. A complete user-friendly graphical user interface (GUI) is presented to record and quantitatively analyze both collective cell proliferation as well as single cell information, including migration and changes in nuclear or cell morphology as a function of the cell cycle status. To enable full control over the analysis, FUCCItrack also contains features for identification of errors and manual corrections.

3.1 Introduction

Conventional cell tracking used to be a manual task [71], with users needing to select each cell at a time, frame by frame. This approach was inherently time consuming, especially when looking at long time lapse imaging, and prone to different bias, due to subjective definition of the center of the cell or user inconsistencies. More recently, many platforms proposed automatic single-cell tracking with different technical solutions [72], both from an open-source initiative on FIJI (ImageJ) or other platforms [73-75], and from proprietary software. These tools are useful to track cell migration, however, they often cannot handle cell division in a consistent, user-independent manner. This may result in incorrect tracking of daughter cells, without the possibility to inspect, edit or adjust the tracking.

This is where the FUCCI cell cycle reporter has an extraordinary benefit with respect to simpler live cell staining. During the G1 phase, only the fluorophore mCherry-Cdt1

(30/120) is expressed. Expression of the fluorophore mVenus-hGeminin (10/110) inside the nucleus indicates the beginning of the S/G2/M phase (Figure 3-4A). Indeed, by expressing first the fluorophore mCherry then mVenus, it provides a defined pattern to track single cells and stop the tracking when the intensity for mVenus drops due to the cell division. This not only allows monitoring of the cell cycle dynamics, but also tracking cell migration parameters such as trajectory and velocity, as a function of cell cycle state, in a single setup and in real time [63]. Paradoxically, this benefit can also turn into a disadvantage, since it means that the fluorophore used for tracking does not have a constant intensity over time for each cell. Alternating fluorescence channels (mCherry/mVenus) with an inherent intensity variability make traditional automatic image processing more complicated to implement.

To the best of our knowledge, only three software solutions have been reported to treat FUCCI time lapse datasets in an automatic or semi-automatic way [76-78]. One is not publicly available [78], one requires multiples applications to be run (Fiji and Columbus) [77], and the latest one was released recently on MATLAB [76]. The latter can perform migration analysis and includes a FUCCI plug-in to extract nuclear intensity and obtain cell cycle duration. However, the software is focused on tracking cell migration and does not perform any segmentation of the nucleus or cell shape. It also does not use the full potential of the FUCCI system to automatically detect cell division since the tracking is independent from the FUCCI intensity. In addition, it is impossible to extract collective cell proliferation parameters such as number of cells over time and remains targeted to single cell behavior only. FUCCItrack allows users to perform rapid and efficient automatic nucleus segmentation, as well as cell shape segmentation if an additional fluorophore is used, to then investigate cell cycle dynamics, proliferation, migration and morphology as a function of time and cell cycle state.

3.2 Materials and methods

3.2.1 FUCCI2 cell line generation

Lentiviral particle production

Lentiviral vectors mCherry-hCdt1(30/120)/pCSII-EF-MCS (DDBJ/EMBL/GenBank, AB512478) and mVenus-hGeminin(1/100)/pCSII-EF-MCS (DDBJ/EMBL/GenBank, AB512479) were purchased from the Riken Brain Science Institute, Japan (Dr. Atsushi

Miyawaki, head of provider laboratory, and Dr. Hiroyuki Miyoshi, developer of pCSII-EF-MCS). Lentiviral particles were generated by co-transfection of HEK-293TN cells (System Biosciences) with mCherry-hCdt1(30/120)/pCSII-EF-MCS or mVenus-hGeminin(1/100)/pCSII-EF-MCS lentiviral vectors, alongside the packaging plasmid psPAX2 (Addgene plasmid, #12260) and the envelope plasmid pMD2.G (Addgene plasmid, #12259). The culture supernatant was collected and concentrated by ultracentrifugation at 22 000 rotation per minute (RPM) for 3 h (Beckman L7-55 with SW32Ti rotor) at 4°C. The virus titer was estimated by transduction on HeLa cells and subsequent flow cytometric analysis for fluorescent protein expression. This work was done in collaboration with Manfred Gossen and Jörg Contzen at the Charité University Hospital Berlin.

Lentiviral transduction and generation of MDA-FUCCI2 and MCF7-FUCCI2 cells

Human metastatic breast cancer cells MDA-MB-231 (ATCC, #HTB-26) and MCF7 (#HTB-22) with the FUCCI2 reporter (MDA-FUCCI2 and MCF7-FUCCI2, respectively) were used during this thesis. MDA-FUCCI2 and MCF7-FUCCI2 cells stably expressing FUCCI2 reporters mCherry-hCdt1 (30/120) (red fluorescence) and mVenus-hGeminin (1/110) (green fluorescence) were obtained as follows. Parental cell lines MDA-MB-231 and MCF7 were sequentially infected with lentiviral particles containing mVenus-hGeminin (1/110) at a multiplicity of infection (MOI) of six (MDA-MB-231) or five (MCF7), followed by mCherry-hCdt1 (30/120) at a MOI of three. Successfully transduced cells were identified by expression of mCherry, mVenus or simultaneous mVenus and mCherry fluorescence, sorted with a FACSAria^{TM} II flow cytometer (Becton Dickinson) and expanded for *in vitro* experiments. This work was done in collaboration with Manfred Gossen and Jörg Contzen at the Charité University Hospital Berlin.

Characterization MDA-FUCCI2 vs. MDA-MB-231 parental cell line

At the MPICI, we performed characterization of MDA-FUCCI2 vs. parental cell line MDA-MB-231 (Figure 3-1) to verify that the genetic modification did not significantly change cell attachment, migration and proliferation. For the cell migration assay, two-chambered silicone cell culture inserts (Ibidi, #80209, area of 0.22 cm^2 per chamber) were placed in a 24 well plate (Thermo Fischer, #142475). Both MDA-FUCCI2 and MDA-MB-231 were seeded with a density of 50 000 cells in a total volume of 70 µL media. Cells were allowed to adhere for 5 h before the silicone chamber was removed

to create a reproducible cell-free area of 500 ± 50 µm (Figure 3-1D). Non-adherent cells were washed away by rinsing once with media. Afterwards cells were incubated in 2 mL media and the gap closure was monitored for 20 h using an inverted microscope (Zeiss AxioObserver 7, 10x objective) with a live cell imaging system (Okolab, UNO-T-H-CO2). The cell-free gap area was quantified in percent of the initial cell-free gap area using MATLAB (Figure 3-1B). To assess cell proliferation kinetics, 38 000 cells in 2 mL media were seeded in 24 well plates and the number of cells at days 1, 2, 3 and 4 were quantified (Figure 3-1C) using a cell counter (Scepter™ 2.0, Millipore). Finally, to determine cell attachment, the same Ibidi inserts were used. Both cell types were seeded with a density of 2200 cells in 70 µL and imaged directly after seeding using the same inverted microscope for a duration of 4 h. A custom-made MATLAB code was used to count round cells (Figure 3-1A), corresponding to suspended cells before they adhere. No significant differences were found between the generated MDA-FUCCI2 and the MDA-MB-231 parental cell line regarding cell attachment, migration and proliferation.

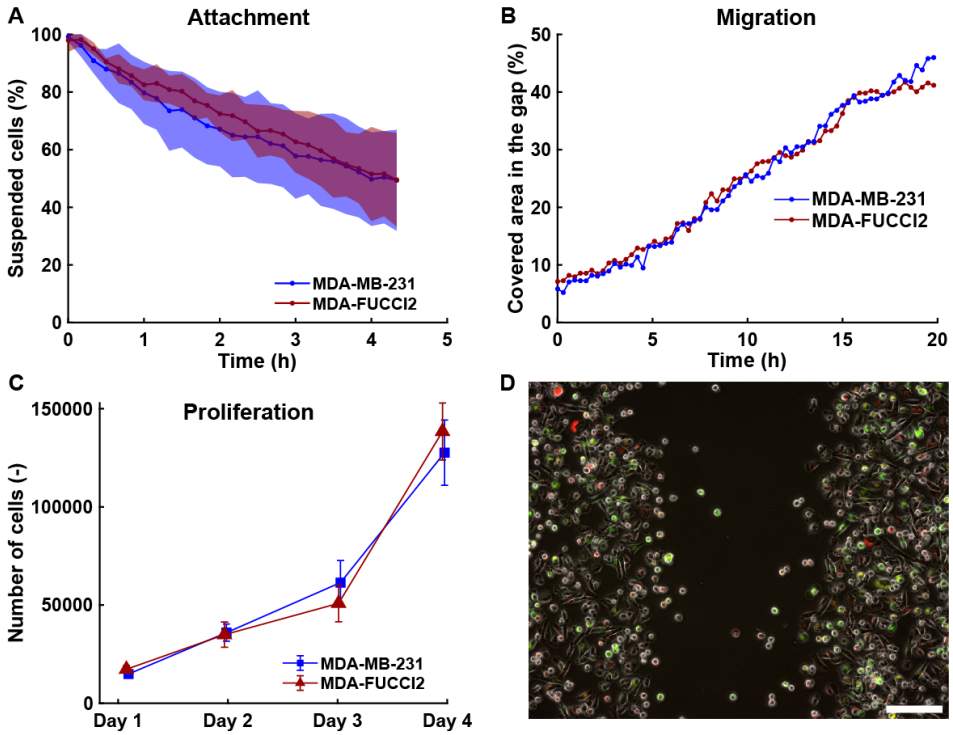

Figure 3-1 Characterization of MDA-FUCCI2 vs. MDA-MB-231 parental cell line. (**A**) Attachment assay where cells were seeded in a closed compartment and imaged for 4 h every 30 minutes (N = 4 wells). Initially (t = 0 h), all cells were round and in suspension and, with time, the number of suspended cells decreased as they

attached and spread on the bottom of the well. (**B**) Wound healing assay showing the coverage of the gap created by the Ibidi inserts as a function of time. (**C**) Proliferation assay, representing the number of cells as a function of time, measured with a cell counter (N = 6 wells for each group). (**D**) Fluorescent image representing the beginning of the migration assay (t = 0 h), scale bar is 200 µm. Data in **A** and **C** are mean ± standard deviation.

3.2.2 Cell culture

MDA-FUCCI2 and MCF7-FUCCI2 were cultured in low glucose Dulbecco's modified eagle's medium (Sigma, #D6046) supplemented with 1 % penicillin/streptomycin (Gibco, #15140-122, 10^4 units/mL of penicillin and 10 mg/mL of streptomycin) and 10 % fetal bovine serum superior (Sigma, #S0615). MCF7-FUCCI2 were additionally supplemented with 0.1 % insulin (Sigma, #I2643-50MG). They were grown at 37 °C with 5 % CO_2 on Nunc™ 100 x 17 mm petri dishes (Thermo Fischer, #150350) with regular passaging. The cell line MDA-MB-231 is a mutant p53 cell line, whereas MCF7 is a wild-type p53 cell line [79].

3.2.3 Cell actin staining

Some experiments were performed using the SiR-Actin Kit (Spirochrome, #SC-001) which is a live F-actin cell staining. Briefly, after passaging a 1000 µL cell suspension of 600 000 cells/mL was incubated in a 1.5 mL Eppendorf for 6 h with the cell culture media containing the SiR-Actin at a concentration of 100 nmol/L. The cell suspension was mixed every 1.5 h. Cells were then seeded for experiments with the media containing the SiR-Actin to allow a consistent F-actin staining over time and throughout the different cell generations.

3.2.4 Time lapse image acquisition

The 2D images were acquired using a Zeiss AxioObserver 7 epifluorescence and a 10x, 0.45 numerical aperture (NA) objective (Zeiss, #420641-9910-000). One field of view was taken for each well/condition in the center of the well. Fluorescence channels mVenus, mCherry and SiR-Actin were recorded with 100 % LED intensity at 511, 555 and 630 nm illumination wavelength, respectively. The following filter sets used were: (i) Zeiss #46 HE (500/25 nm excitation and 535/30 nm emission) for mVenus, (ii) Zeiss #45 (560/40 nm excitation and 630/75 nm emission) for mCherry and (iii) Zeiss #50

(640/30 nm excitation and 690/50 nm emission) for SiR-Actin. All fluorescence channels were recorded at 300 ms exposure time. The phase contrast channel was recorded with transmitted light at 20 % light intensity and without any filter set. Time lapse images were acquired with intervals of 30 minutes for 90 h.

3.3 FUCCItrack software description and workflow

3.3.1 FUCCItrack software installation

FUCCItrack is built with MATLAB (R2019b, v 9.7) and is open-source, available as the (a) MATLAB App/Toolbox and (b) MATLAB source code or (c) a standalone application (MATLAB does not need to be installed to use the software). The application can be run on Windows, macOS or GNU/Linux operating systems.

(a) MATLAB App/Toolbox. This can be found at https://github.com/hubert-taieb/FUCCItrack. Users should download the "FUCCItrack.mlapinstall" file, open MATLAB, go to the APPS tab and click "Install App". Select the downloaded file and then install it. It is possible to open it from the APPS tab or via the command line.

(b) MATLAB source code. Users should download the package "FUCCItrack_2021.02_source_code.rar" at https://github.com/hubert-taieb/FUCCItrack and extract the files. Then open MATLAB and go to the folder containing the package. Directly run "FUCCItrack_V2021_02.mlapp" within the MATLAB command line.

(c) Standalone application. The executable can be found at https://github.com/hubert-taieb/FUCCItrack under "FUCCItrack_installer.exe". Directly open the file from the explorer and follow the instructions.

3.3.2 Software description and workflow

FUCCItrack is a GUI that is tailored for the FUCCI2 system, but also extensible to other two-color fluorophore combinations. The complete workflow is described in Figure 3-2 and refers to the five main independent modules to analyze collective as well as single FUCCI2 cells. There is one additional concatenation module, which is optional and described below. Some modules are fully automatic, and others are semi-automatic, with options for manual corrections. FUCCItrack also allows to save and reopen a

session with the application returning to the previously saved state. See the Appendix A for a complete user's guide of FUCCItrack.

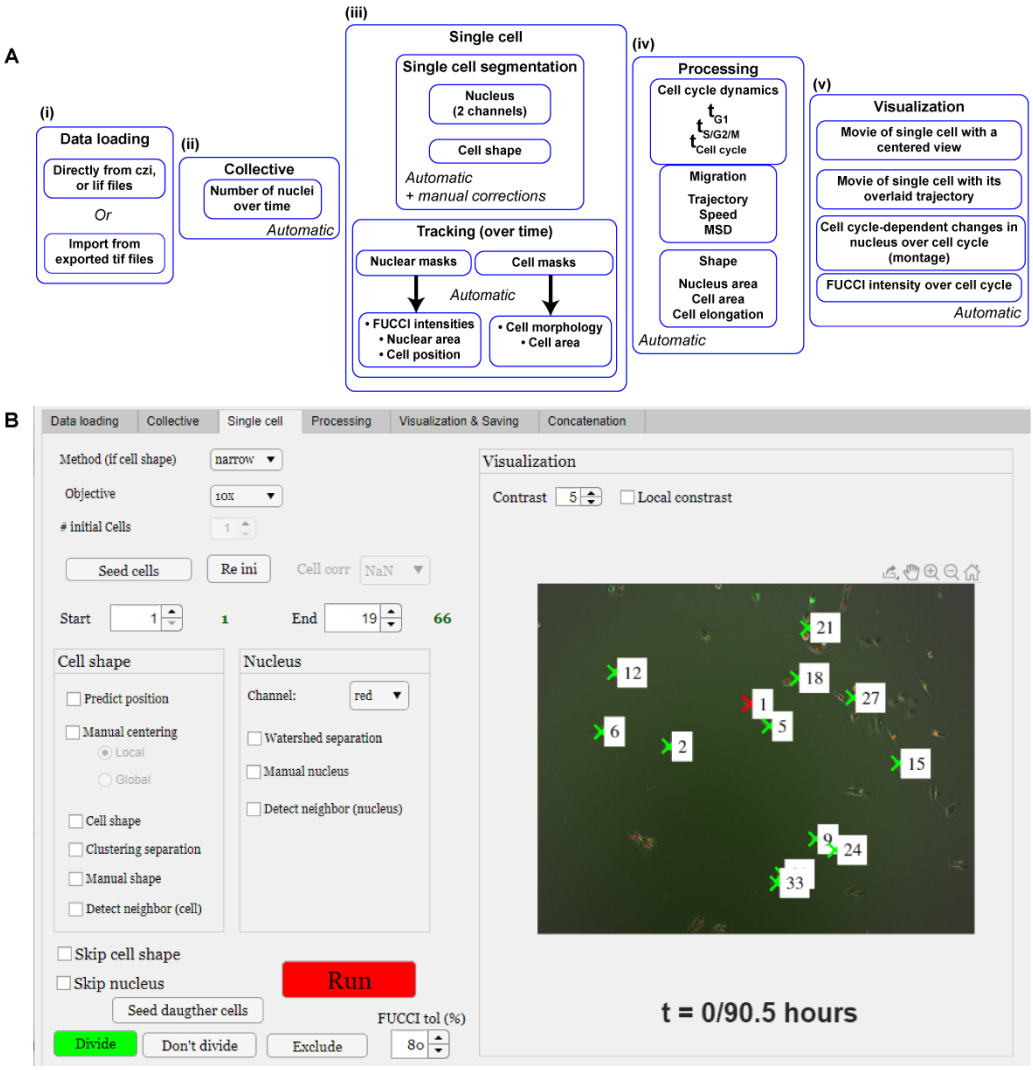

Figure 3-2 Workflow and user interface of FUCCItrack.

(**A**) Workflow describing the use of FUCCItrack, from loading to visualization. (**B**) Single cell panel describing the segmentation and tracking user interface.

Data loading module

Processing of the images begins by loading the native microscope data as described in Figure 3-2A(i) (Zeiss ."czi" or Leica ".lif" file). This allows to automatically extract the metadata, such as the spatial resolution and time interval, and the fluorescence/phase contrast channels used in the experiment. It also avoids having any data loss due to compression needed for precise quantification. If the native microscope data is not available, FUCCItrack can load multi-tiff stacks (the layers of the stacks representing different time intervals) or sequential-tiff images. For this, the user must specify

manually the pixel size (in µm/pixel), the time interval (in h) and ensures the microscopy images were exported without data compression. The preferred mode of import is to use the raw microscopy files (.czi or .lif) that use open-source OME bio-formats library [80] since it requires less user input and is more standardized.

For FUCCI2 datasets, the minimal requirement is to have at least two fluorescence channels for the nucleus (named mCherry and mVenus), and one for the cell itself (phase contrast image and/or SiR-Actin fluorescence for example). Epifluorescence 2D images were used for this chapter but maximum projection of 3D confocal image stacks or individual slices also yields similar results, as described in Chapter 5. Using these inputs, FUCCItrack then runs at two different levels: (i) collective and (ii) single cell level.

Collective module

The collective level allows users to extract the cell number as a function of time in a fully automated way (Figure 3-2A(ii)). Despite its simplicity, this counting method can already give valuable information on the cell proliferation under any experimental conditions, using 2D epifluorescence microscopy in real time.

FUCCItrack makes use of the fluorescence channels visualizing the nucleus and automatically counts the number of cells as a function of time, using an adaptive thresholding approach based on a mean local intensity [81]. This adaptive thresholding is necessary for two reasons. In the FUCCI2 system, the fluorophores are attached to proteins that are getting degraded or produced over time. This means that two cells on the same field of view can have different intensity levels at the same time even though they are both in the same cell cycle phase. Moreover, the absolute mCherry and mVenus maximum intensities that a cell reaches during its cell cycle is not the same throughout a population of cells. For these reasons, it is not possible to use a global thresholding approach with one cut-off value for the intensity. Instead, an automatically defined local threshold is computed and yields the best segmentation results.

In addition, since the two fluorophores are cell cycle reporters, the collective level permits to gain insight on the fraction of $mCherry^+$ and $mVenus^+$ cells at a given time point based on the two fluorescence channels segmented. An extra-step to verify whether the same cell is present in both channels is then applied and cells are categorized as $mCherry^+/mVenus^-$ (G1 phase) or $mVenus^+$ (S/G2/M phase). This module gives an overview of the cell proliferation behavior as well as fractions of cells

in distinct G1 or S/G2/M cell cycle phases (Figure 3-3) but does not provide any tracking of single cells over time.

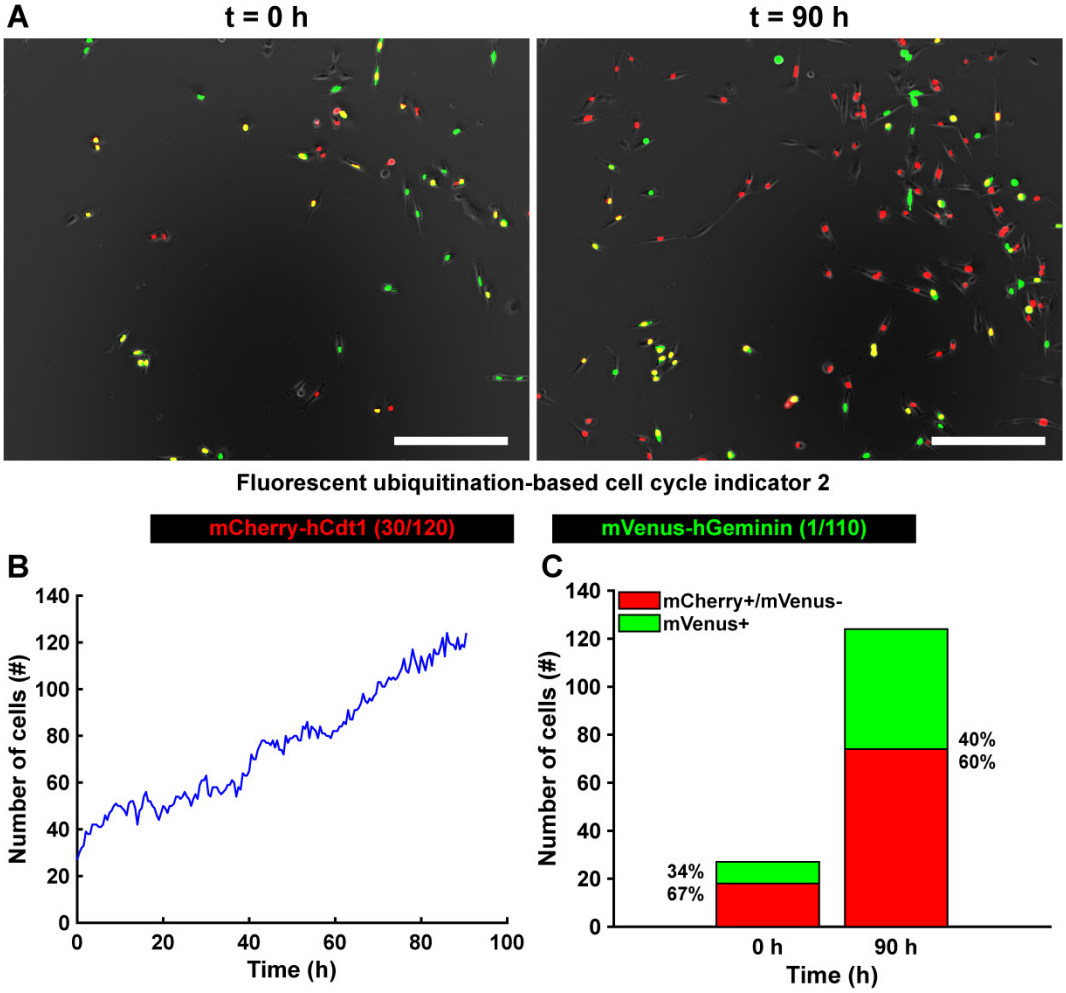

Figure 3-3 Cell proliferation of MDA-FUCCI2 human breast cancer cells at collective level.

(**A**) Time lapse of MDA-FUCCI2 over 90 h of imaging. Scale bars are 200 µm. (**B**) Number of cells as a function of time obtained from the automatic collective segmentation. (**C**) Fraction of mCherry^{+}/mVenus^{-} (G1 phase) and mVenus^{+} (S/G2/M phase) cells at the beginning and at the end of the 90 h of imaging.

Single cell module

Automatic collective segmentation cannot track mitosis events efficiently. However, the single cell module seen in Figure 3-2A(iii) allows tracking single cells and segmenting shapes of nuclei, as well as cell shape automatically. It opens a new realm of information to study single cell cycle dynamics, migration (trajectory and velocity), and changes in nuclear and cell morphology throughout several generations of cells.

The tracking module is presented in Figure 3-2B. The user is invited to select a cell of interest manually (“Seed cells” button) to specify which cell from the field of view should be tracked. Starting from the current frame and after pressing “Run”, the automatic segmentation and tracking of this cell over time starts (Figure 3-2A(iii), Figure 3-2B). After seeding the cell of interest, information about the segmented nucleus in both fluorescence channels is recorded, including coordinates of center of mass, area and FUCCI intensities. To track the cells in the next frame, the software uses a localized search region around the previous position. The size of this search region can be changed by the user, depending on the specifics of the cell line and interval used for imaging. A local adaptative threshold method is used to segment both mCherry and mVenus fluorescence channels in this search region. It then compares the several segmented nuclei found (coming from the cell of interest or others nearby) with the one in the previous frame in term of distance, fluorescence intensity, and shape. The algorithm then picks the candidate that is the most similar to the previous time point. If the algorithm fails to find the corresponding nucleus from one frame to the other, it is possible to use the “Manual centering” option to manually correct the cell tracking, while the rest of the segmentation proceeds automatically.

As presented in Figure 3-2B and described more in detail in the Appendix A, the user can run segmentation tasks on the datasets using two different panels. One for cell shape (if a live cell actin or cell membrane staining is used such as SiR-Actin), and one for the nucleus. If users have a live cell actin or cell membrane staining or analog, they can select the “Cell shape” to perform cell shape segmentation. When using the option to detect already segmented neighbor cells, the tracking accuracy improves with the number of already segmented cells. After the division of the original manually seeded cell, the user is invited to register cell division by using the “Divide” button, followed by the “Seed daughter cells”. This automatically seeds the two daughter cells for further tracking and creates the lineage between cell generations.

Users can choose to perform automatic cell shape segmentation if a specific fluorescent dye is present in their experiment or manual segmentation using the phase contrast/bright field images. This remains optional, and users can also use FUCCItrack to only perform tracking and segmentation of nuclei.

Processing module

The processing module allows users to extract the information from cell tracking and segmentation to receive information on cell cycle dynamics, migration parameters and shape analysis.

Once the segmentation is performed, either automatically or with manual corrections, the intensity values inside the nuclear mask of each channel are extracted. The mean intensity inside the nucleus is computed to determine the duration of the cell cycle phases in the “Processing” tab (Figure 3-2A(iv)). The intensity curves are normalized by the maximum intensity reached during its cell cycle, in each mCherry and mVenus channels independently, due to the variability between cells and fluorescence channels. From these curves the durations of the cell cycle phases can be obtained (Figure 3-4A, Figure 3-4B). The beginning of the S/G2/M phase is then defined as the time when the intensity of mVenus exceeds 5 % (this value can be modified by the user depending on their cell lines) of the maximum intensity. The same method applies for the beginning of the G1 phase (Figure 3-4B). The software computes the cell cycle dynamics parameters (t_{G1}, $t_{S/G2/M}$, $t_{Cell\ cycle}$) for each single cell tracked and the result can be exported as text file.

The information about the position over time of every cell tracked is also available from the segmentation data for further cell migration-related analysis (Figure 3-5). Indeed, after segmentation, the position of each nucleus is determined by computing the center of mass of the resulting mask. Basic trajectory analysis can be computed automatically by pressing the “Add tracks” button, including cell migration speed, displacement, total distance traveled, directionality and mean square displacement (using the package msdanalyzer [82]). When FUCCI2 datasets are used, it is possible to extract these migration parameters as a function of the cell cycle status. All results can be exported in a text file.

Finally, because of the segmentation data, cell and nuclear morphological information can be used in correlation with the cell cycle phases. The processing module performs morphological analyses of those data and calculates nuclear and cell area, equivalent diameter and elongation over time (Figure 3-6). For this application, only daughter cells are used, and the area is normalized by the area at 2 h after division (this can be adjusted by users). Frames corresponding to 2 h before the next division are excluded from the analysis, since they usually represent cells rounding up before division.

Visualization and saving module

In addition to the processing module, FUCCItrack also contains a dedicated module for automatic data visualization (Figure 3-2A(v)). All figures presented in this chapter have been created automatically with the software (Figure 3-3 to Figure 3-6) and exported as vector and pixel-based files for maximum quality.

More functions allow users to create movies automatically, showing only the region where the cell migrated over time, with its trace overlaid on the microscope images, or a movie centered on the cell over time.

Concatenation module

The description above relates to one time lapse cell imaging experiment contained in one file. However, a concatenation module is also available. This module allows users to first run the application with a file from one experiment and then append another file that corresponds to the follow-up of the last time point of the previous experiment. This allows users to change environmental conditions (by even removing the plate from the microscope to change conditions) and still be able to match the cells in both experiments by correlating their position, thereby capturing changes in cell behavior under a dynamic environment. This module was extensively used for the reactivation experiments as described in the Chapter 4.

3.4 Results

3.4.1 Collective level

Here we demonstrate the functionality of FUCCItrack by tracking, segmenting and analyzing MDA-FUCCI2 breast cancer cells but the software could be used with other cell lines such as MCF7-FUCCI2. With the automatic collective module, the cell proliferation or the number of cells as a function of time is evaluated (Figure 3-3A, Figure 3-3B). Thirty initial cells in the field of view proliferate to 120 cells at the end of the experiment, after 90 h. Because the counting method can be applied to the mCherry and mVenus channel independently, the user can evaluate the number of cells that express only mCherry ($mCherry^+/mVenus^-$, defined as G1 cells) or mVenus ($mVenus^+$, defined as S/G2/M cells) as demonstrated in Figure 3-3C. Initially and after 90 h, the ratio of cells in G1 and S/G2/M phases remains roughly constant at 60 % and 40 % respectively, indicating a normal proliferation. The results are obtained

completely automatically, which makes this software a powerful tool to quantify cell proliferation easily and efficiently in real time.

3.4.2 Cell cycle dynamics

In total, 11 cells were randomly selected for single cell tracking at the beginning of the experiment (Figure 3-2B). The user can choose to exclude cells due to fluorescence intensity problems (fluorescence intensity missing for mCherry or mVenus) or cells leaving the field of view during the tracking. The 11 selected cells and their descendants were tracked during the 90 h of live imaging. An illustrative example with cell #8 is given in Figure 3-4B and Figure 3-4C. Users can display the average fluorescence intensity inside the segmented nucleus for both mCherry (red line) and mVenus (green line), with the shaded red and green areas corresponding to the standard deviation inside the nucleus. From the total of 35 cells that were tracked, the median of the G1 phase was 14 hours, the median of the S/G2/M phase was 25 hours, and the total cell cycle duration median was 36 hours (Figure 3-4D).

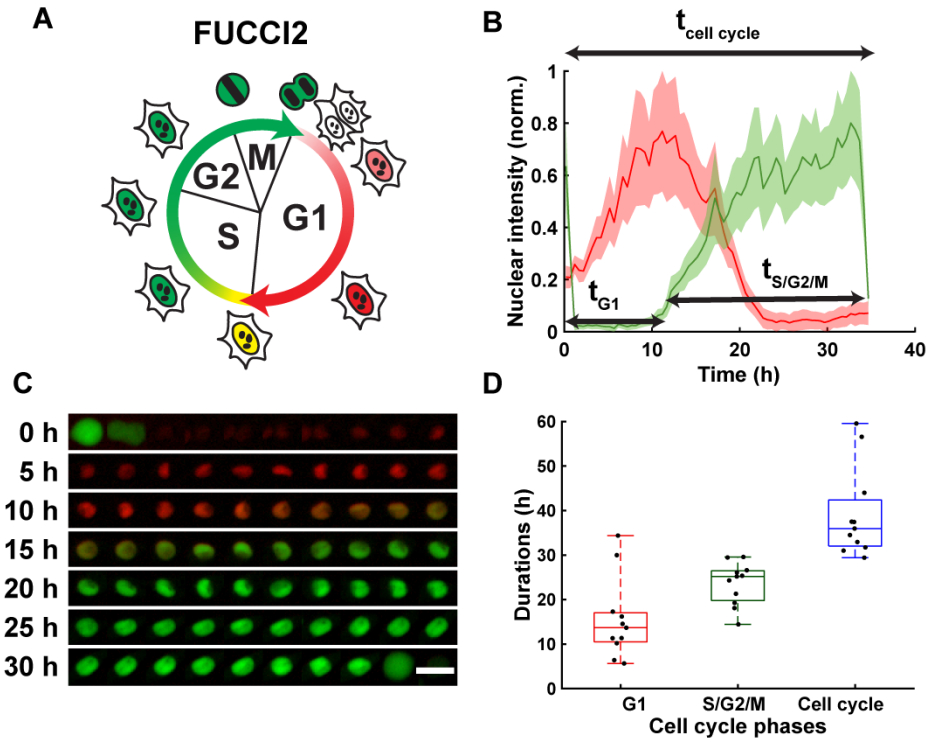

Figure 3-4 Single cell tracking with the FUCCI2 system.

(**A**) FUCCI2 cartoon representing the mCherry (red) and mVenus (green) fluorescence of the nucleus during the cell cycle. (**B**) Normalized fluorescence intensity in mCherry (red) and mVenus (green) for cell #8, with the corresponding

duration of the phases. (**C**) Corresponding fluorescence images of the segmented nucleus over time. Scale bar is 25 µm. (**D**) Duration in hours of the cell cycle phases: G1 (red), S/G2/M (green) and total cell cycle (blue) for N = 11 cells. The FUCCI2 cartoon was adapted from Sakaue-Sawano et al. [49], Copyright (2008), with permission from Elsevier.

3.4.3 Migration and shape analysis

From MDA-FUCCI2 tracked cells, cell migration related parameters can be computed throughout their cell cycle. First, the trajectories of cells are displayed in Figure 3-5A exhibiting a random cell migration. The mean square displacement (MSD) is evaluated for every cell and shown in Figure 3-5B, with a median migration speed of 0.20 µm/min (Figure 3-5C). The median displacement (distance between the beginning and the end of the trajectory) is 69 µm (Figure 3-5D) whereas the median of the total accumulated distance traveled during their trajectory is 500 µm (Figure 3-5E). Finally, the directionality, measured as the ratio of the displacement and the total distance, is 0.18 (Figure 3-5F), far less than 1 corresponding to a perfectly directed motion.

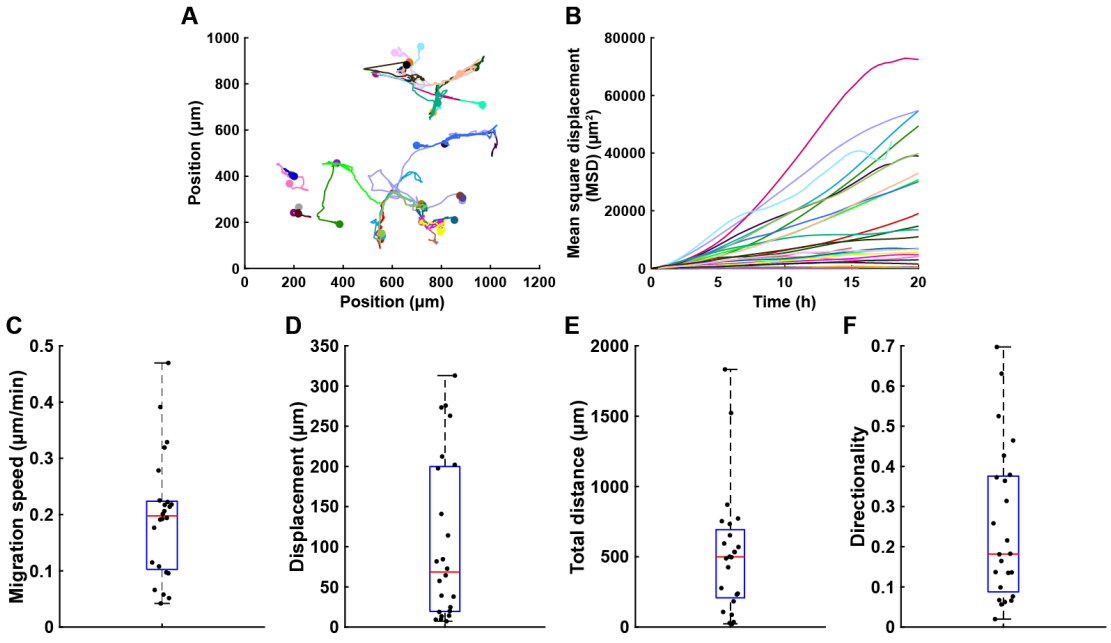

Figure 3-5 Cell migration analysis with the FUCCI2 system.

(**A**) Trajectories of MDA-FUCCI2 cells during their cell cycle. (**B**) Corresponding mean square displacement (MSD) for every cell tracked. (**C-F**) Boxplots showing the heterogeneity between MDA-FUCCI2 cells (n = 24) according to four migration

features of (**C**) migration speed, (**D**) displacement (distance from beginning to end of trajectory), (**E**) total distance (total trajectory length) and (**F**) directionality (ratio of the displacement to total distance).

Based on the nuclear segmentation, the nuclear shape evolution over time can be investigated, such as projected area throughout the cell cycle progression. The nuclear projected area is normalized to the first frame 2 h after division for each cell so that only the increase in area during the cell cycle is taken into account as presented in Figure 3-6B, due to variability between cells.

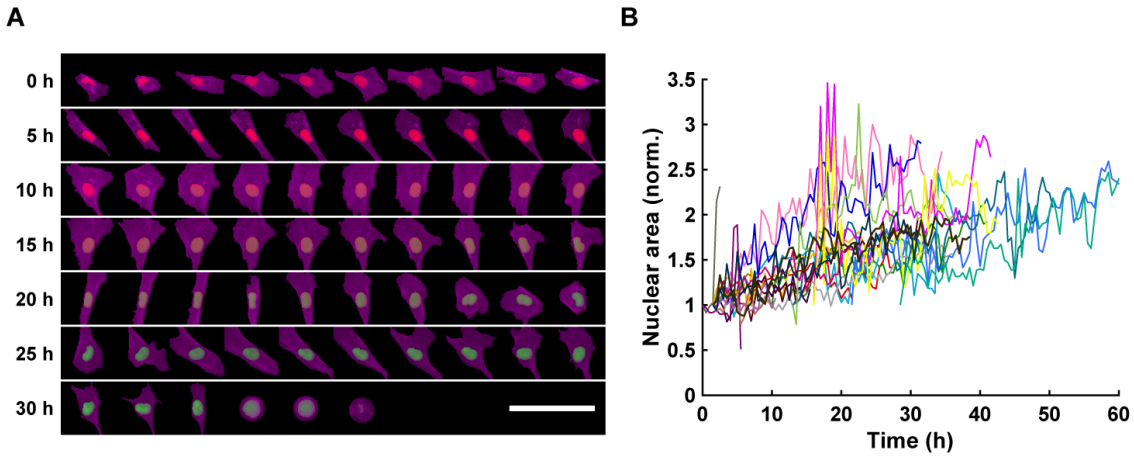

Figure 3-6 Cell and nuclear shape analysis.
(**A**) Overlay of nuclei (red/green) and cell F-actin (magenta) as a function of time for cell #1. Scale bar is 100 µm. (**B**) Normalized nuclear area as a function of time for dividing cells (n = 24).

3.5 Discussion

Here we report FUCCItrack: an application that can be installed within MATLAB or as a standalone application and offering an all-in-one platform to perform segmentation of cell and nucleus, tracking, processing and visualization of cell cycle dynamics, along with migration and shape analyses. It provides non-programmers with a reliable and quantitative solution with a minimum effort as most processes are automatized. The gathering of all these tools into a common robust application diminishes the workload in comparison to more common manual tracking methods. We added the capability to generate graphics and movies from within the software directly. In addition, all results can be exported as text files to be further processed or analyzed by other tools.

FUCCItrack is modular in its construction, which will facilitate future upgrades to include more features such as 3D cell tracking and segmentation.
We released FUCCItrack as a standalone application to avoid any dependency on MATLAB licensing to reach as many people as possible, and with its original source code to remain transparent. The source code is properly commented to offer guidance to fellow programmers who would like to modify it.
We tested FUCCItrack on other computers and other exploitation system with one of our datasets to make sure of its compatibility in an alpha test, but we are aware that upon release, unexpected complications may arise. That is why we linked the release to a public repository such as GitHub, so that FUCCItrack can be maintained over the years.
The software was first developed and improved extensively throughout the years to perform quantitative time lapse imaging and to answer relevant biological questions presented in Chapter 4 and Chapter 5 related to the effect of osmotic pressure and fluid flow on breast cancer cell cycle.

3.6 Limitations

The FUCCItrack software has been specifically developed to work with FUCCI2, as this was the system that was available to us for our experiment design. This means that in its current state there is a rigid requirement to use three channels (one for mCherry, one for mVenus and another for the phase contrast or any live cell dye). To bypass this limitation, researchers who only image with fluorescence channels can just copy the images from one of the channels into the “Phase” contrast folder before loading the images (see Appendix A FUCCItrack user’ guide for more information). This way, FUCCItrack can still be used, even though no cell segmentation could be performed.
Other than this, we adapted the software so that any new users with FUCCI or FUCCI2 time lapse images could use it right away. Other researchers with different cell cycle reporters may need to adapt the source code.

Chapter 4 Osmotic pressure and human metastatic cells

♫ "Pressure: pushing down on me,
Pressing down on you, no man asks for."

Under pressure, Queen & David Bowie

Biophysical cues such as osmotic pressure modulate proliferation and growth arrest of bacteria, yeast cells, and seeds. In tissues, osmotic regulation takes place through blood and lymphatic capillaries and, at a single cell level, water and osmoregulation play a critical role. However, the effect of osmotic pressure on single cell cycle dynamics remains poorly understood. In this chapter, we investigate the effect of osmotic pressure on single cell cycle dynamics, nuclear growth, proliferation, migration and protein expression, by quantitative time lapse imaging of single metastatic cells genetically modified with FUCCI2.

4.1 Introduction

Osmotic pressure is a biophysical cue that modulates cell function. Osmotic pressure changes have been widely associated with growth arrest and proliferation in plants and seeds [35, 36], and more recently in bacteria [33] and yeast [34]. In human physiology, osmotic regulation is present in multiple phenomena. Tissue architecture results from an equilibrium between forces that expand tissue volume, such as osmotic or hydrostatic fluid pressure, and forces that will counterbalance this expansion, such as tension in the extracellular matrix or contractile forces by cells [83]. Osmotic gradients also arise through the lymphatic system and in blood capillaries in the bone marrow. Specifically, a net positive balance of hydrostatic and osmotic pressure drives fluids out of arterioles, while a negative balance drives fluid back into the venules [84-86]. At a cellular level, osmoregulation is a crucial phenomenon that allows cells to respond to changes in ion concentration in their microenvironment through transmembrane proteins responsible for water/ion transport [87, 88]. In a seminal work by Weitz and colleagues, it was shown that variations in external osmotic pressure can induce

changes in cell volume, intracellular molecular crowding as a result of water efflux, changes in cell stiffness and ultimately impact mesenchymal stem cell differentiation in the osteogenic or adipogenic lineage [89].

Yet, the effect of osmotic pressure on single cell cycle dynamics, in particular growth arrest and reactivation, remains poorly understood. Its effect on bulk cell proliferation has been reported, with hyperosmotic pressure resulting in reduced overall proliferation of various human metastatic cells [12, 90]. However, less is known about how the osmotic pressure affects single cell cycle dynamics. Quantitative and real-time tracking of the cell cycle dynamics is possible with the FUCCI system and is increasingly used to detect non-dividing cells in the context of cancer therapies [48].

Here, we hypothesize that osmotic pressure can play a role in human cell niches likely to harbor non-cycling quiescent cells by modulating the reversible growth arrest and reactivation into a proliferative state. To test this hypothesis, we use a highly proliferative human metastatic cell line, which we genetically engineered with FUCCI2 to perform quantitative time lapse imaging of the different phases of the cell cycle at a single cell level.

4.2 Materials and methods

4.2.1 Cell culture

Cell culture was performed exactly as described above in section 3.2.2. The cell line MDA-FUCCI2 was used as a model for highly metastatic breast cancer cells and is a mutant p53 cell line, whereas the MCF7-FUCCI2 cell line was used as a model for weakly metastatic breast cancer cells and is a wild-type p53 [79].

4.2.2 Osmotic pressure

Conventional methods such as vapor-pressure depression or freezing-point method are hardly applicable to measure osmotic pressure values *in vivo* [91, 92]. Recently, a novel biomaterial-based osmotic pressure sensor was developed to possibly fill the gap and enable measurements of osmotic pressure [93]. Osmotic pressure values used in this study were based on those used in previous works [30, 89, 94, 95], and were below acute hyperosmotic stress values that lead to cell death [96].

Increase of osmotic pressure was controlled by adding sterile 300 Da polyethylene glycol (PEG 300) (VWR, #8.17002.5000) or D-Sorbitol (Sigma, #240850) into the cell

culture media. We used PEG 300 because it is the most used osmolyte and is not absorbed by the cells. Also, the low molecular weight PEG was used to do not alter the viscosity of PEG and limits the number of confounding variables.

In addition, we used D-Sorbitol which is commonly used [94, 97-101] as a different osmolyte to verify if our results were PEG specific.

Osmolality as a function of PEG 300 concentration was measured with a freezing point osmometer (Gonotec, Osmomat 3000, Figure 4-1) to reach the targeted hyperosmotic stress: 380 mOsm/kg (PEG^{+}, 1.5 % wt/vol PEG 300) and 460 mOsm/kg (PEG^{++}, 3 % wt/vol PEG 300). The same osmolality values were reached with D-Sorbitol using 60 mmol/L ($Sorbitol^{+}$) or 140 mmol/L ($Sorbitol^{++}$).

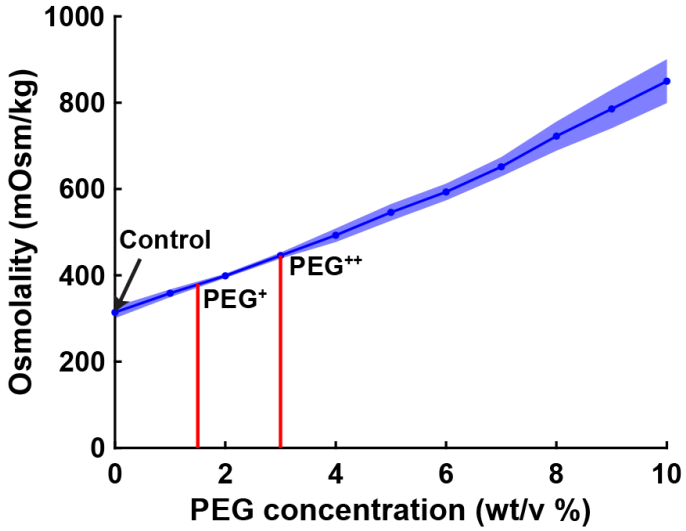

Figure 4-1 Osmolality as a function of PEG 300 concentration in cell culture media.

Normal cell culture media has an osmolality of 320 mOsm/kg (control). Two hyperosmotic pressures were used in this thesis: 380 mOsm/kg (1.5 wt/vol %, PEG^{+}) and 460 mOsm/kg (3 wt/vol %, PEG^{++}). The curve represents the mean (n = 3) and the shaded area is the standard deviation.

4.2.3 Time lapse experiments protocol

To understand the role of osmotic pressure in cell proliferation, MDA-FUCCI2 cells were cultured and observed in the presence of PEG 300.

From regular passaging petri dishes, MDA-FUCCI2 cells were washed with phosphate buffered saline (PBS), detached with trypsin (PAN-Biotech, #38220000) and centrifuged at 300 g for 5 minutes. Cells were then resuspended with cell culture media

only (control), or with additional 1.5 % wt/vol PEG 300 (380 mOsm/kg, PEG^{+}) or with 3 % wt/vol PEG 300 (460 mOsm/kg, PEG^{++}). They were then seeded at 7500 cells/mL (200 µL) on a 96 well glass bottom microplate (Greiner Bio-one, #655892) and allowed to equilibrate and adhere for 24 hours at 37 °C with 5 % CO_2 before imaging. The cell seeding density was chosen so that the wells remained subconfluent until the end of the imaging period, to reduce possible errors during single cell tracking. After 24 h, cells were placed in a stage top incubator with similar culture conditions (Okolab, UNO-T-H-CO2) mounted on an inverted epifluorescence microscope (Zeiss, AxioObserver 7) for long-term time lapse imaging. Similar procedure was used with MCF7-FUCCI2 cells.

4.2.4 Time lapse Image acquisition

All images were acquired with a Zeiss AxioObserver 7 and a 10x, 0.3 NA objective (Zeiss, #420341-9911-000) or a 10x, 0.45 NA (Zeiss, #420641-9910-000). One field of view was taken for each well/condition in the center of the well. Both fluorescence channels mVenus and mCherry were recorded with 100 % LED intensity at 511 nm and 555 nm illumination wavelength, respectively. The filter set Zeiss, #46 HE (500/25 excitation and 535/30 emission) was used to image mVenus and the filter set Zeiss, #45 (560/40 excitation and 630/75 emission) to image mCherry, both were recorded at 300 ms exposure. In addition, phase contrast image was also recorded. Images were acquired every 30 minutes for 90 h.

4.2.5 Proliferation assay

Using the time lapse imaging of MDA-FUCCI2, cell number as a function of time was obtained with the FUCCItrack software. For each frame, both fluorescence channels mCherry and mVenus were independently segmented using an adaptative threshold approach. Then each cluster of pixels, representing each nucleus, was measured in terms of number of pixels. All clusters smaller than 4 µm in radius were discarded. This process was done automatically for all frames to obtain the curves indicating the number of cells as a function of time (Figure 4-2). Using these curves, the proliferation rate was computed as the slope of a linear fit ($y = ax + b$, from 0 to 30 h or unless stated otherwise).

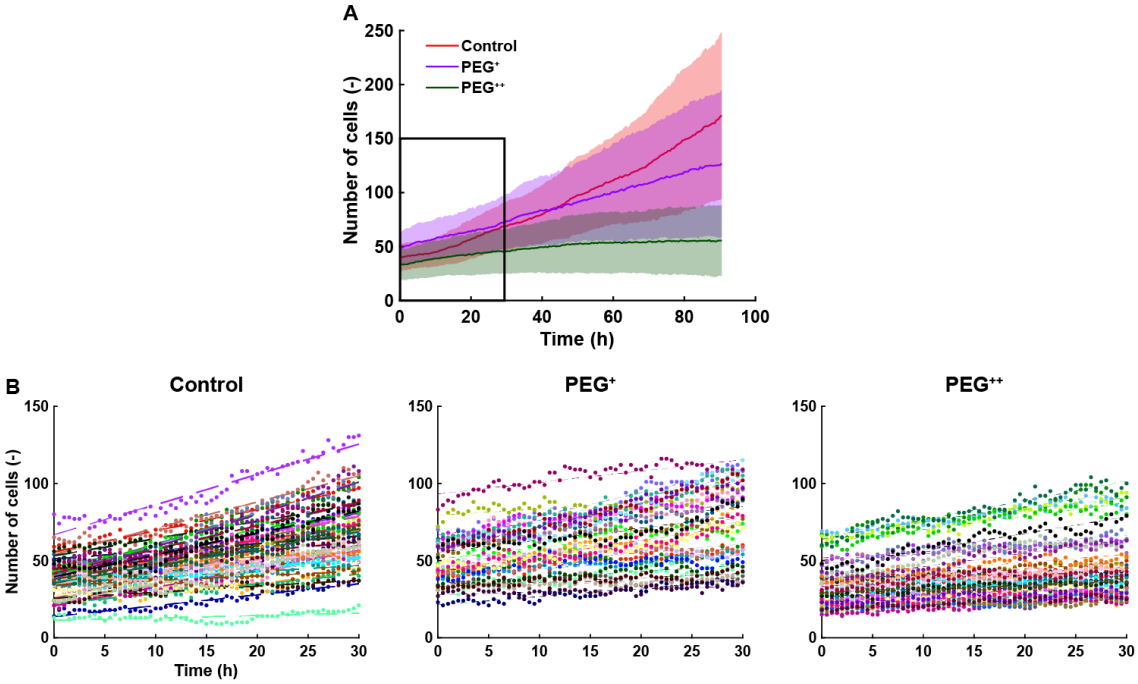

Figure 4-2 Proliferation assay: number of cells as function of time.

(**A**) Average and standard deviation of the cell number as a function of time among all repeats (N = 43, 30 and 43 wells for the control, PEG^{+} and PEG^{++} groups respectively). (**B**) Details of each curve per well as indicated by the box in panel A. Theses curves are used to compute a linear fit (y = ax + b) from 0 to 30 h, and the slopes correspond to the data in Figure 4-3, defined as proliferation rate.

4.2.6 Single cell tracking and cell cycle dynamics

Automatic single cell tracking and cell cycle dynamics quantification was done using the FUCCItrack software. Mitosis events were tracked from the beginning of the experiment and up to 30 h. Single cell cycle dynamics were then recorded for the first generation of daughter cells, where time 0 h for each single cell was defined by the first frame after division of the parent cell. This way, the total duration of the cell cycle could be measured from beginning to mitosis. This was necessary as the readout t_{G1} and $t_{Cell\ cycle}$ are defined with respect to the beginning of the cell cycle. Briefly, the nuclei were automatically segmented, and the nuclear fluorescence intensity as well as nuclear area was being recorded over time. To account for cell variability, the intensity for each channel was independently normalized with respect to its maximum value during the whole cell cycle, for each channel mCherry and mVenus separately. Using the normalized nuclear intensity as a function of time, the duration of cell cycle, G1 and S/G2/M phases were quantified as shown in Figure 4-6A (right middle panel). For the

cell subpopulation “G1 incomplete” scenario (the S/G2/M phase never started), the t_{G1} was taken as the duration between the start of cell cycle and the end of the experiment (90 h) and was then only a lower limit for the actual duration and not an exact value like for all other cell subpopulations.

4.2.7 Immunofluorescence

After 90 h of imaging, cells were washed with PBS and fixed by adding 200 µL per well of a 4 % paraformaldehyde (Boster, #AR1068) solution for 30 minutes at room temperature. After washing twice with a 3 % wt/v bovine serum albumin in PBS, cells were permeabilized with 0.1 % wt/v Triton-X-100 (Sigma-Aldrich, #T8787) in PBS for 10 minutes at room temperature. After two washing cycles, cells were incubated for 17 h in the fridge, either with a 305 ng/mL p21 Waf1/Cip1 primary antibody (Cell Signaling Technology Europe, #2947S) in a dilution buffer containing PBS + 3 % wt/v BSA + 0.1 % Triton-X-100, or with a 1.25 µg/mL Ki67 primary antibody (Abcam, #ab15580) in the same dilution buffer. For each experimental group, two wells were used as negative controls to verify the specificity of the secondary antibody. For this, we did not add the primary antibody in the negative controls, but only the buffer solution. After washing twice, all cells were incubated for 1 h at room temperature in 10 µg/mL Alexa Fluor 647 goat anti-rabbit antibody (Life Technologies, #A21244) in the same dilution buffer. After two washing steps, cells were imaged using the same microscope and settings as described above. A custom-made MATLAB application was developed named ImmunoFinder (Appendix B) to count the number of p21/Ki67 positive cells. Briefly, the two channels from the FUCCI2 reporter were artificially merged and used to localize the cells. The negative controls of p21 and Ki67 were then used to determine the background signal of the secondary antibody and thereby define the threshold for positive p21 or Ki67 signal. The application contains a graphical user interface to be usable by everyone without prior programming skills required as visible in Appendix B.

4.2.8 Reactivation experiments

Because dormancy is a reversible mechanism, we wanted to observe how the highly metastatic breast cancer cells react when removing the osmotic stress. For this we designed reactivation experiments that followed the initial time lapse osmotic stress experiments.

After the 90 h initial experiment under the three different conditions (control, PEG^{+} and PEG^{++}), the media was renewed in all groups with standard cell culture media. Then time lapse imaging was performed during additional 90 h, at the exact same location. Similar analyses were performed to extract the MSD, migration speed, and single cell cycle dynamics. To do so, mitosis events were tracked from the beginning of the reactivation and up to 30 h. Single cell cycle dynamics were then recorded for the first generation of daughter cells. This way, the cell cycle total duration for each cell could be measured. This defines the time = 0 h in Figure 4-10 and Figure 4-11.

4.2.9 Statistical analysis

All the data presented in this chapter comes from up to five biological repeats for the three experimental groups each. We define a biological repeat as an experiment that was done with a different batch of thawed cell. All data were analyzed using MATLAB. The plots represent the median, 1st and 3rd quartiles and extrema. Statistical analysis was done with respect to the control using a non-parametric two-tailed Wilcoxon rank sum test except when stated otherwise, n.s: $p > 0.05$, *: $p < 0.05$, **: $p < 0.01$ and ***: $p < 0.001$.

4.3 Results

4.3.1 Hyperosmotic stress slows down cell proliferation

Osmolality values ranged from control values (320 mOsm/kg, with only cell culture media) to mild hyperosmotic stress (380 mOsm/kg, PEG^{+}) and high hyperosmotic stress (460 mOsm/kg, PEG^{++}) and the cells were monitored every 30 minutes for a period of 90 h (Figure 4-3A).

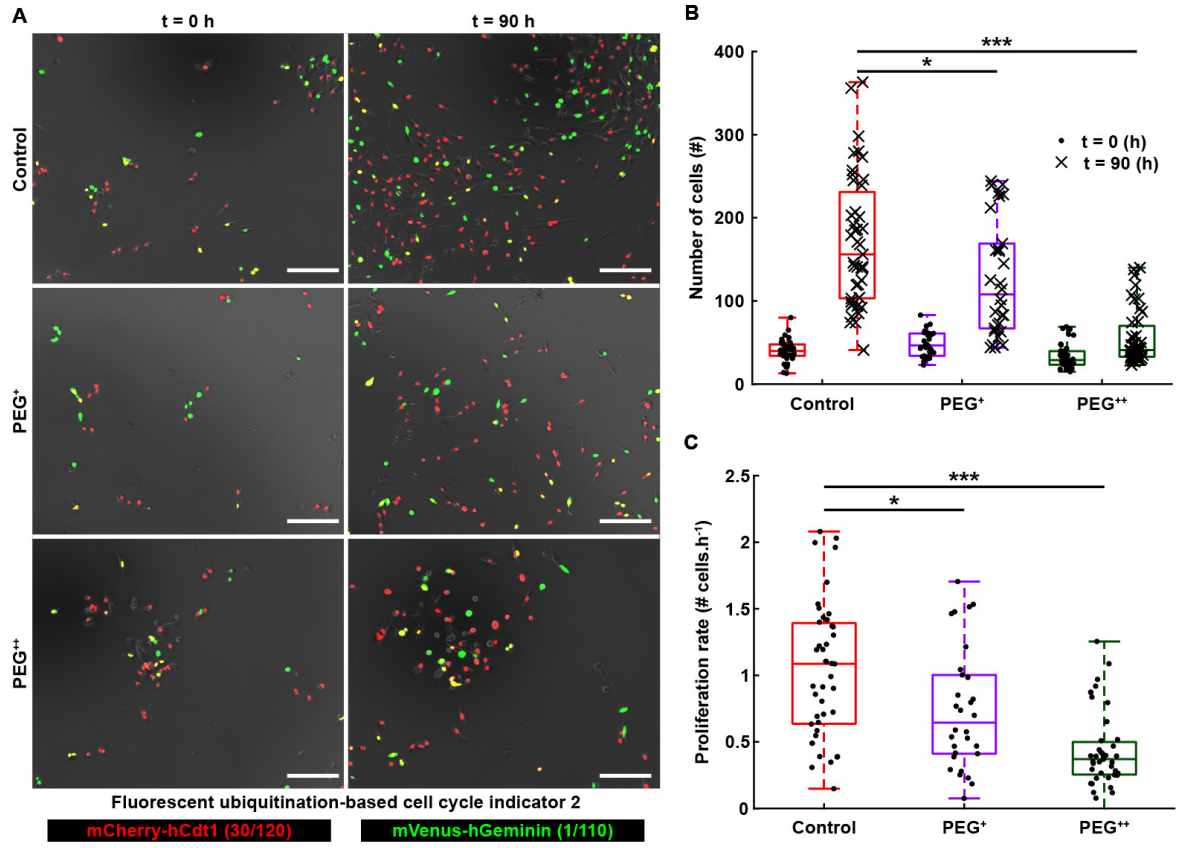

Figure 4-3 Increase of osmotic pressure slows down proliferation of MDA-FUCCI2.

(**A**) Time lapse of MDA-FUCCI2 cells exposed to three different osmolalities: 320 mOsm/kg (control), 380 mOsm/kg (PEG^{+}) and 460 mOsm/kg (PEG^{++}). Scale bars are 200 µm. (**B**) Number of cells at time 0 and after 90 h of imaging (5 biological repeats and N = 43, 30 and 43 number of wells for the control, PEG^{+} and PEG^{++} groups, respectively). (**C**) Proliferation rates are taken as the slopes of the curves indicating the number of cells as a function of time (Figure 4-2), in the range between 0 and 30 h.

Using the FUCCI2 reporter, the number of cells as a function of time was monitored in real-time. After 90 hours, both mild and high conditions significantly impaired proliferation (Figure 4-3B) when compared to the control, with a decrease of around four-folds for the highest hyperosmotic stress (PEG^{++}). In addition, the kinetics of cell proliferation was assessed by calculating the proliferation rate as the slope of the curve: number of cells as a function of time (Figure 4-2), in the linear range, between 0 to 30 h. The interval of 30 h was determined based on the duration of a total cycle in control condition (Figure 4-7B). Notably, already from an early time-point, cell cycle

dynamics were highly reduced (Figure 4-3C). These findings were reproduced with the weakly metastatic human breast cancer cell line MCF7-FUCCI2 (Figure 4-4). Namely, that hyperosmotic stress significantly reduced both proliferation (Figure 4-4B) and cell cycle dynamics (Figure 4-4C).

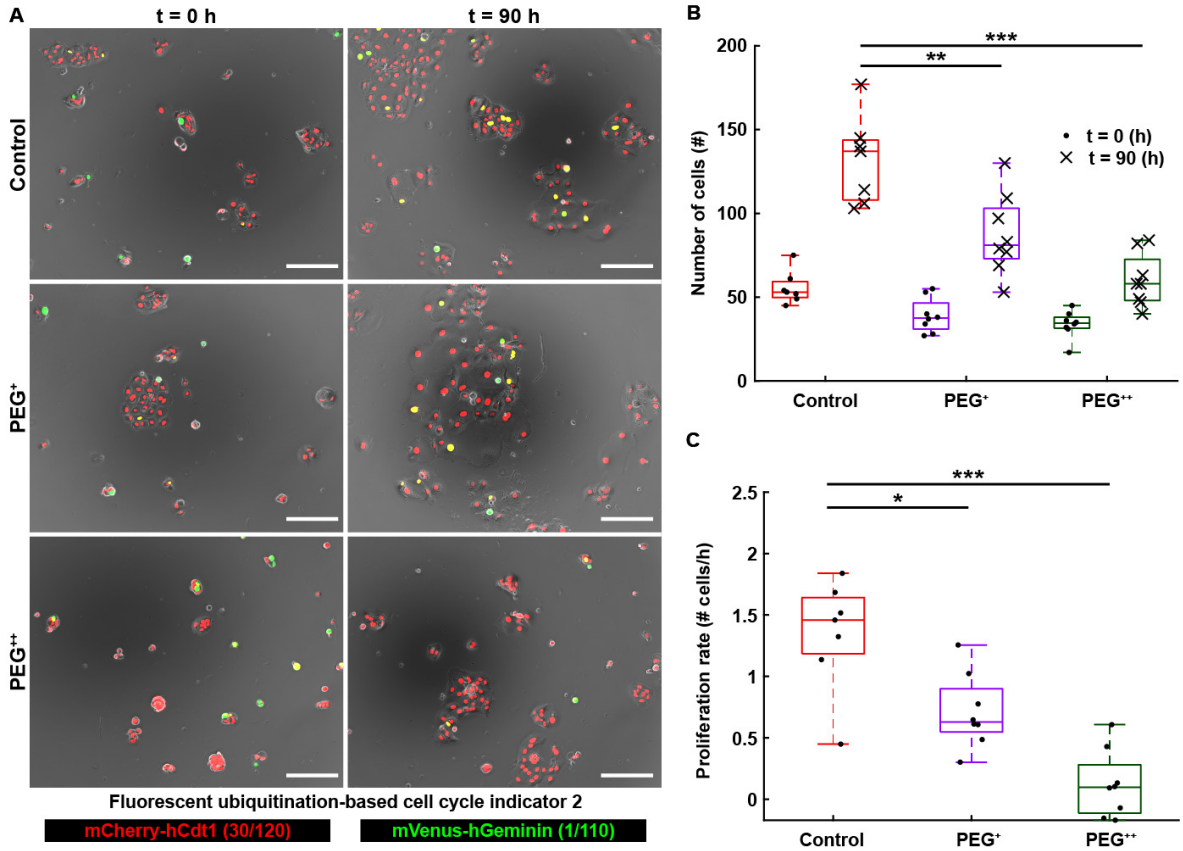

Figure 4-4 Increase of osmotic pressure slows down proliferation of MCF7-FUCCI2.

(**A**) Time lapse of MCF7-FUCCI2 cells exposed to three different osmolalities: 320 mOsm/kg (control), 380 mOsm/kg (PEG^{+}) and 460 mOsm/kg (PEG^{++}). Scale bars are 200 µm. (**B**) Number of cells at time 0 and after 90 h of imaging (one biological repeat and N = 7, 8 and 8 number of wells for the control, PEG^{+} and PEG^{++} groups, respectively). (**C**) Proliferation rates are taken from the slope of the curves indicating the number of cells as a function of time, in the range between 0 and 30 h.

The same osmolality values were applied with D-sorbitol over a period of 90 h: control values (320 mOsm/kg, with only cell culture media), mild hyperosmotic stress (380 mOsm/kg, $Sorbitol^{+}$), and high hyperosmotic stress (460 mOsm/kg, $Sorbitol^{++}$) (Figure 4-5). Analogous to the results obtained with PEG, cell proliferation was

significantly impaired when compared to the control (Figure 4-5B). In addition, the initial rate of cell proliferation was highly reduced at early time points (Figure 4-5C).

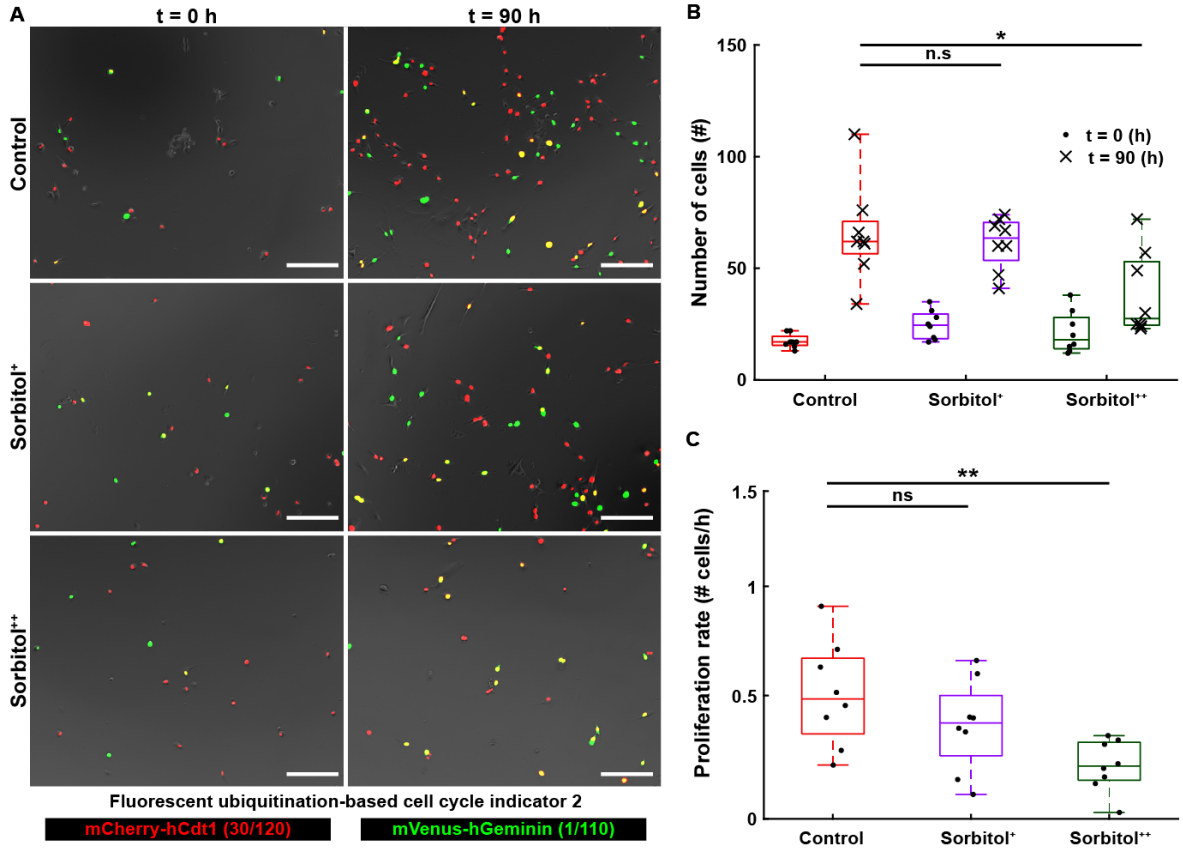

Figure 4-5 Increase of osmotic pressure via sorbitol slows down proliferation of MDA-FUCCI2.

(**A**) Time lapse of MDA-FUCCI2 cells exposed to three different osmolalities: 320 mOsm/kg (control), 380 mOsm/kg (Sorbitol^{+}) and 460 mOsm/kg (Sorbitol^{++}). Scale bars are 200 µm. (**B**) Number of cells at time 0 and after 90 h of imaging (1 biological repeat and N = 8, 8 and 8 number of wells for the control, Sorbitol^{+} and Sorbitol^{++} groups, respectively). (**C**) Proliferation rates are taken from the slopes of the curves indicating the number of cells as a function of time, in the range between 0 and 30 h.

4.3.2 Single cell analysis of cell cycle dynamics reveals osmotically driven impaired nuclear growth and delayed or growth arrested cell subpopulations

After the observation that hyperosmotic pressure reduced the overall cell proliferation, we next focused on single cell cycle dynamics of MDA-FUCCI2. Firstly, mitosis events were tracked from the beginning of the experiment and up to 30 hours. Single cell cycle dynamics were then recorded for the first generation of daughter cells and used in Figure 4-6 and Figure 4-7, where time 0 h for each single cell corresponds to the first frame after division of the parent cell. During the G1 phase of the cell cycle, only mCherry fluorescence is expressed in the nucleus as it is linked to the Cdt1 protein, while as soon as the S/G2/M phase starts, the mVenus fluorescence can be detected as it is linked to the Geminin protein (Figure 4-6A). Hence, by measuring the fluorescence intensity inside the nucleus over time, the duration of the G1 phase (t_{G1}, Figure 4-7D), the S/G2/M phase ($t_{S/G2/M}$, Figure 4-7C) and the whole cell cycle ($t_{cell\ cycle}$, Figure 4-7B) were evaluated.

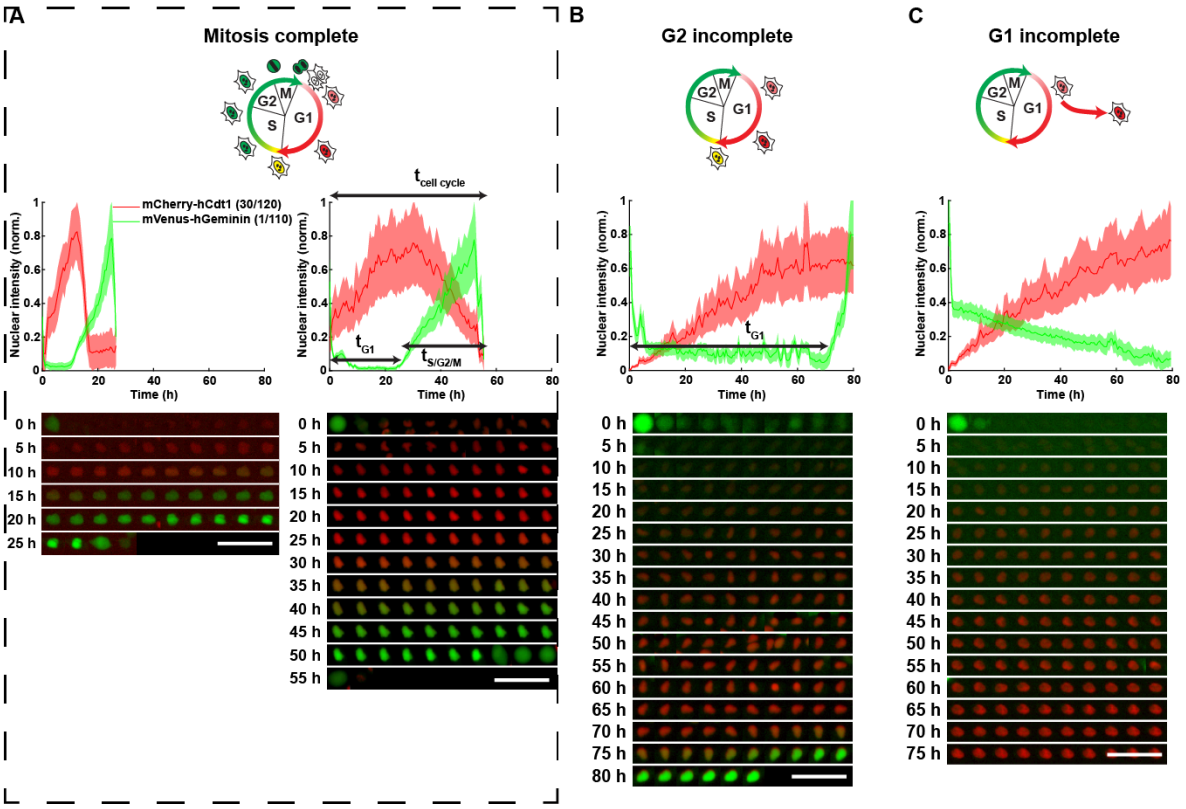

Figure 4-6 At a single cell level, increase in osmotic pressure leads to the emergence of distinct cell subpopulations.

(**A-C**) Normalized FUCCI2 fluorescence intensity inside of segmented nuclei (middle panels), corresponding fluorescence images over time (bottom panels) and cartoons (top panels) representing the cell cycle phases in three different cell subpopulation: (**A**) cell cycle with mitosis complete ("Mitosis complete"), (**B**) cell cycle with prolonged time in G1 until the cells start the S/G2/M phase ("G2 incomplete") and (**C**) the cells remain in G1 for the whole duration of the experiment ("G1 incomplete"). The time 0 h for each single cell corresponds to the first frame after division of the parent cell. Scale bars are 50 µm. The FUCCI2 cartoons were adapted from Sakaue-Sawano et al. [49], Copyright (2008), with permission from Elsevier

Under control conditions, all MDA-FUCCI2 cells took 30 h (median) to run through a full cell cycle (Figure 4-7B). Interestingly, under hyperosmotic pressure cell cycle dynamics were altered resulting in three different cell subpopulations: (i) the cells could divide but the cell cycle was prolonged ("Mitosis complete", Figure 4-6A right side), (ii) the cells had initiated the G2 phase ("G2 incomplete", Figure 4-6B) or (iii) the cells stayed arrested in G1 ("G1 incomplete", Figure 4-6C). The duration of the experiment of 90 hours corresponds to three times the cell cycle duration under control conditions.

For the cell subpopulation “Mitosis complete”, the osmotically-driven delay in the cell cycle was manifested with an increase in the duration of the whole cell cycle (Figure 4-7B), the S/G2/M phase (Figure 4-7C) and G1 phase (Figure 4-7D, “Mitosis complete”), with a delay proportional to the applied osmotic pressure. All cells of the control group completed mitosis, whereas only 67 % and 25 % of the mild PEG^{+} and high PEG^{++} hyperosmotic groups respectively managed to do so (Figure 4-7E, “Mitosis complete”). Notably, the cell cycle duration could increase up to two-folds between the control and the most osmotically stressed group (PEG^{++}).

The cell subpopulation “G2 incomplete” was found in 5 % of the cells in the PEG^{+} group and 14 % of the cells in the PEG^{++} group (Figure 4-7E). This indicates that these cells were highly delayed in their cell cycle progression, as shown by the time spent in G1, with 11 hours for the control group, 43 h for the PEG^{+} and 55 h for the PEG^{++} (Figure 4-7D, “G2 incomplete”).

Strikingly, a significant fraction of MDA-FUCCI2 cells (28 % and 62 % for PEG^{+} and PEG^{++} respectively, Figure 4-7E) did not even enter the S/G2/M phase (defined as subpopulation “G1 incomplete”) for the whole duration of the experiment . Since the cell cycle duration in the control group was 30 hours (Figure 4-7B), all the cells could have divided three times during the experiment. Instead, the cells in this subpopulation never expressed mVenus-hGeminin (1/110). For this reason, the cells in the subpopulation “G1 incomplete” are considered to be growth-arrested.

Remarkably, for the cell subpopulation “Mitosis complete” in all three experimental groups, the nuclear area increased over time up to roughly two-folds (Figure 4-7A, “Mitosis complete”). However, for both cell subpopulation “G2 incomplete” and “G1 incomplete”, under both PEG^{+} and PEG^{++}, the nuclear growth was impaired throughout the whole experiment (Figure 4-7A, “G1 incomplete” and “G2 incomplete”). Those cells were not dead as they maintained a reduced migratory activity during this prolonged G1 phase (Figure 4-8).

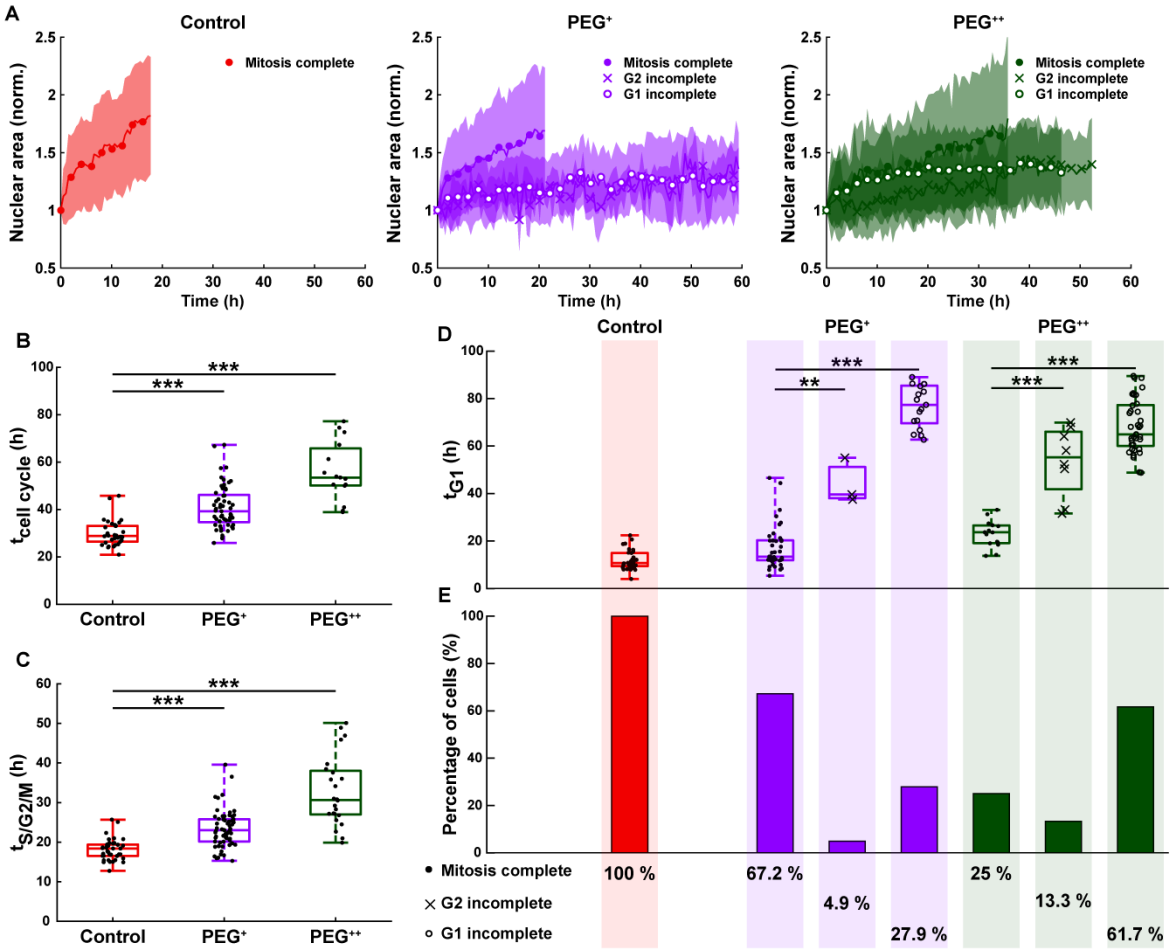

Figure 4-7 Increase in osmotic pressure leads to impaired nuclear growth and delayed or arrested cell cycle.

(**A**) Normalized nuclear area as a function of time for the three experimental groups and the three different cell subpopulations. The line is the average, and the shaded area is the standard deviation. (**B**) Duration of the whole cell cycle (time from division to division) for the cell subpopulation "Mitosis complete" (N = 34, 57 and 15 cells for the control (red), PEG^{+} (violet) and PEG^{++} (green) groups). (**C**) Duration of the S/G2/M phase, for the cell subpopulation "Mitosis complete" (N = 39, 61 and 24 cells for the control, PEG^{+} and PEG^{++} groups, respectively). (**D**) Duration of the G1 phase in the three different cell subpopulations: "Mitosis complete", "G2 incomplete" and "G1 incomplete", for the control, PEG^{+}, PEG^{++}, groups, respectively. (**E**) Fraction of cells in the three different cell subpopulations, for the groups: control, PEG^{+} and PEG^{++}.

4.3.3 Cell migration is slowed down but not arrested under osmotic pressure

To investigate whether this prolonged cell cycle and reduced proliferation correlated with decreased cell mobility, we examined single cell migration using the FUCCI2 marker. The center of the nucleus of every cell was tracked and their trajectories were recorded over time (Figure 4-8A). MSD and migration speed were analyzed for the three different groups (control, PEG^{+} and PEG^{++}). Under osmotic stress, both MSD and migration speed decreased drastically with respect to the control (Figure 4-8B, Figure 4-8C). This indicates that the cells under osmotic pressure were less migratory, stayed in a near neighborhood and moved slower than the control group, with median migration speed of 0.42, 0.18 and 0.16 µm/min for the control, PEG^{+} and PEG^{++}, respectively. In addition to reduced proliferation and prolonged cell cycle, cell migration was strongly impaired under hyperosmotic pressure.

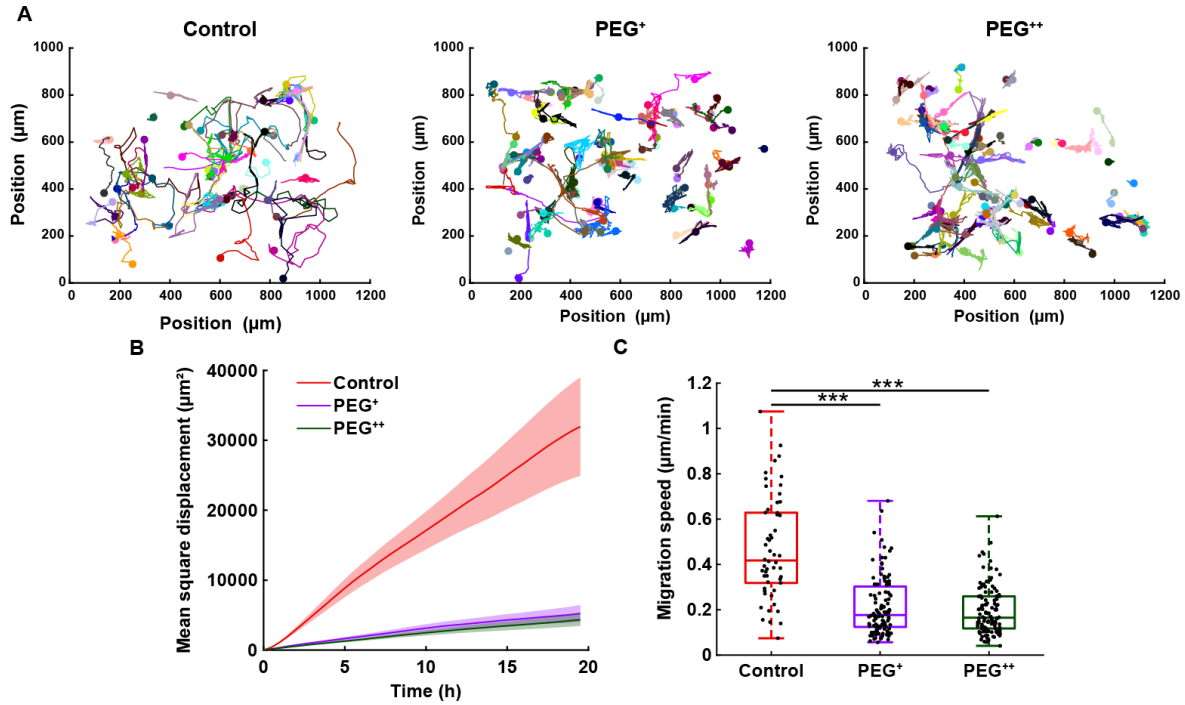

Figure 4-8 Migration is strongly reduced under hyperosmotic condition.
(**A**) Cell trajectories over the duration of the experiment (90 h), 3 biological repeats and N = 54, 111 and 118 for the control, PEG^{+} and PEG^{++} groups, respectively. Each color represents the path of one cell. (**B**) Mean square displacement of the first 20 h of the cell cycle (MSD, in µm²). The thick line represents the average MSD, and the shadow is the standard deviation. (**C**) Migration speed (µm/min) of single cells taken as the median of instantaneous cell speeds over their trajectories.

4.3.4 Expression levels of Cyclin-dependent kinase inhibitor protein p21 and proliferation marker Ki67 validate the FUCCI2 observations

The FUCCI2 reporter was used to monitor in real-time single cell cycle dynamics under osmotic stress. To further confirm the previous findings describing cell subpopulations with delayed or growth-arrested cell cycle, immunofluorescence staining was performed for the cyclin-dependent kinase inhibitor protein p21 and the proliferation marker Ki67 after 90 hours of PEG exposure. Protein expression was detected using a fluorescently labeled secondary antibody (AF467). For clarity, FUCCI2 images were artificially indicated in white and AF647 images in magenta (Figure 4-9A, Figure 4-9B). Higher levels of osmotic pressure led to a significant increase in the number of p21 positive cells from 30 % for the control, to 59 % for PEG^{+} and to 66 % for the PEG^{++} conditions (Figure 4-9C). In accordance with that finding, the number of positive cells for the proliferation marker Ki67 showed a significant drop when increasing osmotic pressure (Figure 4-9D).

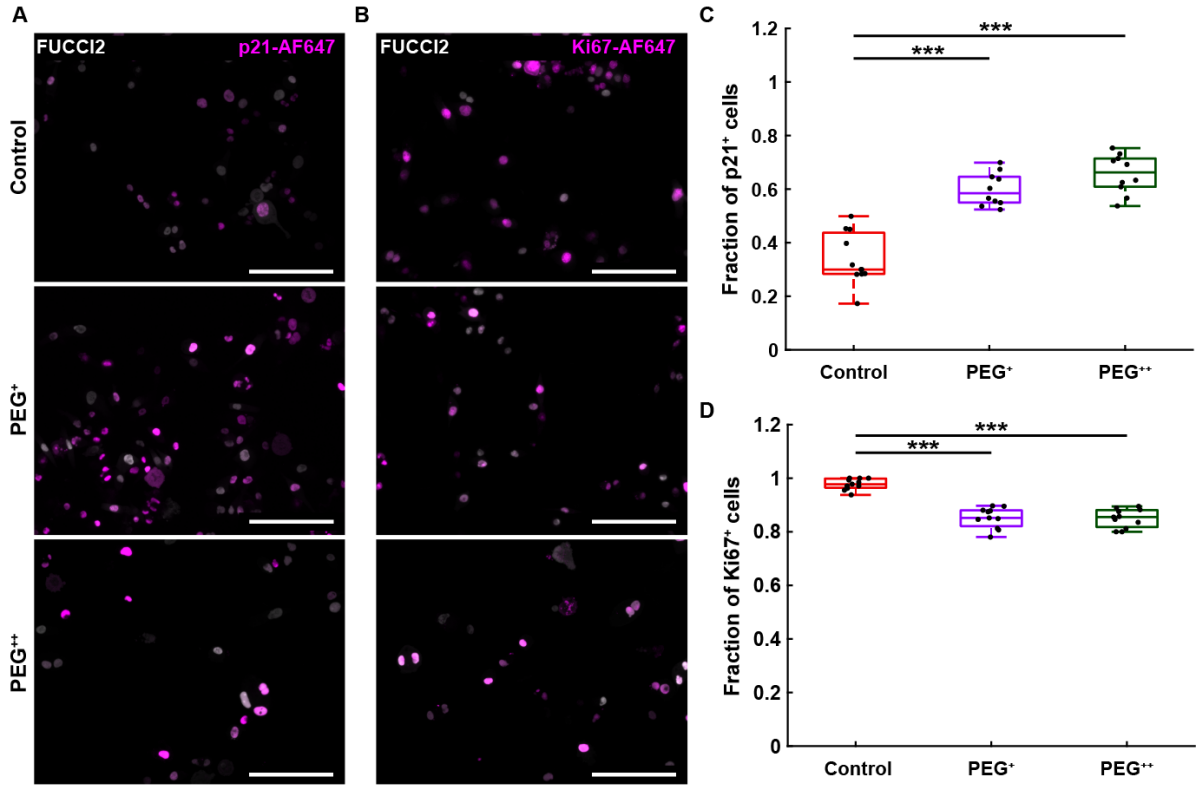

Figure 4-9 Osmotically driven delayed or growth arrested cells shows a higher expression of p21 and lower expression of Ki67.

(**A**) p21 immunofluorescence (magenta, AF647) overlaid with FUCCI2 fluorescent (artificially indicated as white) cells for the control, PEG^{+} and PEG^{++} groups, after 90 h. Scale bars are 200 µm. (**B**) Ki67 immunofluorescence (magenta, AF647) overlaid with FUCCI2 fluorescent (artificially indicated as white) cells for the control, PEG^{+} and PEG^{++} groups, after 90 h. Scale bars are 200 µm. (**C**) Fraction of p21 positive cells on three biological repeats and N = 10 wells. (**D**) Fraction of Ki67 positive cells on three biological repeats and N = 10 wells.

4.3.5 Releasing the osmotic pressure reactivates cell proliferation and migration

We next investigated whether this delay or arrest of cell cycle, accompanied by a reduction in migratory activity, was a reversible effect. To do so, after 90 h under control, PEG^{+} and PEG^{++} conditions, the media was renewed in all groups with standard cell culture media (Figure 4-10B). That is, after 90 h, all cells were exposed to the same osmotic pressure as in the control (320 mOsm/kg). The cells were then monitored for another additional 90 h and the same analyses as with the previous

experiments were performed (Figure 4-10A). The proliferation rate was measured as the slope of the curve indicating cell number as a function of time but taken at different times intervals: 60 to 90 h (cells at the end phase of the hyperosmotic pressure experiment), 90 to 120 h (early phase of reactivation), and 150 to 180 h (late phase of reactivation). The proliferation rate of the PEG^{+} group increased over time at the early phase of reactivation (90 - 120 h) (Figure 4-10C, violet) and, at the late phase (150 - 180 h) it reached values similar to the one of the control group (60 - 90 h). Cells in the PEG^{+} group also recovered their MSD (Figure 4-10D), as well as their migration speed (Figure 4-10E) and they reached values similar to the control during the first part of the experiment. To our surprise, the cells in the PEG^{++} group did not recover from the osmotic stress and the proliferation rate stayed low even at the late phase of reactivation (Figure 4-10C, green).

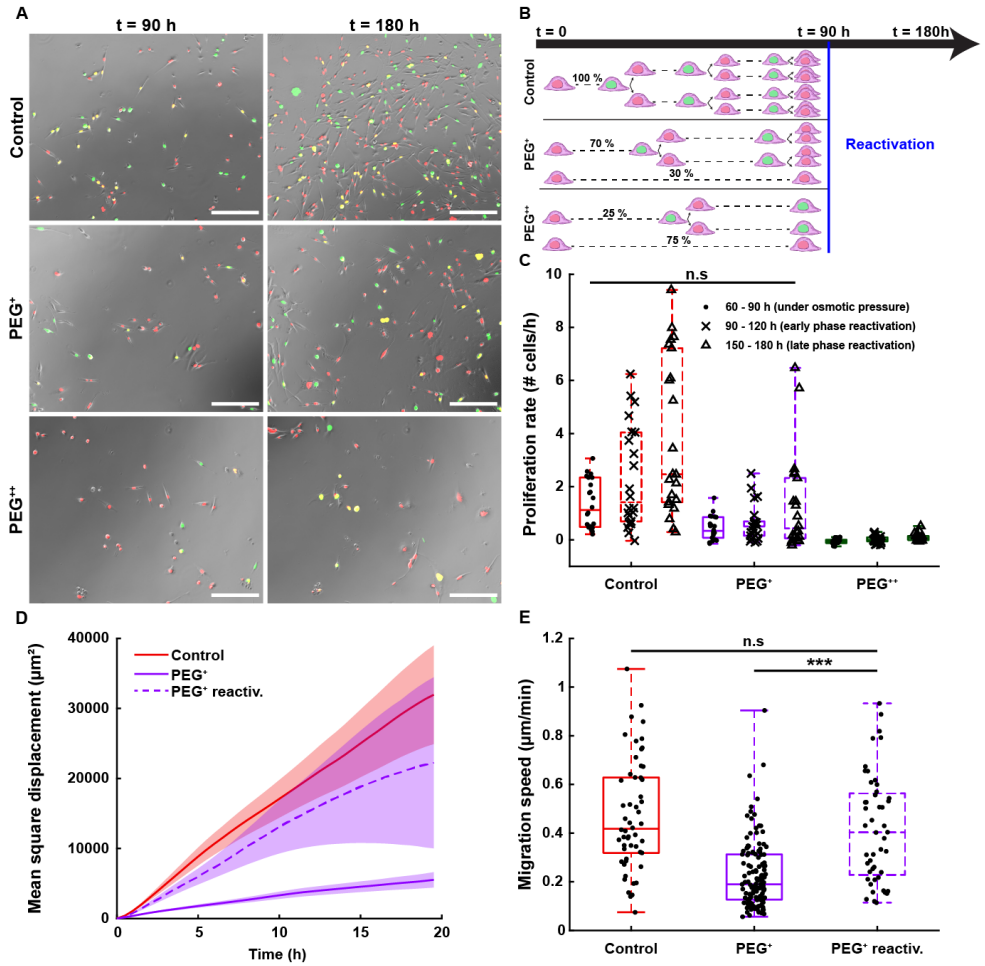

Figure 4-10 Reversible recovery of cell proliferation and migration upon osmotic reactivation.

(**A**) Time lapse of MDA-FUCCI2 cells, previously exposed to 320 mOsm/kg (control), 380 mOsm/kg (PEG^{+}) and 460 mOsm/kg (PEG^{++}) for 90 h, followed by exposure to control osmolality. Scale bars are 200 µm. (**B**) Illustration of the reactivation experiment pursuing the time lapse experiment for another 90 h but replacing the cell culture media with control osmolality. (**C**) Proliferation rates are taken as the slopes of the curves indicating the number of cells as a function of time in the range between 60 - 90 h (under osmotic pressure), 90 – 120 h (early phase of reactivation) and 150 – 180 h (late phase of reactivation), two biological repeats, N = 22 wells for each group. (**D**) MSD of cells that were previously in PEG^{+} (dashed line) in comparison with the previous data for the control and PEG^{+} groups (from Figure 4-8B). The thick line represents the average MSD and the shadow the standard deviation. (**E**) Migration speed of cells that were previously in PEG^{+} (PEG^{+} reactiv., dashed box) in comparison with the previous data for the control and PEG^{+} group (from Figure 4-8C).

In addition to the recovery of properties such as proliferation and migration, single cell cycle dynamics also returned to values resembling control conditions upon reactivation (Figure 4-11A). Similar to single cell cycle analyses during osmotic pressure, for reactivation experiments mitosis events were tracked from the beginning of reactivation and up to 30 h. Single cell dynamics were then recorded for the first generation of daughter cells. Interestingly, the duration of the cell cycle after reactivation significantly shortened with respect to the previous hyperosmotic condition and was almost fully returning to control values, with a median value of 33 h for the reactivation group against 30 h for the control (Figure 4-11B). The S/G2/M phase after reactivation was also significantly decreased and fully recovered to control values (Figure 4-11C). However, the G1 phase duration remained unchanged after reactivation and was therefore still significantly longer than the control (Figure 4-11D), although the data dispersion was strongly reduced and resembled the control values.

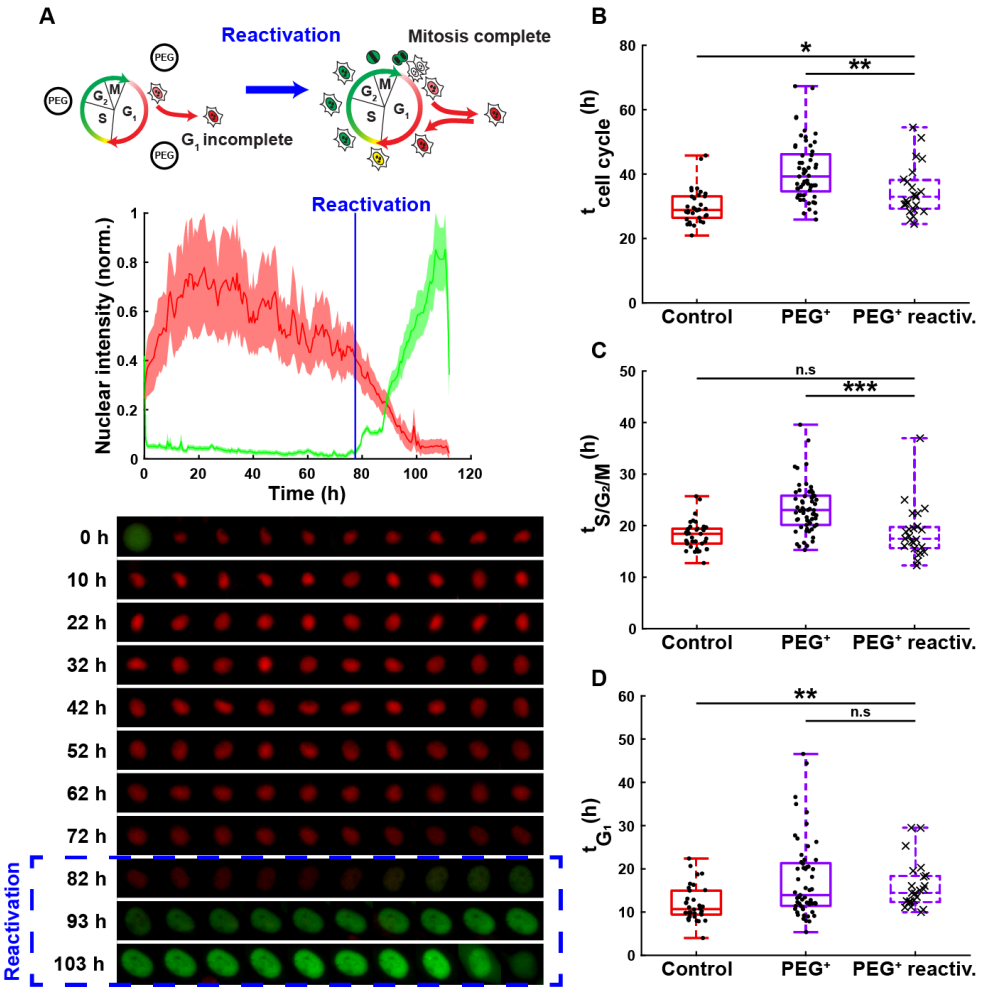

Figure 4-11 Reactivation and return to control single cell cycle dynamics upon releasing the osmotic stress.

(**A**) Cartoon of the effect of reactivation on single cell cycle dynamics (top panel), normalized FUCCI2 fluorescence intensity (middle panel), with corresponding fluorescence images before and after reactivation (bottom panel). (**B**) Duration of the whole cell cycle (time from division to division) for the cell subpopulation "Mitosis complete", before and after reactivation (N = 34, 57 and 23 cells for the control (red), PEG^+ (violet) and PEG^+ reactiv. (violet dashed), respectively). (**C**) Duration of the S/G2/M phase for the cell subpopulation "Mitosis complete", before and after reactivation (N = 39, 61 and 23 cells for the control (red), PEG^+ (violet) and PEG^+ reactiv. (violet dashed) groups, respectively). (**D**) Duration of the G1 phase for the cell subpopulation "Mitosis complete", before and after reactivation (N = 34, 57 and 23 cells for the control (red), PEG^+ (violet) and PEG^+ reactiv. (violet dashed) groups, respectively).

4.4 Discussion

Together, our findings identify osmotic pressure as a key biophysical cue modulating single cell cycle dynamics that can induce reversible growth arrest and reactivation of human metastatic cells. Quantitative time lapse imaging of single cell cycle dynamics reveals that, upon exposure to hyperosmotic stress, distinct cell subpopulations emerge with delayed or even growth-arrested cell cycle. This effect is reversible for mild hyperosmotic pressure and cells can return to regular cell cycle dynamics, proliferation and migration upon release of the osmotic pressure (see graphical summary in Figure 4-12). This is in agreement with similar phenomena observed previously with bacteria [33], yeast cells [34] and plant seeds [35, 36], but has barely been explored in the context of human cells. Our findings highlight the importance of the local biophysical microenvironment, specifically osmotic pressure, particularly in human cell niches likely to harbor non-cycling quiescent cells such as lymphatic and blood capillaries in the bone marrow.

We show that hyperosmotic stress drastically impacts highly metastatic MDA-MB-231 cells as well as weakly metastatic MCF7 human breast cancer cells, with a drop in the proliferation rate proportional to the osmotic pressure applied. These results are not specific to PEG, and analogous results are obtained when sorbitol is used as an osmolyte. This is in agreement with previous observations with prostate cancer cells, where osmotic pressure was linked to a dormant state, but only when seeded at very low (clonogenic) cell density [94]. More recently, Miermont et al. [95] also observed this drop in proliferation due to hyperosmotic stress in metastatic cell lines, including MDA-MB-231 breast cancer cells, using bulk cell analyses based only on immunofluorescence staining of proliferation markers. Since p53 has previously been related to cell cycle delay or apoptosis [102-105], the use of a mutant p53 cell line such as MDA-MB-231 could partially explain the reduced proliferation under hyperosmotic stress. However, new experiments performed with the wild-type p53 MCF7-FUCCI2 cell line, and data from the literature with the wild-type p53 T24 cell line [95], also show a reduced proliferation under hyperosmotic stress. Nam et al. [31] investigated cell cycle progression under 3D mechanical confinement using hydrogels, with an additional osmotic pressure effect, using static single cell EdU proliferation assays. They found that fast relaxing gels allowed for cell cycle progression, and this was slowed down or arrested for cells within slow relaxing gels, or within fast relaxing gels

with an additional osmotic pressure effect. However, to obtain a better understanding of the effects of osmotic pressure on single cell cycle dynamics, a quantitative real-time single cell imaging approach was lacking.

We took advantage of the FUCCI2 reporter to assess single cell cycle dynamics as well as nuclear growth in real-time, with unconfined cells under hyperosmotic conditions and upon release of the osmotic stress. FUCCI2 reporter was developed by Sakaue-Sawano et al. [49, 57] and is increasingly used to study cell cycle progression and especially quiescence [106-110]. Based on single cell analyses, we could distinguish three different cell subpopulations emerging upon exposure to mild (PEG^{+}) and high (PEG^{++}) osmotic pressure. The subpopulation “Mitosis complete” exhibited prolonged total cell cycle duration (up to two-folds longer than control conditions), with regular nuclear growth. In contrast, the subpopulations “G2 incomplete” and “G1 incomplete” showed impaired nuclear growth, accompanied by prolonged G1 phase for the former (up to five-folds longer than control conditions), and cell cycle arrest in G1 for the latter. The fraction of the subpopulation “Mitosis complete” dropped with increasing osmotic pressure (68 % and 25 %, for PEG^{+} and PEG^{++}), while an increase was observed with higher osmotic pressure in the fraction of the subpopulation “G2 incomplete” (5 % and 13 %, for PEG^{+} and PEG^{++}). Barnet et al. [111] also observed that the cell populations capable of surviving long-term dormancy were heterogeneous and contained cycle-arrested cells mixed with proliferating cells. The emergence of these different subpopulations of cells under the same biophysical microenvironment highlights the power of single cell analyses in real-time to better understand the dynamics of growth arrest and reactivation of highly proliferative human metastatic cells.

These results were validated with bulk analyses of a collective of cells based on immunofluorescence staining. The osmotic stress resulted in a drop in the proliferation marker Ki67 and an increase of the cyclin dependent kinase inhibitor protein p21 expression, which was proportional to the osmotic pressure applied. It has been shown that p21 expression can be an indicator for cell cycle arrest while inhibiting apoptosis [112]. This cell cycle arrest caused by high p21 expression can happen in both G1 phase, but also in G2 phase by mediation of cyclin B1 degradation in presence of DNA damage [113, 114]. In addition, the proliferation-associated protein Ki67 is a common method to visualize growth arrested cells [40, 115, 116]. Our immunofluorescence results show that 80 % of cells under mild osmotic pressure are

Ki67 positive, while the other 20 % are Ki67 negative and therefore not cycling (Figure 4-9D). This bulk analysis correlates with our findings from the dynamic single cell FUCCI analyses in Figure 4-7E, with a fraction of 28 % cells in G1 incomplete. Both p21 and Ki67 results on bulk analyses agree with the trends detected by summing up the results of the FUCCI2 single cell tracking. Here we quantified a decreasing subpopulation "Mitosis complete" (67 % and 25 %), increasing subpopulation "G2 incomplete" (5 % and 13 %) and "G1 incomplete" (28 % and 62 %), from mild (PEG^{+}) to high (PEG^{++}) osmotic pressure.

Under hyperosmotic stress, cell migration decreased drastically for both mild and high osmotic stress. It has been previously reported that hyperosmotic stress was involved in a reduction or suppression of protrusive activity [117] which is necessary for cells to migrate [118]. An increase in osmotic stress proved to be responsible for a reduction of lamellipodia area [119]. Conversely, a reduction in osmotic stress, enhanced lamellipodial formation, as shown by an epithelial gap closure assay [120]. These reported effects of osmotic pressure on filopodia and lamellipodia formation could explain our findings of reduced cell migration under hyperosmotic stress.

An essential characteristic of the herein-described cell cycle arrest and reactivation is its reversibility. For the mild hyperosmotic pressure condition, the MDA-FUCCI2 cells resumed proliferation, migration and partially cell cycle dynamics upon releasing the osmotic pressure. Unlike previous studies [94], this is to the best of our knowledge the first study quantitatively monitoring the reversibility of the cancer cell cycle arrest and return to active proliferation, in real-time and at a single cell level.

One possible mechanism linking osmotic regulation with cell behavior could be the cell and nuclear size. In the context of mesenchymal stem cell biology, it has been shown that variations in external osmotic pressure can induce changes in cell volume, intracellular molecular crowding as a result of water efflux, changes in cell stiffness and ultimately impact mesenchymal stem cell differentiation in the osteogenic or adipogenic lineage [89]. Furthermore, a recent and important study shows that cell division requires the nuclear size-dependent dilution of the cell cycle inhibitor retinoblastoma protein, which is enabled by nuclear growth during the G1 phase [121]. Remarkably, in our study we show that cells exhibiting impaired nuclear growth did not complete mitosis, under both mild and high hyperosmotic pressure; while cells that divided, showed a nuclear growth comparable to control conditions. These findings

suggest that a biophysical cue such as osmotic pressure could modulate single cell cycle dynamics by impairing nuclear growth.

While the focus of this chapter has been the effect of osmotic pressure on single cell cycle dynamics using highly proliferative human metastatic cells as a model system, its implications can be extended to a broader physiological context. It is known that gradients in osmotic pressure and hydrostatic pressure drive fluids out of arterioles and back into the venules [84][86]. Such gradients could contribute to the spatial distribution of quiescent hematopoietic stem cells (HSC) in the neighborhood of capillaries in the bone marrow [37][38]. From a disease state point of view, growth-arrested human metastatic breast cancer cells have been associated to stable vasculature, while reactivation and proliferation have been linked to sprouting new vessels [13]. Sprouting neovasculature is characterized by a looser and more permeable capillary wall, resulting in a lower osmotic pressure gradient [122]. These findings describing the effect of osmotic pressure on reversible cell growth arrest and reactivation can have implications in a broader context such as stem cell quiescence vs. proliferation, or human disease like cancer dormancy and metastasis.

4.5 Graphical summary

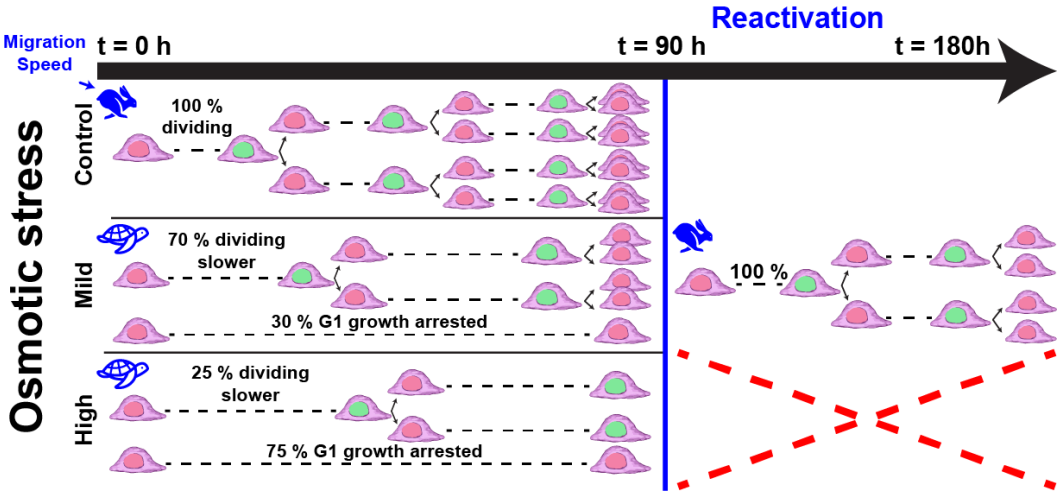

Figure 4-12 Effect of osmotic stress on breast metastatic cells

4.6 Limitations

The presented chapter shows the *in vitro* implication of hyperosmotic stress microenvironment and its impact on breast cancer cell dormancy. We show the impact of hyperosmotic stress on one of the most aggressive metastatic cell lines and could

demonstrate that under certain conditions, the cell cycle was greatly delayed or completely arrested, in a reversible fashion.

Despite using more than one cell line with the MDA-FUCCI2 and MCF7-FUCCI2, the use of cell lines greatly limits the reach of our results and conclusion. Pursuing similar analyses with primary cells or with many different cancer cell lines would be highly beneficial.

Relying on FUCCI2 cell lines is also a limitation since it can represent a lot of work to generate the cell line in a stable manner. This work was done in collaboration with colleagues at the Charité University Hospital.

The experiments also required access to sophisticated and stable hardware such as a completely motorized EM with a top stage incubator for long term experiments (up to 8 days for the reactivation experiments).

Moreover, despite the efforts we made to observe, quantify and document events in the most accurate way the effect of hyperosmotic stress on breast cancer cell dormancy, the work in this thesis does not provide a mechanistic explanation of the biology behind the observed results. We believe the work done in this chapter is still beneficial for starting more biologically oriented research of the effect of osmotic stress on breast cancer cell.

Finally, the fact that we performed all our experiment in a perfectly controlled, *in vitro* 2D tissue culture plate is a rough simplification of what the microenvironment can look like *in vivo*.

By lowering the complexity of the system to a 2D glass plate, we could model and focus one specific effect of an otherwise more complete environment. How the response to osmotic stress would interact with other biophysical cues of the microenvironment or even other cells present in the system remains unknown and to be discovered.

Chapter 5 Single cell under fluid flow in a microfluidic device

♫ “I can go… with the flow,
don't say it doesn't matter anymore.”

Go with the flow, Queens of the stone age

Cancer cells can metastasize to secondary organs at early stages of the disease. Metastatic cancer cells travel through capillaries characterized by gradients in both osmotic pressure and fluid flow. Chapter 4 was dedicated to the role of osmotic pressure and here we investigate the effect of sinusoidal fluid flow, and its resulting shear stress derived from computational fluid dynamics, on metastatic cell cycle progression, migration, cell and nuclear volume as well as shape.

5.1 Introduction

There are many molecular pathways that drive metastasis [123], but it is becoming more acknowledged that mechanical forces can also be responsible for tumor progression [124-126]. Part of these mechanical cues are fluid flow-based cell responses. This is because before creating a metastasis, the tumor cells are exposed to three main body fluids: blood, lymph and interstitial fluid [127-129]. The terms “hemodynamic” or “mechanical” theory describe the notion that fluid-based mechanics could shape metastasis. It was thus shown that the frequency of metastasis in height classical target organs correlated with organ arterial blood flow [130]. In the context of brain cancer, it has been reported that fluid flow could stimulate invasion as well as proliferation [131, 132]. On the other hand, after extravasation it was demonstrated that specific cancer cells could remain dormant for years to decades in niches [13]. Metastatic onset or dormancy requires physical intravascular arrest of DTCs before they actively extravasate to the interstitial matrix , where they can stay dormant [10] or generate life-threatening metastasis [134].

Given that the bone marrow (BM) is a preferential site for breast cancer metastasis and that stable microvasculature can provide a dormant niche [13], this region appears

to be of great interest to study the impact of fluid flow on breast cancer cell dormancy. The BM microvasculature is composed of a fairly irregular network of connected sinusoidal microvessels, located in the BM cavities of bones [135, 136]. In long bone, these microvessels connect to a complex and irregular network of sinusoidal capillaries [37, 135]. Recently, intravital two-photon imaging was used *in vivo* to quantify blood flow dynamics and velocities in these sinusoidal capillaries [137], thus providing an accurate basis for determining fluid flow profiles in this region. To mimic these condition, microfluidics is an important technique that allows the control over a tunable fluid flow and shear stress, while monitoring the behavior of cancer cells *in vitro* [138, 139].

To the best of our knowledge, the role that shear forces exert on tumor cell dormancy has not been documented. Whether DTCs perivascular niches [13] that can create a chemo-resistant environment for dormant tumor cells [140] for example originate from extravasated cells that went through specific flow profiles during endothelial remodeling [141] remains unknown. It would be of great interest to know if tumor cells could be localized and discriminated solely based on fluid flow profile.

Here, we hypothesize that the fluid flow and shear stress can play a role in human cell niches likely to harbor non-cycling quiescent cells by altering their cell cycle dynamics, migration and morphology.

In a similar way to the osmotic pressure study, we use the highly proliferative human metastatic cell line MDA-MB-231 with FUCCI2 (MDA-FUCCI2) to perform quantitative time lapse imaging of the different phases of the cell cycle at a single cell level.

We investigate the effect of different levels of fluid flow mimicking regions such as the sinusoidal capillaries near the bone marrow. To do so, we use a microfluidic device and study the time-resolved single cell cycle dynamics, migration, cell and nuclear volume/morphology, for several days. The level of fluid control, and the ability to capture single cell for 3D time lapse imaging makes the microfluidic a unique platform suitable for our experiments.

5.2 Materials and methods

5.2.1 Cell culture

Cell culture was performed exactly as described above in section 3.2.2.

5.2.2 Cell actin staining

Cell actin staining was performed exactly as described above in section 3.2.3

5.2.3 Fabrication of polydimethylsiloxane (PDMS) microfluidic devices

The aim of the microfluidic device is to trap and isolate single cells for long time lapse imaging (> 3 days) and investigate their behavior under different fluid flow conditions. For this we need specific features that consist of traps in microfluidic channels, and our microfluidic devices (Figure 5-3) were inspired and adapter from previously reported design [142, 143].

Wafer master mold fabrication

A silicon wafer (Siegert wafer, #BW14001) was used to create the master mold of 30 µm in height via soft photolithography (Figure 5-1A). Briefly, the original empty wafer was dehydrated at 200 °C for 30 minutes and then spin-coated with 4 mL SU-8 photoresist (Microchem, SU8-3025) at 500 RPM for 15 seconds followed by 2600 RPM for 30 seconds (Laurell, #WS-650-23). The wafer was then soft-baked and inserted into the mask aligner (KLOE, UV-KUB3) along with the film mask (Micro Lithography Services) containing our design for ultraviolet (UV) exposure at 35 mW/cm² for 6 seconds. The wafer was then post-baked and developed (Micro resist technology, #mr-Dev 600) to remove the non-cured SU-8. A final hard bake was performed at 200 °C for 30 minutes and the wafer was silanised to avoid PDMS adhesion. This was done by having the wafer overnight inside a 150-mbar desiccator with 50 µL of 1H,1H,2H,2H-Perfluorodecyltrichlorosilane (abcr, #AB111155). Every wafer contains 10 designs to create 10 individual chips. The channels inside the microfluidic device can be visualized in Figure 5-1B.

Microfluidic device to trap single cell

To produce the microfluidic chips, PDMS and curing agent (Dow Corning, Sylgard 184 Silicone Elastomer Kit) were mixed with a 10:1 ratio (70 g PDMS, 10 g linker). The mixture was degassed for 30 minutes in a 150-mbar desiccator and then poured into the wafer master. The mixture was degassed once more for 15 minutes in a 150-mbar desiccator and cured at 80 °C for 2 h. The 10 designs were cut out from the cured PDMS and holes for the inlet and outlet were made with a 1.5 mm biopsy puncher (Kai Europe GmbH). A reservoir made from a cut 1000 µL pipette tip was placed above the inlet, sealed with liquid PDMS and cured at 80 °C for 30 minutes. The PDMS microfluidic devices and the cover slip (24 x 40 mm, Thermo Fischer, #10180035) were

then placed in a plasma cleaner (Plasma Cleaner PDC- 002-CE, Harrick Plasma) at 0.6 mbar for 60 seconds. Following the plasma activation, the PDMS and the cover slip were attached manually and kept on a hot plate at 60 °C for 30 minutes to help the binding. Before an experiment, the microfluidic device was sterilized under UV radiation for one hour.

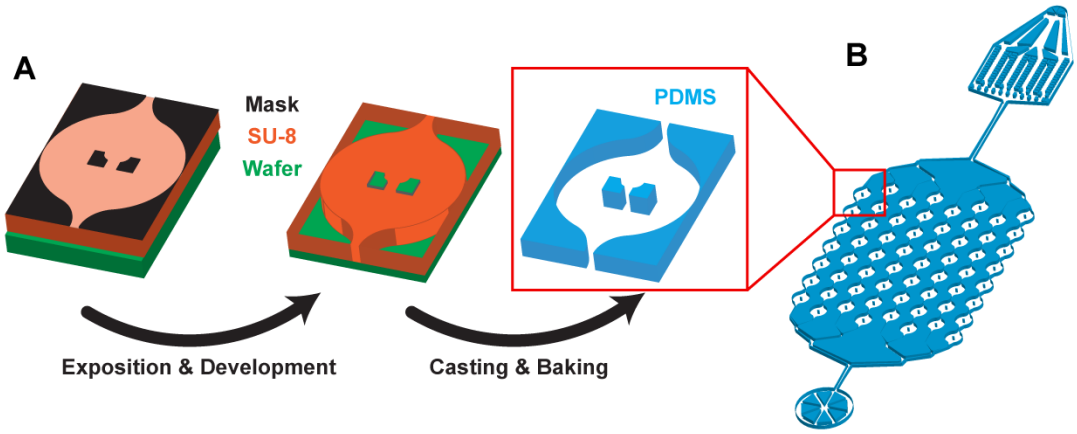

Figure 5-1 Wafer and microfluidic device fabrication process.
(**A**) A silicon wafer was spin-coated with SU-8 at 30 µm thickness, then exposed to UV through a mask containing the design of the microfluidic device. After development to remove any non-cured SU-8, a wafer master mold was generated. Liquid PDMS was then poured into the wafer master mold and baked to create the microfluidic device. (**B**) Overview of one complete microfluidic device.

Complete setup

A microfluidic device can be seen in Figure 5-3A. It consists of 8 parallels channels (colored with red dye) accounting for 60 traps in total. Each trap contains two posts that block cells and allow single cells to be captured in the chip (Figure 5-3B).
Firstly, the microchannels were flushed with a cell culture media solution (200 µL) with centrifugation for 10 minutes at 900 RPM. The microfluidic device with its channels filled with cell culture media was then placed in a stage top incubator at 37 °C and 5 % CO_2 (Okolab, UNO-T-H-CO2). We used an aluminum custom-made sample holder to make sure no movement will occur during the long time lapse imaging (Figure 5-2B). The outlet was then connected with a metal connector to a 1 mL (control and Flow^{+}) or 2.5 mL (Flow^{++}) syringe (Agilent, #5190-1530 and #5190-1534) mounted on a pump (Chemyx, Fusion 200) in withdraw mode (Figure 5-2A). Once everything was

connected, the device stayed was kept 30 minutes to reach the targeted temperature and concentration of CO_2 inside the chamber and inside the microfluidic device.

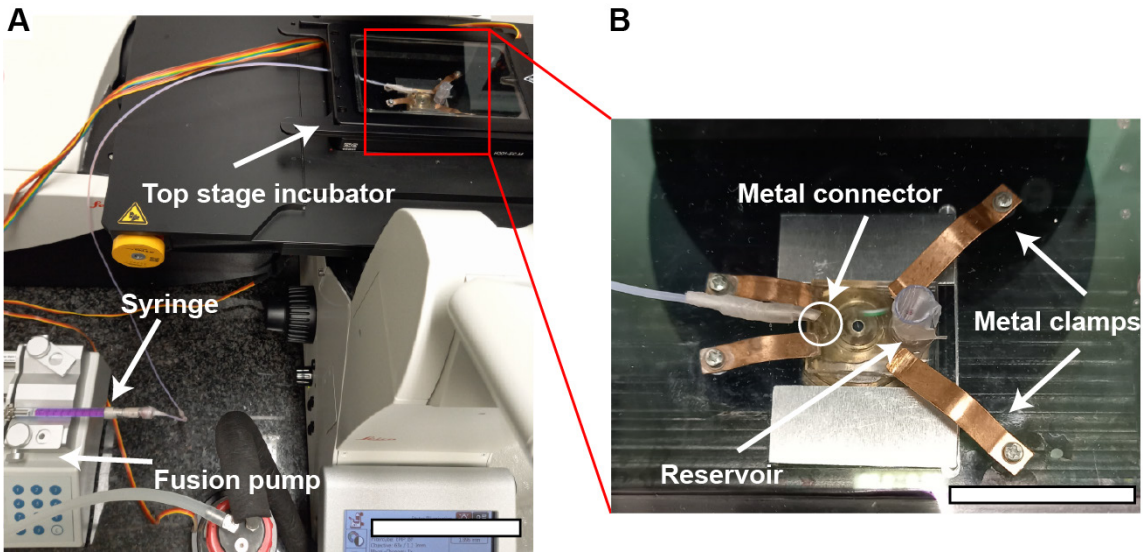

Figure 5-2 Complete setup of the microfluidic device with syringe and pump. (**A**) Top stage incubator mounted on a confocal SP8 microscope containing the microfluidic device. The microfluidic device is attached to a syringe mounted on a pump in withdraw mode to create the flow. Scale bar is 12 cm. (**B**) Close-up view of the inside of the top stage incubator. The microfluidic device is mounted on a custom-made holder with four metal clamps to prevent movement during time lapse. The outlet of the microfluidic device is attached to the syringe with a metal connector to ensure a tight connection and avoid formation of air bubbles. Scale bar is 4 cm.

Microfluidic device operation

The complete setup was prepared and checked so that no apparent air bubbles were present in any of the channels. Then the process of trapping the cells inside the microfluidic device was started. From the master cell suspension at 600 000 cells/mL that received the SiR-Actin, another cell suspension was created by dilution to reach 100 000 cells/mL. The microfluidic device operation is divided in four steps (Figure 5-3B):

(i) Insertion. From the cell suspension of MDA-FUCCI2 stained with SiR-Actin, 50 µL were taken (~ 5000 cells) and inserted into the reservoir. The flow rate was set to 20 µL/min for 5 minutes for maximum trapping efficiency.

(ii) Capture. The streamlines in the microfluidic device will go around and between the two posts until a suspended cell occupied the space between

the posts. After this point, other cells would only go around the posts and fill the next trap.

(iii) Adhesion. A visual check with the microscope was done to ensure that at least 80 % of the traps were filled since this yielded enough single cells per experiments. The flow rate of the chosen experimental group was then applied (control: 0.02 µL/min, $Flow^{+}$: 0.1 µL/min and $Flow^{++}$: 0.2 µL/min, please see the section 5.2.10 for more details on the choice of the flow conditions). The remaining cells in suspension still in the reservoir from the initial insertion were removed by three exchanges of media. Finally, media containing SiR-Actin was added until the top of the reservoir and parafilm was added to prevent evaporation. The trapped suspended cells (mechanically trapped between the two posts) were then incubated overnight to allow adhesion.

(iv) Migration and proliferation. Once the cells adhered, they migrated within the trap and proliferated while being imaged during time lapse.

During the time lapse imaging, two containers filled with Millipore water were inserted inside the top stage incubator (Okolab, UNO-T-H-CO2) to have a 100 % humid environment along with the 5 % CO_2 mixture and the 37 °C temperature, thus resembling the main incubator used for regular cell culture and avoiding media evaporation.

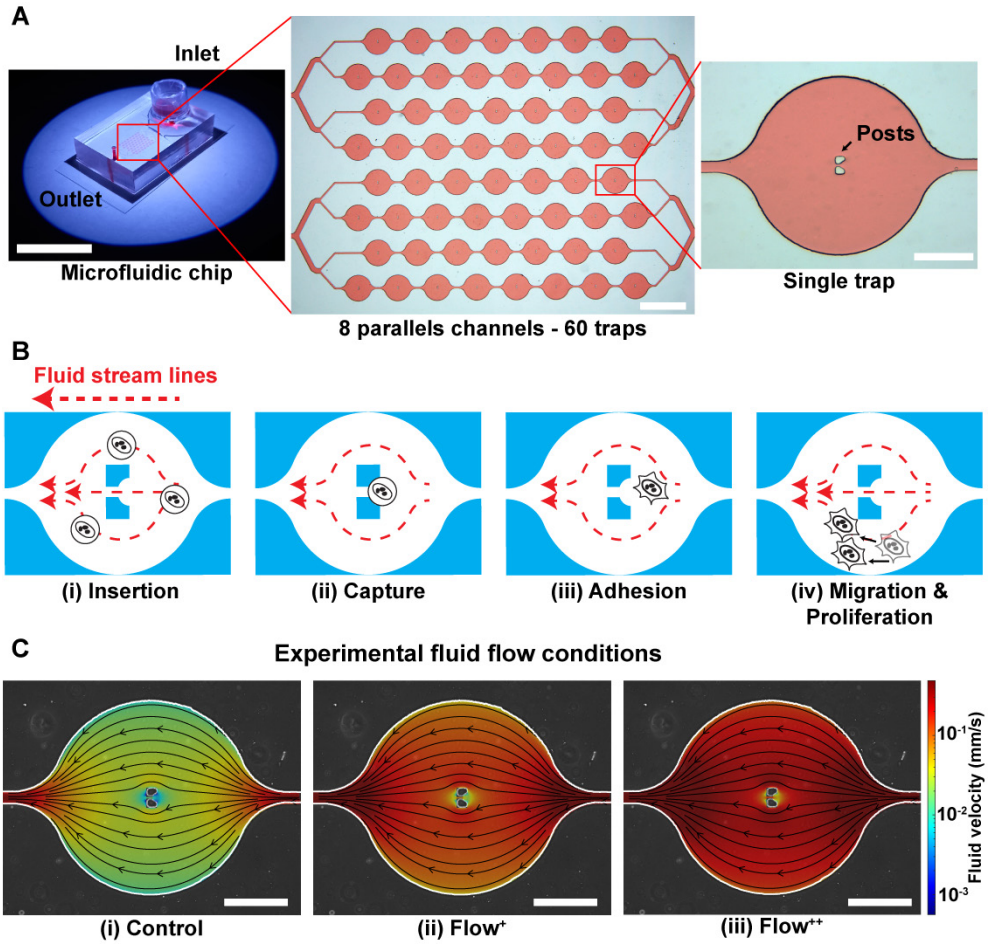

Figure 5-3 Microfluidic approach for high efficiency trapping of single breast cancer cells.

(**A**) Bright field image of the PDMS microfluidic chip used to trap MDA-FUCCI2 cells. It consists of 8 parallels channels (colored with red dye) accounting for 60 traps in total. Each trap contains two posts that block cells and allow single cells to be captured in the chip. From left to right, scale bars are 20 cm, 1 mm and 200 µm. (**B**) Process of trapping cells inside the chip: (i) cells are inserted from the reservoir and flushed inside the chip with a high fluid flow at 20 µL/min (insertion) until (ii) the cells are trapped within the two posts (capture). (iii) Once enough cells are occupying the traps (>80 %), the flow rate is set at the experimental fluid flow condition (Control, Flow^{+}, Flow^{++}) and cells are incubated overnight to allow adhesion. (iv) Cell migration and proliferation is monitored over time under the different experimental fluid flow conditions. (**C**) Overlay of phase contrast image of one single trap with fluid streamlines and fluid velocity in the three experimental fluid flow conditions, corresponding to two levels of sinusoidal fluid flow, Flow^{+} (0.1 µL/min) and Flow^{++} (0.2 µL/min), and Control (0.02 µL/min).

5.2.4 Time lapse experiments protocol

Every experiment was done in parallel on two independent top stage incubators: (i) in an epifluorescence microscope (Zeiss, AxioObserver 7) and (ii) in a confocal microscope (Leica, SP8). While both the epifluorescence and confocal microscope could provide information about the cell cycle dynamics and migration, only the confocal microscope was able to resolve the nuclear and cell volume over time (Figure 5-4). Coupled with the computational fluid dynamics (CFD) simulation, an accurate estimate of the wall shear stress on the cell membrane was computed as described in 5.2.5.

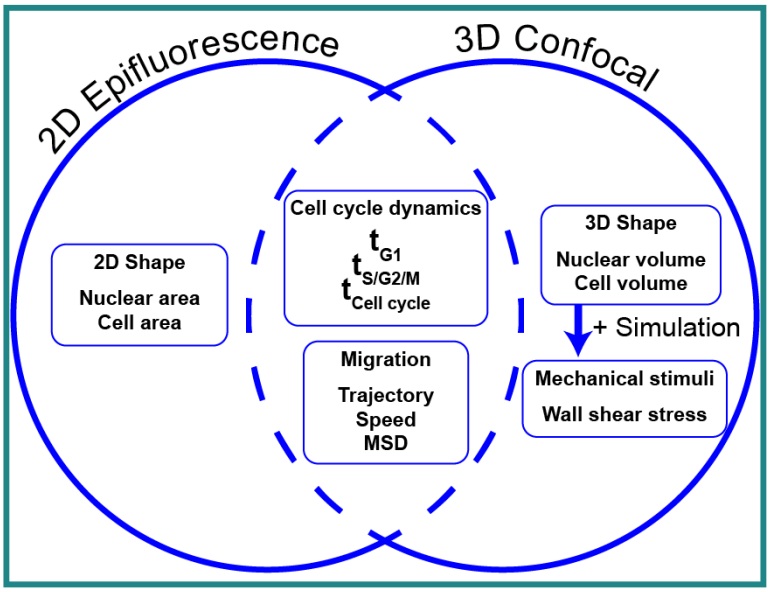

Figure 5-4 Description of the readouts available from both epifluorescence and confocal microscope.

5.2.5 2D time lapse image acquisition

The 2D time lapse image acquisition was performed as described in section 3.2.4.

5.2.6 3D time lapse image acquisition

The 3D time lapse images were acquired using a Leica SP8 confocal microscope and a 63x, 1.2 NA water immersed objective (Leica, #11506356). An automatic water immersion micro dispenser (Leica, #15640019) was used along with the objective to prevent drying and allow for time lapse imaging for 90 h. For every trap, a 2x2 tile image was acquired (with 10 % overlap) and then merged using the LASX (Leica) software. Fluorescence channels mVenus, mCherry and SiR-Actin were recorded with

1 % laser intensity at 488, 552 and 638 nm laser excitation. Emission was recorded for the three channels as follow: (i) mVenus [493-547 nm], (ii) mCherry [588-633 nm] and (iii) SiR-Actin [651-707 nm]. Sequential acquisitions were performed to record all channels independently, and bright field transmission images were also obtained. Voxel sizes were 0.481 µm/pixel for X and Y direction whereas 1 µm/pixel resolution was achieved for the Z direction.
3D time lapse images were acquired with intervals of 2 h for 90 h.

5.2.7 Single cell tracking and cell cycle dynamics

The single cell tracking, and quantification of cell cycle dynamics was done as previously described in section 4.2.6 using the FUCCItrack software.

5.2.8 Deep learning 3D multi-channels time lapse segmentation

For this thesis, 3D time lapse multi-channel images were recorded as follows: mCherry (red), mVenus (green) and the SiR-Actin (magenta). Considering the large amount of data to be processed for every cell and for every experimental group, a deep learning approach was chosen to help automatically segment the respective channel. The pipeline is described as follows and uses both MATLAB for the preparation and DragonFly software (ORS, V2021.1.0.977) for the actual DL training and testing.

Deep learning training

The DL training needs two inputs: (1) the raw images to be processed and (2) the expected segmentation for every image (called ground truth). With these two, the neural network was trained to the point that it can accurately make predictions on a new dataset and perform a semantic segmentation.

Raw data preparation

From FUCCItrack, an additional module was created specifically to prepare the 3D dataset for segmentation and deep learning training. Using the single cell tracking data, each single cell was localized, and the field of view was automatically cropped to produce 3D stack time lapse images stored in one big tif file per cell. This step is crucial as it allowed us to reduce the size of the dataset enormously by only keeping the essential part of the field of view.

Ground truth (SiR-Actin)

A total of seven different time lapse cells were used for the training of the SiR-Actin channel, meaning that manual segmentation was performed for 1710 slices (Cell

#1: 130, Cell #2: 153, Cell #3: 341, Cell #4: 336, Cell #5: 250, Cell #6: 251 and Cell #7: 249 slices). For every slice, two labels were created: (i) the SiR-Actin label from the cell and (ii) the background.

Ground truth (FUCCI2)

Only a total of 4 different time lapse cells were used for the training of the mCherry and mVenus channels since it yielded better segmentation results than the SiR-Actin channel. It means a total of 434 slices (Cell #1: 77, Cell #2: 93, Cell #2: 129 and Cell #3: 135 slices) were manually segmented and used.

Creation of the training dataset

To have the best training results, it is often better to avoid unbalanced label counts so that the number of pixels in each label is as close as possible to each other. This is a way to avoid artifacts in the learning process that would see one label predominantly. To achieve this, the 2D slices were cropped down to the minimum region of interest (ROI) that contains the ground truth and removing as many pixels corresponding to the background as possible. Data augmentation was also used by flipping/rotating and scaling the original dataset to create more training images.

Network architecture and training parameters.

The U-net neural network was used to perform the 3D time lapse segmentation. The dice loss function from the DragonFly software (it calculates the difference between the outcome predicted and the ground truth, 0 means bad prediction and 100 % perfect prediction) was used. The training was stopped when it reached more than 98 % accuracy. Considering the three channels to be processed, there were three independent neural networks that were trained during the thesis, one for the SiR-Actin, one for mCherry and one for mVenus.

Deep learning testing

Once the neural networks were trained with the desired accuracy, new cells (never seen by the neural networks) could be prepared like described (in the raw data preparation section) and run through the neural network (the testing). The final datasets with 3D segmented cells were always checked manually to make sure there was no incorrect segmentation, and the overall DL process shortened the processing time by several orders of magnitude. Some results of 3D time lapse segmentation can be seen in Figure 5-5 with each column corresponding to individual cell time lapse.

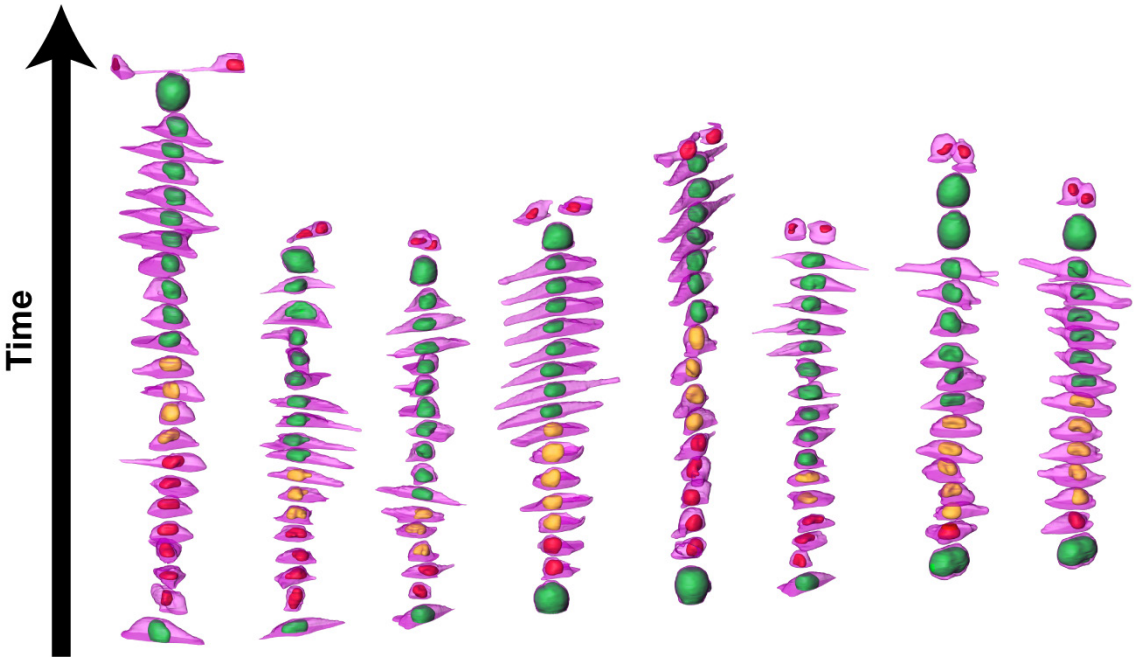

Figure 5-5 3D time lapse multi-channel segmentation reveals cell and nuclear volume of breast cancer cells.

3D time lapse rendering showing the evolution of the cell volume (magenta, SiR-actin) along with the nuclear volume (red, yellow and green for the FUCCI2 system) in the experimental control group.

5.2.9 Computational fluid dynamics simulation

In addition to experimental 3D time lapse imaging, CFD was performed to estimate the fluid velocity inside the microfluidic device and to compute the wall shear stress (WSS) for each cell and for each timepoint automatically. The CFD simulations were performed using OpenFOAM (Open-Source Field Operation and Manipulation) and the results visualized with the open-source software ParaView.

3D Model and assumptions

In the CFD simulation performed in the thesis, the goal was to solve the Navier-Stokes equation that governs fluid dynamics in the microfluidic device. There are several hypotheses that were assumed: (i) the fluid is Newtonian and (ii) incompressible. In addition, (iii) all variables (pressure and velocity) are independent of time (steady state), (iv) there is no leak and (v) there is an equal distribution of the flow between all channels of the microfluidic device. Gravitational forces were neglected, and the flow was considered laminar (Re << 1). The base 3D model (without cell) corresponds to one trap with two posts in the middle since all traps are identical in the microfluidic

device. The flow at the inlet was obtained by assuming an equal repartition between the different channels of the microfluidic device and by dividing the flow of the syringe by eight (number of parallel channels).

A simulation was performed for each z-stack acquired by confocal microscopy and for each timepoint of the assay. The simulations were parametrized and interfaced with OpenFOAM automatically using a custom-made script written in Python 3.8.6: Automated Simulation On Cluster (ASOC). From the SiR-Actin channels, each cell was 3D modelled by segmenting the z-stacks and generating the surfaces was done using the Amira software (“Generate surface” module) that uses the marching cube algorithm [144] to create a mesh from 3D datasets.

The cell surface was modeled as a rigid surface as first approximation. Since the cell shape changes with time, the updated shape at each time point obtained from experiments was used to calculate the shear stress on the cell surface.

Choosing the right mesh

The models (the trap and the cells inside, Figure 5-6A) were meshed using the cfMesh library within OpenFOAM and were of cartesian type. The mesh was mostly composed of uniform elements of 4 µm, locally refined to 2 µm around the central posts and to 1.5 µm around each cell boundary (Figure 5-6B). Since the wall shear stress calculation depends on the element size close to the cell, meshing like this was found to maintain sufficient accuracy while improving the simulation time by an order of magnitude with respect to a 1.5 µm uniform elements everywhere. A no-slip condition was imposed on the walls of the trap and on the cell boundary, meaning that the velocity at this interface is set to 0.

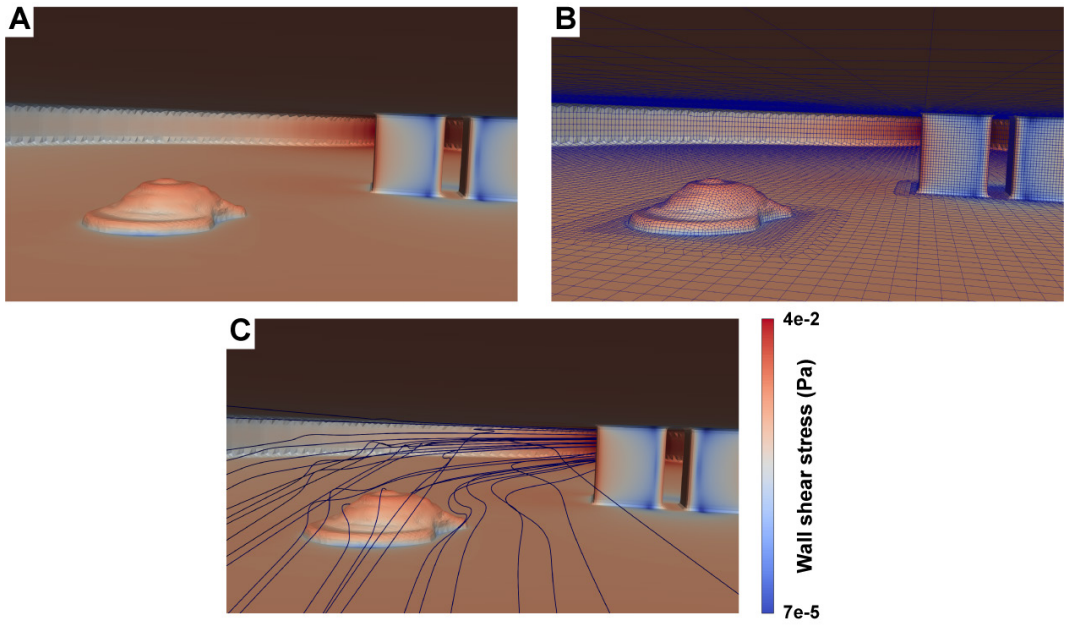

Figure 5-6 CFD simulation on real cell shape reveals wall shear stress experienced by metastatic cell.

(**A**) View from within the 3D CFD simulation model containing a cell inside a trap with the color corresponding to the wall shear stress. (**B**) Corresponding view of the mesh at the surface used for the computation. The mesh is finer around the cell and coarse further away to reduce computation time. (**C**) Overlay of the wall shear stress with the fluid streamlines around the cell.

5.2.10 Physiologically relevant fluid flow

To investigate the effects of fluid flow on metastatic breast cancer cells, several experimental groups were defined as follows. The control group (flow rate: 0.02 µL/min) was defined as the minimum value of flow inside the microfluidic device that would permit cell proliferation similarly as in the 96 glass well plate experiment (section 4.3.2) and avoid cell death by providing a continuous flow of nutrients. In addition, two experimental fluid flow conditions were chosen ($Flow^{+}$: 0.1 µL/min and $Flow^{++}$: 0.2 µL/min) to create a region of fluid velocity that resembles that in sinusoidal capillaries in the bone marrow microvasculature [137].

5.3 Results

5.3.1 Fluid flow accelerates cell cycle by decreasing S/G2/M duration

Under control conditions, all MDA-FUCCI2 cells took 30 hours (median) to run through a full cell cycle (Figure 5-7A, D), similarly of the control in Chapter 4 (Figure 4-7B).

Interestingly, under higher fluid flow (Flow^{+}) cell cycle dynamics (t_{G1}, $t_{S/G2/M}$ and $t_{Cell\ cycle}$) were not altered and no significant difference could be measured compared to the control group (Figure 5-7B, C and D). However, the highest fluid flow (Flow^{++}) triggered a response in cell cycle dynamics resulting in a slight significant increase of t_{G1} (+1.5 h, Figure 5-7B) and a more pronounced decrease in $t_{S/G2/M}$ (-2.8 h, Figure 5-7C) leading to a significant overall shorter cell cycle (-2 h, Figure 5-7D).

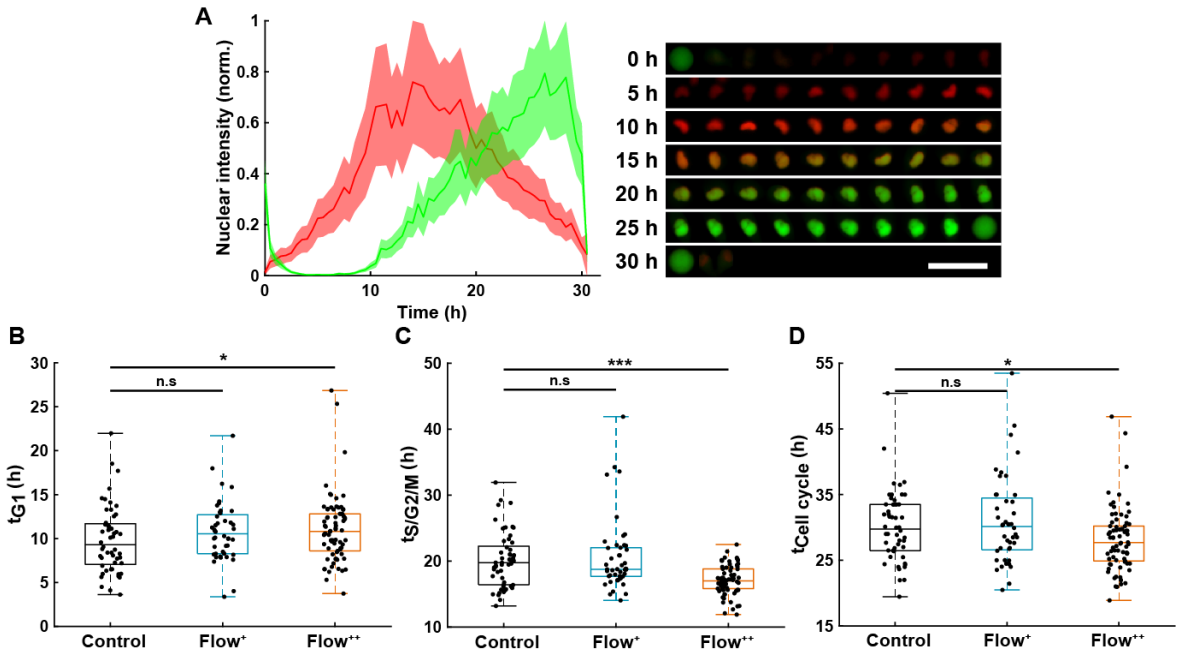

Figure 5-7 Increase in fluid flow leads to shorter S/G2/M phase, slightly longer G1 phase, and an overall shorter cell cycle.

(**A**) Normalized FUCCI2 fluorescence intensity inside of an exemplary segmented nucleus (left panel) with corresponding epifluorescence images over time (right panel). The line is the average, and the shaded area is the standard deviation. The time 0 h for each single cell corresponds to the first frame after division of the parent cell. Scale bar is 50 µm. (**B**) Duration of the G1 phase in the three groups (2 biological repeats and N = 52, 44 and 74 cells for the control, Flow^{+} and Flow^{++}, respectively). (**C**) Duration of the S/G2/M phase for the three experimental groups. (**D**) Duration of the whole cell cycle (time from division to division).

5.3.2 Fluid flow increases cell migration in a non-directional manner

To investigate whether the shortened cell cycle for the highest flow condition correlated with an impact of cell mobility, we examined single cell migration using the FUCCI2 marker. The center of the nucleus of every cell was tracked and their trajectories were recorded over time. The Figure 5-8A is a representation of an exemplary trap in phase contrast overlaid with cell trajectories coming from different traps and two biological repeats for the control and Flow^{++} groups. The dispersion and the migration of the cells within a trap was also represented with a heatmap of cell probability (Figure 5-8B). Every time a cell went to a certain position within a trap, the probability of its presence increased so that the resulting heatmap displayed the most likely position any cells would be found in. In both cases, the highest probability of presence was around the two posts. However, the highest flow condition (Flow^{++}) displayed a slightly shifted heatmap in the x direction, following the flow direction.

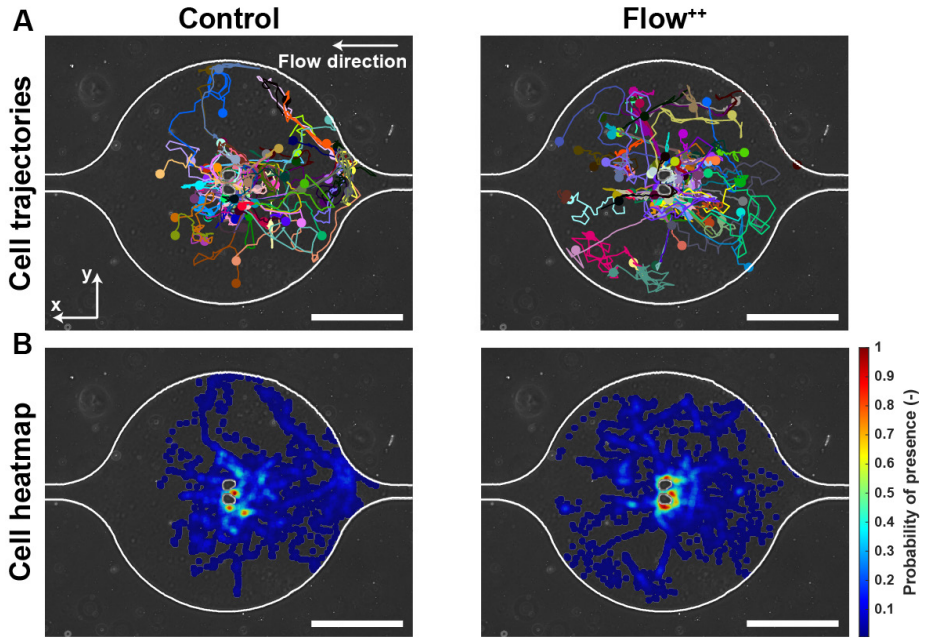

Figure 5-8 Single cell migration under flow: how metastatic cells explore the microfluidic device.
(**A)** Phase contrast image of an exemplary trap overlaid with cell trajectories coming from different traps and biological repeats for the control and Flow^{++} groups (2 biological repeats and N = 86 and 116 cells for the control and Flow^{++} groups). (**B**) Cell probability heatmap corresponding to the most frequently occupied location within the trap for the control and Flow^{++} groups. Scale bars are 200 µm.

In addition, migration related parameters were measured and analyzed for the three experimental groups (Figure 5-9).

The migration speed U (µm/min) was computed as the median of instantaneous migration speed of cells throughout their trajectory. The x component of the speed vector (Ux) was summed up throughout each cell trajectory to determine if the flow direction influenced the cell migration direction. Finally, the distance traveled was computed as the total distance a cell traveled over time and the displacement was defined as the distance between the beginning and the end of the tracking.

Like for the cell cycle dynamics, the $Flow^{+}$ experimental group did not show any significant difference with the control for all migration related parameters (Figure 5-9A, B, C, D and E). However, in the highest flow condition ($Flow^{++}$), migration speed increased up to 30 % (median) with respect to control (Figure 5-9A) in a non-directed fashion (Figure 5-9B), since the sum of Ux did not show any significant difference with the control. More specifically, the increase in migration speed was different in the G1 and the S/G2/M phase with the more significant increase recorded on the S/G2/M phase (Figure 5-9E). Interestingly, within each experimental condition, cells moved at similar migration speed in both G1 and S/G2/M phase with no significant difference (Figure 5-9E, red and green box). In addition, the total distance traveled by cells also increased by 24 % (from 347 µm to 432 µm) between the control and the $Flow^{++}$ group respectively (Figure 5-9C). Inversely, the displacement slightly decreased for the highest flow condition with respect to the control (Figure 5-9D). Not only did the highest flow condition fastened cell cycle dynamics but it also resulted in an acceleration of cell migration, irrespective of the flow direction.

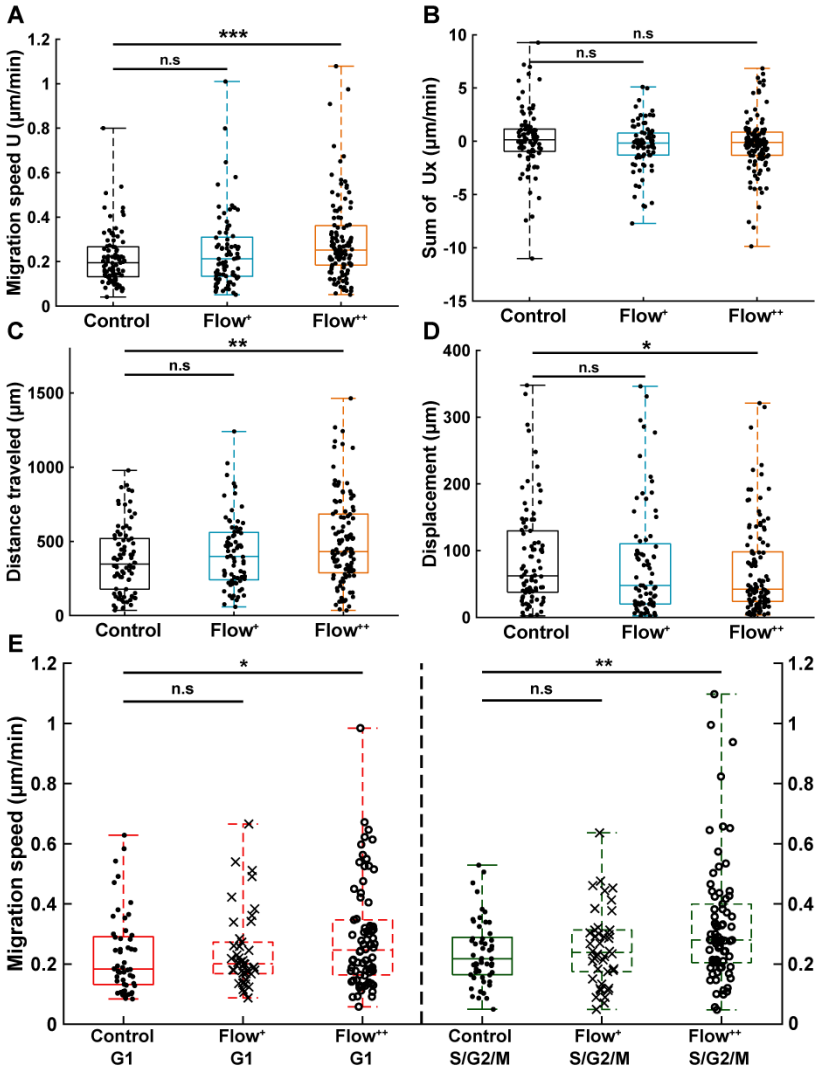

Figure 5-9 Higher fluid flow increases migration speed of metastatic cell.

(**A**) Migration speed magnitude (U, in µm/min) of single cells taken as the median of instantaneous cell speeds over their trajectories (2 biological repeats and N = 86, 76 and 116 cells for the control, Flow^{+} and Flow^{++} groups, respectively). (**B**) Sum of the x component of the velocity vectors (Ux, in µm/min) showing no preferred direction of movement with or against the flow. (**C**) Distance traveled (µm) between the beginning and the end of cell trajectories. (**D**) Displacement (µm) measured as the distance between the last and first position of cell trajectories (**E**) Migration speed magnitude separated by cell cycle phase (red boxplot for G1 phase and green for S/G2/M).

5.3.3 Cell main axis does not align with fluid streamlines before division

We quantified the orientation of the cells in the trap by measuring the angle between the cell main axis and the fluid streamlines (obtained with the CFD simulation) right before division occurred (Figure 5-10). An angle of 0 ° would represent the cell being parallel to the fluid streamlines and 90 ° would indicate the cell being perpendicular to the fluid streamlines (Figure 5-10A). Between the control and the Flow^{++}, there was no significant difference with respect to orientation before division (Figure 5-10C, boxplot). Furthermore, there was no specific relation in the angle between the cell main axis and the fluid velocity right before division for the control and Flow^{++} group (Figure 5-10C, colormap). The dispersion of angle covered the smallest (0.1 mm/s) to the highest (0.5 mm/s) velocity without any distinctive pattern.

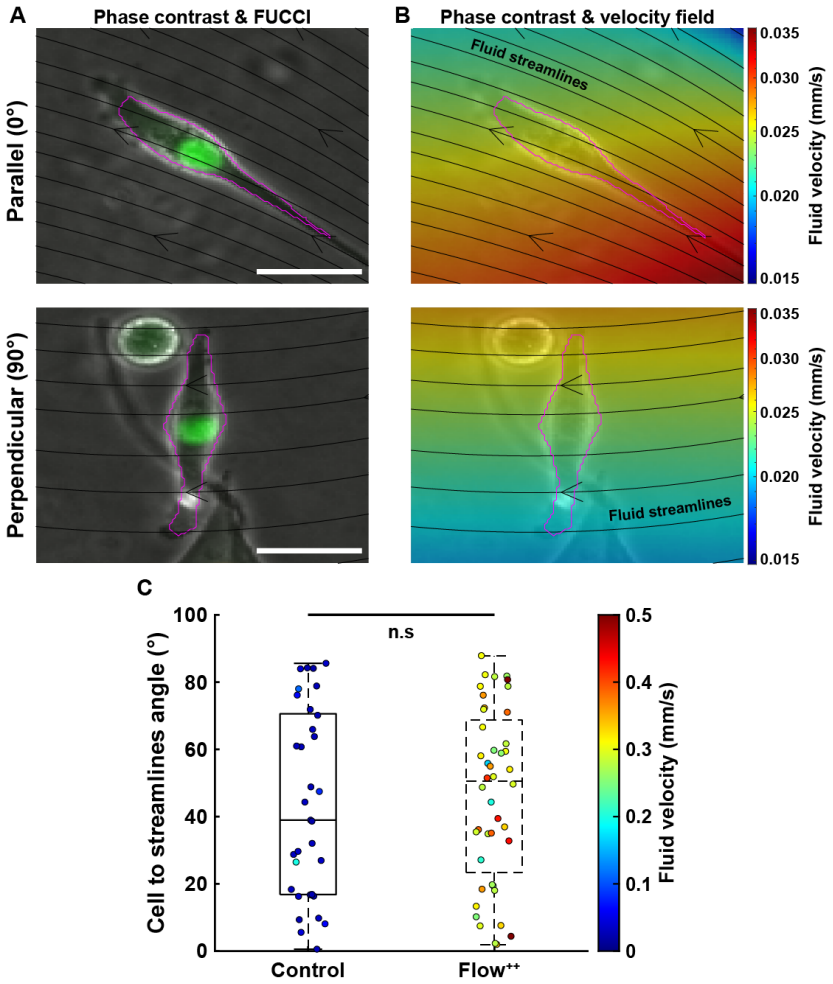

Figure 5-10 Metastatic cell main axis does not have a preferred orientation with respect to the fluid streamlines immediately before division.

(**A**) Overlay of phase contrast image and FUCCI2 fluorescence channel image before division for exemplary cells presenting its main axis parallel (low angle) to the

fluid streamlines (top panel) or perpendicular (high angle) to the streamlines (bottom panel). Scale bare are 50 µm. (**B**) Overlay of phase contrast image and simulated velocity field around the cell. (**C**) Angle between cell main axis and fluid streamlines (°) for the control and Flow^{++} groups (2 biological repeats, N = 33 and 44 cells, respectively). The markers are colored according to the fluid velocity around the cell.

5.3.4 Time-resolved volume analysis shows no impact on cell and nuclear volume under flow

We further investigated cell and nuclear volume changes under flow (Flow^{++}) with 3D confocal time-lapse imaging. After a mitosis event, daughter cells were tracked and segmented to obtain the cell and nuclear volume of every single cell throughout entire cell cycle (Figure 5-5). For every time point, the cells were segmented using deep learning in three channels: the SiR-Actin (magenta) was used to approximate the cell volume and mVenus/mCherry (green, yellow, red) were used to measure the nuclear volume as well as the cell cycle phases (Figure 5-11). Because we could isolate single cell inside a confined field of view suitable for confocal imaging, tracking single cell over a long period of time with 3D confocal microscopy was successful.

The cell volume roughly doubled linearly from onset of mitosis (t = 0h) to the next cell division event, in both the control and Flow^{++} groups (Figure 5-11B). In absolute value, the cell volume started at 3000 µm^3 and ended at 6000 µm^3 (Figure 5-11D) with a similar growth rate in both experimental conditions. More specifically during G1, cell volume increased from 3000 µm^3 to 4000 µm^3, and from 4000 µm^3 to 6000 µm^3.

Similarly, nuclear volume roughly doubled for every cell (Figure 5-11C), starting at 650 µm^3 and growing to 1200 µm^3 (Figure 5-11E), in both control and Flow^{++} groups. During G1, the volume increased from 650 µm^3 to 800 µm^3, until reaching 1200 µm^3 before division.

Overall, the absence of significant differences between the control and Flow^{++} group, despite the impact of flow previously reported (cell cycle dynamics and migration), suggested us to look for other parameters such as cell morphology.

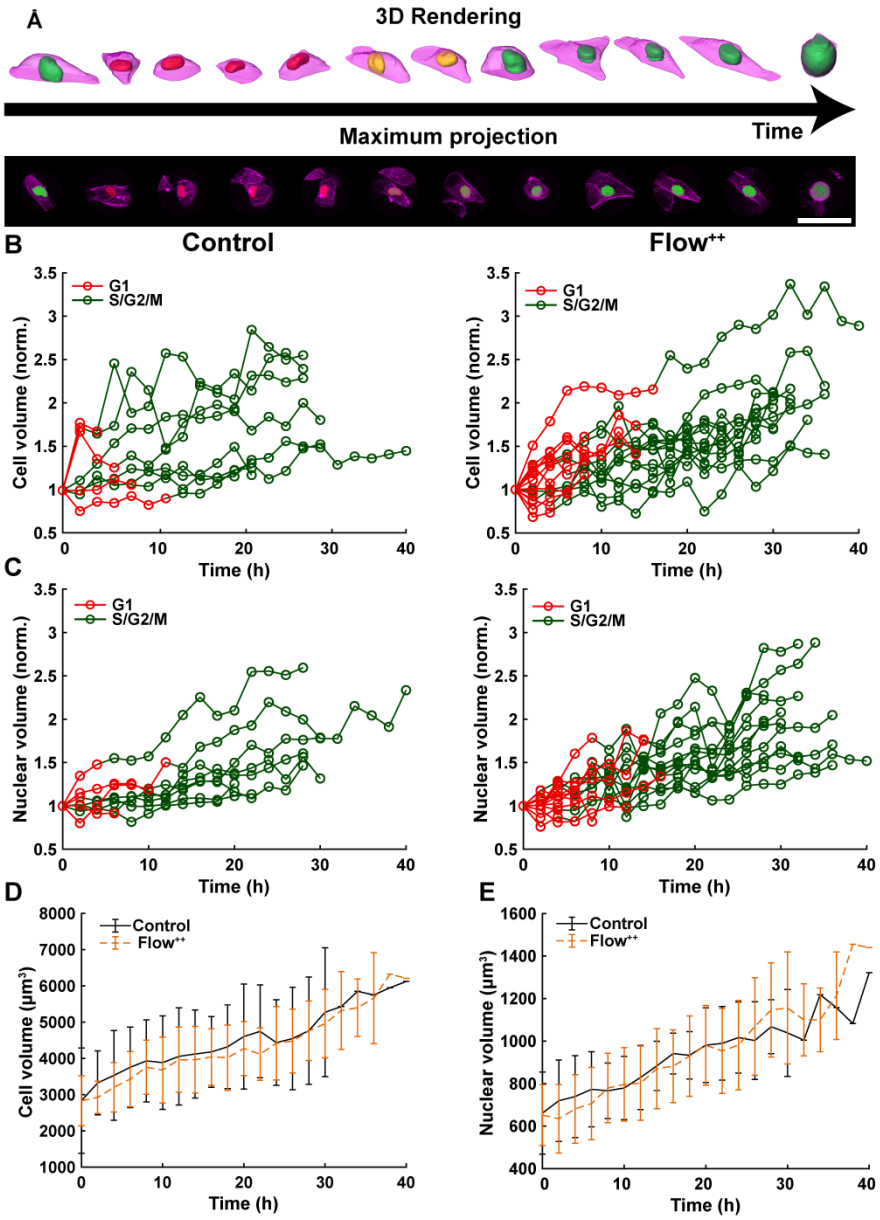

Figure 5-11 Time-resolved confocal 3D imaging of metastatic cells reveals no significant effect of fluid flow on cell and nuclear volume changes over time. (**A**) 3D rendering and maximum projection of one exemplary time lapse showing the evolution of the cell volume (magenta, SiR-Actin) with the nuclear volume (red, yellow and green for FUCCI2). Scale bar is 50 µm. (**B**) Time-resolved single cell volume during the cell cycle of every cell (normalized to the initial volume) for the control and Flow^{++} groups (two biological repeats and N = 8 and 15 cells). (**C**) Time-resolved nuclear volume during the cell cycle for every cell (normalized to the initial volume). (**D**) Cell volume (µm^3) over time averaged for all cells and the standard deviation. (**E**) Nuclear volume (µm^3) over time averaged for all cells and the standard deviation.

5.3.5 Shape analysis of 3D time lapse reveals no significant effects of fluid flow on cell elongation

Surprisingly the volume analysis did not show any significant difference between the control and the Flow^{++}. We then further investigated the cell and nuclear morphology coming from the same 3D confocal time lapse multi-channel images. Using MATLAB, we calculated the Eigenvalues of the voxels representing every segmented cell. We then defined the elongation (Eq. 1) as the ratio of the second Eigenvalue with respect to the first Eigenvalue (Figure 5-12), with 1 meaning a perfect spherical shape and 0 a really elongated cell.

$$Elongation = \frac{EV2}{EV1} \qquad 0 < Elongation < 1 \qquad \text{(Eq. 1)}$$

Firstly, within each experimental group and for every cell, we noticed a large fluctuation of cell elongation over time, as visible in Figure 5-12A, ranging from one to almost zeros. This indicated that the cell shape is not a constant variable during the cell cycle, regardless of the fluid flow experienced. Despite this variability, when averaging over the different cells, cell elongation seemed to follow a descending trend going from roughly isotropic at the beginning of the cell cycle (cell elongation ~ 0.6) to anisotropic and elongated towards the end (cell elongation reaching ~ 0.1) (Figure 5-12C) for both control and Flow^{++}. This trend can also be seen in Figure 5-5 with the actual cell and nuclear rendering. It is worth mentioning that the variance of cell elongation with the Flow^{++} group was larger than the control group.

Moreover, thanks to the FUCCI2 signal, the nuclear elongation could also be measured (Figure 5-12B). Within each experimental group, nuclear elongation over time displayed a smaller fluctuation than the cell elongation. Similarly, once again the nuclear elongation variance was broader in Flow^{++} than in the control group. Finally, the extrema values ranged from 1 to 0.3 for the control to 0.9 to 0.2 for the Flow^{++} group Figure 5-12D. In contrast to the cell elongation, the nuclear elongation followed a constant trend, with an average value reaching ~ 0.5.

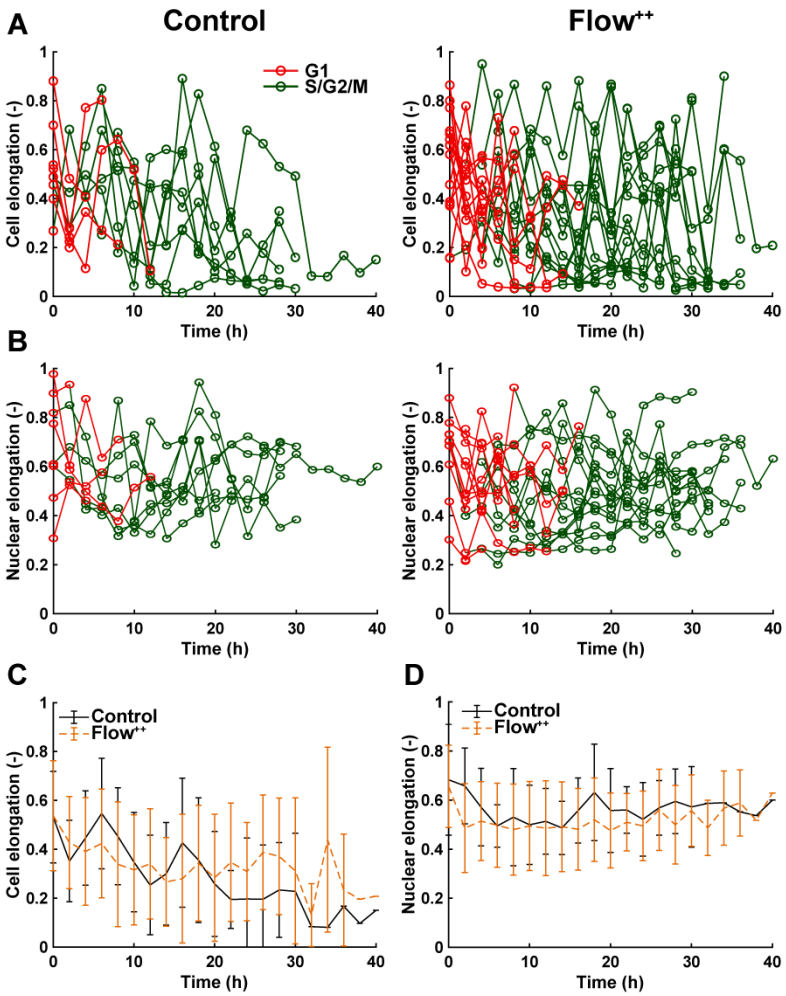

Figure 5-12 Time-resolved confocal 3D imaging of metastatic cells reveals variation of cell and nuclear elongation throughout the cell cycle.

(**A**) Time-resolved single cell elongation during the cell cycle of every cell for the control and Flow^{++} groups (two biological repeats and N = 8 and 15 cells). (**B**) Time-resolved nuclear elongation during the cell cycle of every cell for the control and Flow^{++} groups. (**C**) Cell elongation and (**D**) nuclear elongation over time averaged between all cells with the standard deviation.

The FUCCI2 signal provided additional information since we could distinguish the cell and nuclear elongation at every phase of the cell cycle (Figure 5-13). For this, we poled all data points as a function of the cell cycle phase. It means that every datapoint in the boxplot corresponds to one cell for one time point in its respective cell cycle phase (G1, S/G2/M). Firstly, we could find similar results as previously, meaning that between the G1 and the S/G2/M phase (red vs. green boxplots), the cell elongation significantly decreased for both the control (plain lines) and the Flow^{++} (dashed lines) groups

(Figure 5-13A). Between the control and the Flow^{++}, we could not see a significant difference with respect to the cell elongation, neither in G1 nor S/G2/M phase. Additionally, the nuclear elongation was similar between the control and the Flow^{++} in G1 and did not show significant differences (Figure 5-13B, red boxplots). However, in S/G2/M the nuclear elongation strongly decreased for the Flow^{++} group (Figure 5-13B, green boxplots).

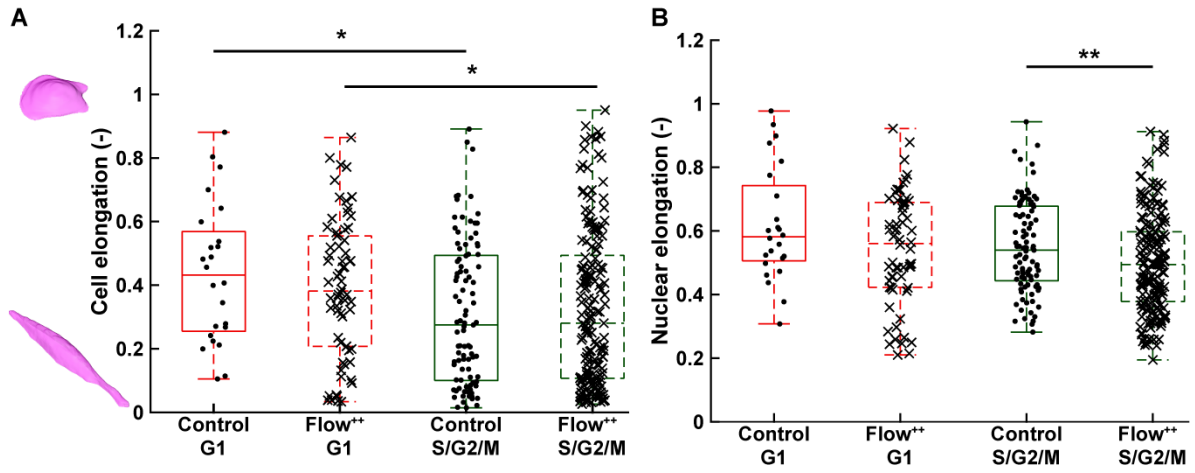

Figure 5-13 Confocal 3D imaging of metastatic cells reveals no significant effect of fluid flow on cell elongation and a decrease in nuclear elongation.
(**A**) Cell elongation during the G1 phase (red), S/G2/M phase (green) for the control and Flow^{++} groups (2 biological repeats and N = 24, 66, 97, 177, 121 and 243 timepoints, respectively). (**B**) Nuclear elongation during the G1 phase (red), S/G2/M phase (green) for the control and Flow^{++} groups (2 biological repeats and N = 24, 62, 97, 177, 121 and 239 timepoints, respectively).

5.3.6 Coupling 3D time lapse and CFD for shear stress analysis

The wall shear stress was computed using OpenFOAM on a computer cluster and the SiR-Actin channel was used to approximate the cell membrane. A simulation was performed for each z-stack acquired by confocal microscopy, for each timepoint of the cell cycle (Figure 5-14A). The simulations were parametrized and interfaced with OpenFOAM automatically using a custom-made script written in Python 3.8.6 (ASOC). The cells in the trap were 3D-modelled and meshed like previously described in section 5.2.9. The wall shear stress value was obtained by averaging every element of the mesh representing the cell (Figure 5-14B). By 3D time lapse confocal imaging and

simulations, we could calculate in a more accurate way the mechanical stress that cells experience under fluid flow. For this exemplary cell taken from the Flow^{++} group, the wall shear stress experienced was in average 6 ± 4 mPa or 0.06 ± 0.04 dyne/cm² and constant throughout the cell cycle.

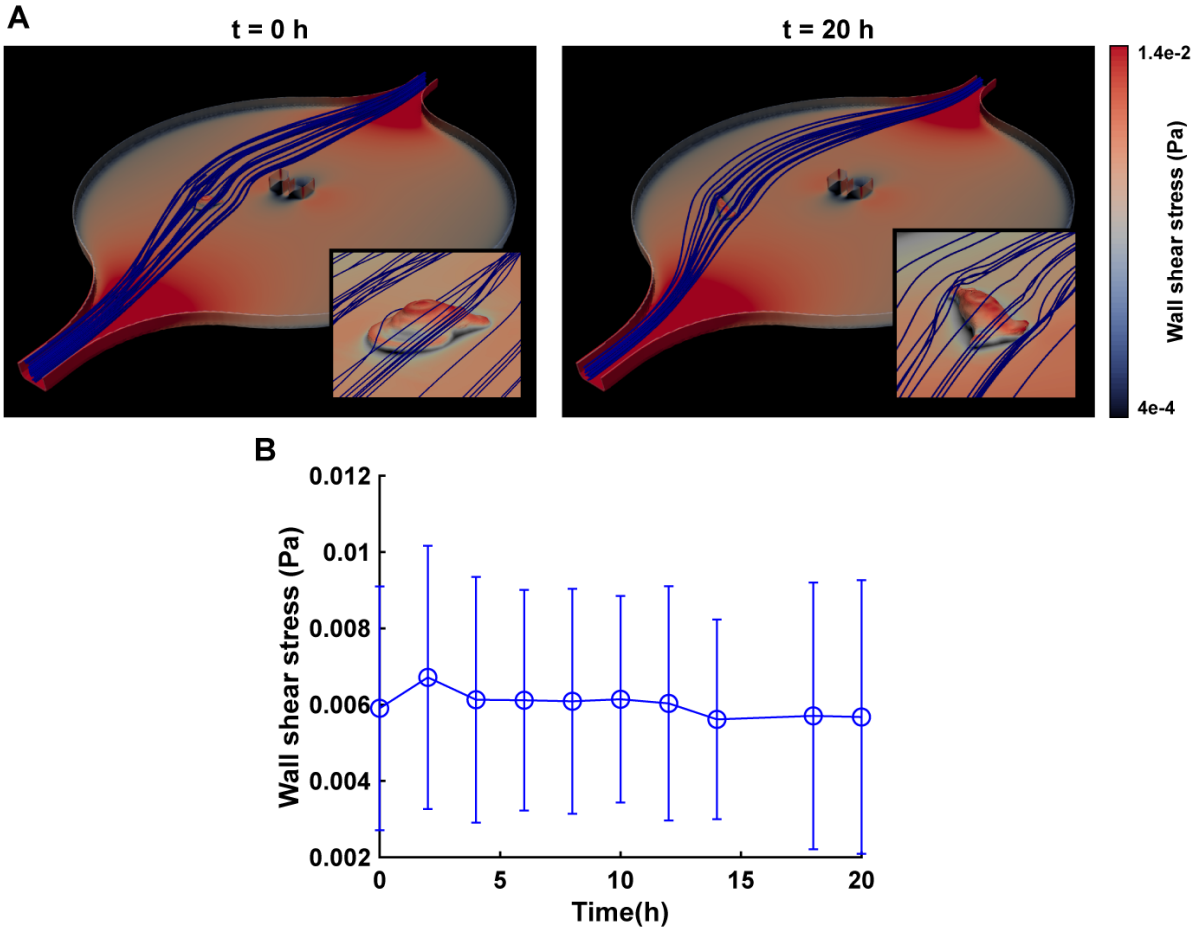

Figure 5-14 Time lapse wall shear stress calculation using CFD and 3D confocal imaging.

(**A**) Finite element simulation of an exemplary real cell shape (obtained with SiR-Actin) inside a trap for the Flow^{++} group (streamlines around the cell indicated in blue). (**B**) Wall shear stress over its surface that one exemplary MDA-FUCCI2 cell experienced during its cell cycle. Line is the average over the cell surface, and the error bars correspond to the standard deviation.

5.4 Discussion

Fluid flow and resulting shear stress is a physiologically important cue that is involved in several processes in cancer metastasis [39]. It is known that regions of high shear

stress can be detrimental to cancer cells by promoting cell death [145]. Here, our findings on 2D single cell analysis identify fluid flow mimicking sinusoid capillaries as a biophysical cue that can slightly modulate single cell cycle dynamics by reducing the S/G2/M phase duration, hence the overall division time and thus increasing the proliferation behavior of metastatic cancer cells.

3D time lapse single cell analysis showed no significant differences between the evolution of the cell and nuclear volume under flow. Moreover, a more elongated nuclear shape was observed during S/G2/M phase under $Flow^{++}$.

Most methods for cell or nuclear segmentation involve compromise between automation and flexibility. It can be done completely with manual labeling [146], with customized pipelines involving user-specific parameters [147, 149] or with fully automated methods based on deep learning networks containing parameters estimated on large training datasets [150, 151]. We propose here an approach based on the deep learning network U-net for 3D time lapse cell and nucleus segmentation with minimal training datasets. By doing so, we significantly decreased the processing time of our large datasets. Still, our method was trained on a specialized dataset, and it will be interesting to see how it can generalize to other cell lines for example. A large international competition (Data Science Bowl) was held recently to gather dataset of varied images of nuclei from many different laboratories and a deep learning method outperformed other methods on segmentation tasks [152]. Very recently, a similar approach was taken to gather images of cells from many laboratories and create a universal deep learning model to perform cell segmentation without requiring parameter adjustments, new training data or network retraining [153].

Our CFD simulation inside the trap shows that the velocities correspond to what was measured *in vivo* in the bone marrow sinusoidal capillaries [137]. Interestingly, at these velocities, we show that the time spent in S/G2/M phase was significantly reduced with respect to the control, thus accelerating the overall cell cycle. This is in agreement with previous work done in prostate cancer cells that demonstrated an acceleration of proliferation under similar range of WSS (0.05 dyne/cm²) [154]. In their work, they identified that under flow, the transcriptional coactivator with PDZ-binding motif (TAZ) positively influenced cancer cell proliferation, whereas silencing of TAZ under flow reduced proliferation with respect to control. Indeed, TAZ can act as a promotor and amplify genes that have roles in cell proliferation and other cellular functions [155, 156] and its activation under fluid flow could explain the observed acceleration in the cell

cycle. Nonetheless, it has been proven that much higher fluid flow and shear stress (~ 12 dynes/cm²), which are values found *in vivo* in intermediate capillaries [137], could induce a cell cycle arrest via G2/M in DTCs by increasing the expression of cyclin B1 and p21, while decreasing the expressions of cyclin A, D1 and E, CDK-1, -2, -4 and -6, as well as p27, in three bone cancer cell lines and one tongue cancer cell line [157]. This result also can be put in perspective with the emergence of quiescent HSC preferentially found in small arterioles in the BM [37], regions where shear stress is higher than sinusoidal capillaries (>20 dyne/cm²) [137]. Unfortunately, our system in its current state does not allow to reach such high shear stress and would require design modifications. It is also worth noting that shear stress may not only be the sole factor inducing quiescence, as arterioles are also different in structure from sinusoids since they are located around sympathetic nerves, smooth muscle cells as well as matrix components, and their function is to bring blood from the heart under high pressure [37]. While accelerated proliferation under sinusoidal flow was previously reported [157], to the best of our knowledge it is the first time that quantification of cell cycle phase duration in real time is being reported, thanks to the FUCCI system.

We hypothesized that a reason for cell cycle dynamics to accelerate could be that the fluid streamlines physically supports cells to divide. Indeed, if cells oriented themselves perpendicular to the flow, it could bring support for the division hence resulting in faster cell cycle dynamics. Our results however do not support this hypothesis since there was no significant difference observed between the cell orientation with respect to the flow in the control and the Flow^{++} group right before division. It would nonetheless be interesting to quantify the orientation with respect to the flow during the total cell cycle, but more work would be required.

Acting not only as a cell cycle reporter, the FUCCI system can also be used to track single cell migration thanks to our FUCCItrack software. We show that irrespective of the flow condition, MDA-FUCCI2 generally had similar migration speed in G1 and in S/G2/M phase, matching previous work with HeLa FUCCI cells [53]. Moreover, under Flow^{++} the migration speed and distance traveled increased significantly compared to control despite not exhibiting any preferred direction with respect to the direction of the flow. A previous study, also done in a microfluidic device with MDA-MB-231 breast cancer cell, also confirms an increase of migration speed as well as a more migratory behavior under flow [158]. More specifically, they identify the transient receptor potential melastatin 7 (TRPM7) as being activated by fluid-shear through deformation

of the plasma membrane and promoting extracellular calcium influx which in turn activate several pathways coordinating cell migration. Indeed, it has been shown that biophysical cues such as shear stress can activate mechanosensitive ion channels to enable uptake of extracellular Ca^{2+} into the cell [159].

It is still not clear what mechanisms are responsible for our results concerning the cell cycle dynamics and migration, but we attempted to understand it from a morphological point of view with 3D time lapse imaging.

Based on those data we could not detect any significant differences in cell volume and cell shape changes over time, between $Flow^{++}$ and the control group. Interestingly, we could detect a more elongated nuclear shape during the S/G2/M phase under $Flow^{++}$.

Finally, our approach to compute the wall shear stress to potentially gain more insights on how cells feel shear stress was novel but could not be sufficiently developed to make it usable in this thesis would require further investigations to complete it.

5.5 Limitations

The current chapter shows the role of fluid flow mimicking sinusoidal capillaries region and its impact on breast cancer cell dormancy *in vitro*. Thanks to the single cell trap from the microfluidic device, we could perform 3D time lapse multi-channel imaging and extract critical information about the evolution of cell and nuclear volume, and cell and nuclear shape under flow. Because of technical limitations on the system (volume of syringe and long time lapse required), we could not go above 0.2 µL/min for the flow rate. We saw that from 0.1 µL/min ($Flow^{+}$) to 0.2 µL/min ($Flow^{++}$), a clear change of behavior occurred within the cell cycle duration and migration, and it would have been interesting to go beyond these values to see if the trend further evolved in that direction.

Furthermore, and similar to Chapter 4, the use of a single cell line is a hard limitation and lowers the impact of our message. Due to time constraints, MCF7-FUCCI2 cell line could not be included in the study.

The overall experimental design in this chapter was complex both from the experimental point of view, as it required a lot of hardware for long 2D and 3D time-lapse imaging experiments, as well as from the analysis point of view, with large data sets being generated. We used an epifluorescence microscope as well as a confocal microscope for up to 4 days of time-lapse. For the confocal microscope, we used a 63x water immersion objective with a water dispenser to have constant and continuous

water at the interface between the objective and the plate. In addition, we also needed the whole wafer and microfluidic preparation hardware.

It is also worth noting the staggering amount of work to process the resulting 3D time lapse multi channels data, even though with FUCCItrack and the deep learning approached, we could eventually streamline the process.

Chapter 6 Conclusion & future directions

6.1 Conclusion

In this thesis, we investigated the role of various biophysical cues in controlling breast cancer cell dormancy and reactivation. Specifically, we investigated the effect of osmotic pressure and fluid flow on cell and nuclear morphology, migration and cell cycle dynamics. To do so, we used microfluidic systems and performed quantitative real-time live imaging of single cancer cells genetically modified with the FUCCI2 system, where the cell cycle G1 phase was visualized with red fluorescence and the S/G2/M phase with green fluorescence.

To perform the quantitative analyses of complex time lapse experiments running for up to 4 days, we developed a fully automated software FUCCItrack with a graphical user interface written in MATLAB (with additional option for manual corrections) to facilitate the analysis of big datasets for the FUCCI or more generally the cell cycle reporter community. We believe it will provide a solid ground for researchers wanting to use this amazing tool that represents the FUCCI system, thus extending its usage to researchers with small or no experience in image processing. We made FUCCItrack completely open-source and modular so that anyone can build on this in the future.

Thanks to FUCCItrack, we showed that under hyperosmotic stress, distinct cell subpopulations emerge with impaired nuclear growth, delayed or growth-arrested cell cycle and reduced cell migration. This effect is reversible for mild hyperosmotic pressure and cells can return to regular cell cycle dynamics, proliferation and migration upon release of the osmotic pressure. These findings emphasize the importance of considering the local osmotic pressure in the microenvironment potentially harboring dormant cells.

The last part of this thesis focused on the effect of fluid flow and shear stress mimicking regions in the sinusoidal capillaries in the bone marrow. We used a microfluidic device that we integrated with both 2D epifluorescence and 3D confocal microscopy, within an incubator for live cell imaging over 4 days. Single cell data in 2D revealed that under higher fluid flow, cell cycle dynamics was shortened, the migratory activity increased

significantly, yet the directionality was not influenced by the flow direction. With 3D confocal time lapse multi-channel imaging, we showed that at the single cell level, no significant difference could be measured in terms of cell or nuclear volume, when compared to the control experimental group. In terms of morphology, only the nuclear shape showed a more elongated profile under higher fluid flow, whereas the cell elongation did not differ significantly between groups. The apparent shortening of the cell cycle and increased migratory activity, accompanied with the absence of striking differences in cell and nuclear volume/shape discard our initial hypothesis: if fluid flow originating from the sinusoidal capillaries alone can provide a sufficient trigger to generate a dormant phenotype. Nevertheless, this chapter provides novel insights based on 3D time lapse single cell imaging and deep learning image analysis, inviting follow up experiments exploring higher fluid flow velocities or other biophysical cues such as osmotic pressure or hypoxia.

As a proof of principle, we developed an automated simulation model to compute the velocity of the fluid within the microfluidic chip and the resulting cell wall shear stress over time, based on the experimental input from the 3D confocal time lapse images under flow. This coupling of experimental time-resolved microscopy 3D data and fluid flow simulations corresponds to a new approach in CFD simulation and could provide exciting novel insights linking single cell volume, nuclear volume and cell cycle dynamics as a function of the fluid flow and shear stress.

6.2 Future directions

The **first goal** in this thesis was to provide an open-source software with a graphical user interface to broaden the outreach of the FUCCI system, and in general of live cell cycle reporters. With FUCCItrack, we hope that the difficulties associated with large datasets such as time lapse imaging and the resulting processing time could be reduced. Because we created FUCCItrack to be modular, it is a perfect candidate to receive improvement, updates and new modules over the years. Since it is open-source and available online on a GitHub, this can be done easily by myself, or any other researchers. One potential first direction of improvement would be to make FUCCItrack usable for people with a single classical live staining. This will make the cell cycle dynamics analysis module less relevant, but researchers could still use the software and the graphical user interface for migration analysis.

As we also mentioned previously, an additional module was created for the preparation of the deep learning part currently done in DragonFly. It would be beneficial in the future to migrate the deep learning training and testing directly within MATLAB to reduce the number of software dependencies.
Finally, another module could be added to directly link the 3D time lapse imaging workflow and surface generation with the scripts developed in python to automatically launch the simulation (ASOC). Additionally, ASOC could also be translated into MATLAB to reduce once more the number of software dependencies.

The **second goal** was to use FUCCItrack to discover how metastatic breast cancer cells react under osmotic pressure and fluid flow mimicking region of sinusoidal capillaries. For the osmotic pressure part, it would be highly beneficial to further continue the investigation of single cell behavior of other FUCCI2 cell lines. We indeed proved that proliferation was decreased under osmotic stress for MCF7-FUCCI2 cells but at a collective level. More in depth single cell analysis of this weaker metastatic breast cancer cell line would be beneficial to the understand of the role of osmotic stress as a cue in breast metastasis and dormancy. Specifically, if sub populations of highly delayed or completely growth arrested emerge under osmotic stress. Going further, we also could use the non-malignant cell line such as MCF10A-FUCCI2 that we already possess to evaluate the specificity of the osmotic role to cancer cells.
Moreover, more investigation into the mechanism behind the reversible growth arrest we observed is needed. A first interesting result that we could observe was the lack of nuclear growth in 2D under osmotic stress for growth arrested MDA-FUCCI2. However, with the current microfluidic platform and the 3D time lapse imaging workflow that we developed, we could now increase the dimensionality and investigate further into how cell and nuclear volume as well as shape are impacted by osmotic stress.

For the fluid flow part, one could hypothesize that we did not reach high enough values of shear stress to trigger a dormant phenotype. Unfortunately, with the current design we were limited to certain values of shear stress, but it would be possible to adapt the design to offer a broader range of fluid flow values and test this hypothesis. It is worth noting that already under Flow^{++} conditions, we sometimes observed cells detachment upon division and thus lost the tracking of these cells. If we increase of fluid flow, further

work will be needed to potentially coat the glass of the microfluidic device, ensuring a tighter adhesion force of the cells with the substrate.
It will also be beneficial to perform immunofluorescence inside the microfluidic device to further understand the acceleration of the cell cycle as well as the increased migration behavior. With this, one could also precisely quantify the shape of the cells under flow by taking higher resolution images, even if it corresponds to an end point of the experiment. A more detailed analysis of for example filopodia number and length could thus be performed.

Our **third goal** was to develop an approach to use a microfluidic device along with computational fluid dynamics to study the interaction of breast cancer cells with fluid flow. Unfortunately, because of lack of time, the connection between the real 3D cell shapes over time and the shear stress in the simulation could not be done automatically, even though all the workflow was ready for this. Indeed, we faced severe issues of non-convergence during the simulation because of the inherent shape irregularities of cells and manual correction on the mesh was necessary to obtain convergence. More work would be needed to have a running workflow and provide the wall shear stress experienced by the cells.

More generally, the technical and image processing workflow that we developed during this thesis could be used to investigate in depth other biophysical cues that are related to cancer metastasis and dormancy. For example, hypoxia conditions can be easily created thanks to a gas mixer that can be connected to our existing top stage incubator or pH can also be controlled with the concentration of CO_2 in the air.

We believe that with some optimization, our system can be extended to other researchers to tackle many questions about the interplay between biophysical cues and breast cancer cell metastasis and dormancy.

Bibliography

[1] Steeg, P. S. Targeting metastasis. *Nat. Rev. Cancer* **16**, 201–218 (2016) . https://doi.org/10.1038/nrc.2016.25.

[2] Steeg, P. S. Tumor metastasis: mechanistic insights and clinical challenges. *Nat. Med.* **12**, 895–904 (2006) . https://doi.org/10.1038/nm1469.

[3] Lawson, D. A., Kessenbrock, K., Davis, R. T., Pervolarakis, N. & Werb, Z. Tumour heterogeneity and metastasis at single-cell resolution. *Nat. Cell Biol.* **20**, 1349–1360 (2018) . https://doi.org/10.1038/s41556-018-0236-7.

[4] EBCTCG: Early Breast Cancer Trialists' Collaborative Group. Effects of chemotherapy and hormonal therapy for early breast cancer on recurrence and 15-year survival: an overview of the randomised trials. *Lancet* **365**, 1687–1717 (2005) . https://doi.org/10.1016/S0140-6736(05)66544-0.

[5] Coleman, R. E. Clinical Features of Metastatic Bone Disease and Risk of Skeletal Morbidity. *Clin. Cancer Res.* **12**, 6243s-6249s (2006) . https://doi.org/10.1158/1078-0432.CCR-06-0931.

[6] Weilbaecher, K. N., Guise, T. A. & McCauley, L. K. Cancer to bone: a fatal attraction. *Nat. Rev. Cancer* **11**, 411–425 (2011) . https://doi.org/10.1038/nrc3055.

[7] Karrison, T. G., Ferguson, D. J. & Meier, P. Dormancy of Mammary Carcinoma After Mastectomy. *JNCI J. Natl. Cancer Inst.* **91**, 80–85 (1999) . https://doi.org/10.1093/jnci/91.1.80.

[8] Giancotti, F. G. Mechanisms Governing Metastatic Dormancy and Reactivation. *Cell* **155**, 750–764 (2013) . https://doi.org/10.1016/j.cell.2013.10.029.

[9] Linde, N., Fluegen, G. & Aguirre-Ghiso, J. A. The Relationship Between Dormant Cancer Cells and Their Microenvironment. in *Advances in Cancer Research* vol. 132 45–71 (Elsevier Inc., 2016). . https://doi.org/10.1016/bs.acr.2016.07.002.

[10] Sosa, M. S., Bragado, P. & Aguirre-Ghiso, J. A. Mechanisms of disseminated cancer cell dormancy: an awakening field. *Nat. Rev. Cancer* **14**, 611–622 (2014) . https://doi.org/10.1038/nrc3793.

[11] Aguirre-Ghiso, J. A. Models, mechanisms and clinical evidence for cancer dormancy. *Nat. Rev. Cancer* **7**, 834–846 (2007) . https://doi.org/10.1038/nrc2256.

[12] Chambers, A. F., Groom, A. C. & MacDonald, I. C. Dissemination and growth of cancer cells in metastatic sites. *Nat. Rev. Cancer* **2**, 563–572 (2002) . https://doi.org/10.1038/nrc865.

[13] Ghajar, C. M. *et al.* The perivascular niche regulates breast tumour dormancy. *Nat. Cell Biol.* **15**, 807–817 (2013) . http://dx.doi.org/10.1038/ncb2767.

[14] Naumov, G. N. *et al.* Ineffectiveness of Doxorubicin Treatment on Solitary Dormant Mammary Carcinoma Cells or Late-developing Metastases. *Breast Cancer Res. Treat.* **82**, 199–206 (2003) . https://doi.org/10.1023/B:BREA.0000004377.12288.3c.

[15] Marshall, J.-C. A. *et al.* Effect of Inhibition of the Lysophosphatidic Acid Receptor 1 on Metastasis and Metastatic Dormancy in Breast Cancer. *JNCI J. Natl. Cancer Inst.* **104**, 1306–1319 (2012) . https://doi.org/10.1093/jnci/djs319.
[16] Goss, P. E. & Chambers, A. F. Does tumour dormancy offer a therapeutic target? *Nat. Rev. Cancer* **10**, 871–877 (2010) . https://doi.org/10.1038/nrc2933.
[17] Paget, S. The distribution of secondary growths in cancer of the breast. *Lancet* **133**, 571–573 (1889) . https://doi.org/10.1016/S0140-6736(00)49915-0.
[18] Levental, K. R. *et al.* Matrix Crosslinking Forces Tumor Progression by Enhancing Integrin Signaling. *Cell* **139**, 891–906 (2009) . http://dx.doi.org/10.1016/j.cell.2009.10.027.
[19] Nakasone, E. S. *et al.* Imaging Tumor-Stroma Interactions during Chemotherapy Reveals Contributions of the Microenvironment to Resistance. *Cancer Cell* **21**, 488–503 (2012) . https://doi.org/10.1016/j.ccr.2012.02.017.
[20] Provenzano, P. P., Inman, D. R., Eliceiri, K. W. & Keely, P. J. Matrix density-induced mechanoregulation of breast cell phenotype, signaling and gene expression through a FAK–ERK linkage. *Oncogene* **28**, 4326–4343 (2009) . https://doi.org/10.1038/onc.2009.299.
[21] Bragado, P. *et al.* TGF-β2 dictates disseminated tumour cell fate in target organs through TGF-β-RIII and p38α/β signalling. *Nat. Cell Biol.* **15**, 1351–1361 (2013) . https://doi.org/10.1038/ncb2861.
[22] Liu, Y. *et al.* Blockade of IDO-kynurenine-AhR metabolic circuitry abrogates IFN-γ-induced immunologic dormancy of tumor-repopulating cells. *Nat. Commun.* **8**, 15207 (2017) . https://doi.org/10.1038/ncomms15207.
[23] Gao, H. *et al.* The BMP Inhibitor Coco Reactivates Breast Cancer Cells at Lung Metastatic Sites. *Cell* **150**, 764–779 (2012) . https://doi.org/10.1016/j.cell.2012.06.035.
[24] Di Martino, J. S. *et al.* A tumor-derived type III collagen-rich ECM niche regulates tumor cell dormancy. *Nat. Cancer 2021* 1–18 (2021) . https://doi.org/10.1038/s43018-021-00291-9.
[25] Fluegen, G. *et al.* Phenotypic heterogeneity of disseminated tumour cells is preset by primary tumour hypoxic microenvironments. *Nat. Cell Biol.* **19**, 120–132 (2017) . https://doi.org/10.1038/ncb3465.
[26] Schwartz, L., da Veiga Moreira, J. & Jolicoeur, M. Physical forces modulate cell differentiation and proliferation processes. *J. Cell. Mol. Med.* **22**, 738–745 (2017) . https://doi.org/10.1111/jcmm.13417.
[27] Agus, D. B. *et al.* A physical sciences network characterization of non-tumorigenic and metastatic cells. *Sci. Rep.* **3**, 1449 (2013) . https://doi.org/10.1038/srep01449.
[28] DelNero, P., Hopkins, B. D., Cantley, L. C. & Fischbach, C. Cancer metabolism gets physical. *Sci. Transl. Med.* **10**, eaaq1011 (2018) . https://doi.org/10.1126/scitranslmed.aaq1011.
[29] Delarue, M. *et al.* Compressive Stress Inhibits Proliferation in Tumor Spheroids through a Volume Limitation. *Biophys. J.* **107**, 1821–1828 (2014) . https://doi.org/10.1016/j.bpj.2014.08.031.
[30] Nam, S. & Chaudhuri, O. Mitotic cells generate protrusive extracellular forces to divide in three-dimensional microenvironments. *Nat. Phys.* **14**, 621–628 (2018) . https://doi.org/10.1038/s41567-018-0092-1.
[31] Nam, S. *et al.* Cell cycle progression in confining microenvironments is regulated by a growth-responsive TRPV4-PI3K/Akt-p27 Kip1 signaling axis. *Sci. Adv.* **5**, eaaw6171 (2019) . https://doi.org/10.1126/sciadv.aaw6171.

[32] Sun, Y., Chen, C. S. & Fu, J. Forcing Stem Cells to Behave: A Biophysical Perspective of the Cellular Microenvironment. *Annu. Rev. Biophys.* **41**, 519–542 (2012) . https://doi.org/10.1146/annurev-biophys-042910-155306.

[33] Lv, R. *et al.* Detection and Quantification of Viable but Non-culturable Campylobacter jejuni. *Front. Microbiol.* **10**, (2020) . https://doi.org/10.3389/fmicb.2019.02920.

[34] Abuhattum, S. *et al.* Intracellular Mass Density Increase Is Accompanying but Not Sufficient for Stiffening and Growth Arrest of Yeast Cells. *Front. Phys.* **6**, (2018) . https://doi.org/10.3389/fphy.2018.00131.

[35] Vicente, M. J. *et al.* Effect of light, temperature, and salinity and drought stresses on seed germination of Hypericum ericoides, a wild plant with ornamental potential. *Sci. Hortic. (Amsterdam).* **270**, 109433 (2020) . https://doi.org/10.1016/j.scienta.2020.109433.

[36] Undeen, A. h. & Frixione, E. The Role of Osmotic Pressure in the Germination of Nosema algerae Spores 1. *J. Protozool.* **37**, 561–567 (1990) . https://doi.org/10.1111/j.1550-7408.1990.tb01265.x.

[37] Kunisaki, Y. *et al.* Arteriolar niches maintain haematopoietic stem cell quiescence. *Nature* **502**, 637–643 (2013) . https://doi.org/10.1038/nature12612.

[38] Acar, M. *et al.* Deep imaging of bone marrow shows non-dividing stem cells are mainly perisinusoidal. *Nature* **526**, 126–130 (2015) . https://doi.org/10.1038/nature15250.

[39] Follain, G. *et al.* Fluids and their mechanics in tumour transit: shaping metastasis. *Nat. Rev. Cancer* **20**, 107–124 (2020) . https://doi.org/10.1038/s41568-019-0221-x.

[40] Gerdes, J. Ki-67 and other proliferation markers useful for immunohistological diagnostic and prognostic evaluations in human malignancies. *Semin. Cancer Biol.* **1**, 199–206 (1990). https://pubmed.ncbi.nlm.nih.gov/2103495/.

[41] Yamamoto, N. *et al.* Cellular Dynamics Visualized in Live Cells in Vitro and in Vivo by Differential Dual-Color Nuclear-Cytoplasmic Fluorescent-Protein Expression. *Cancer Res.* **64**, 4251–4256 (2004) . https://doi.org/10.1158/0008-5472.CAN-04-0643.

[42] Catala, M., Lamontagne, B., Larose, S., Ghazal, G. & Elela, S. A. Cell Cycle-dependent Nuclear Localization of Yeast RNase III Is Required for Efficient Cell Division. *Mol. Biol. Cell* **15**, 3015–3030 (2004) . https://doi.org/10.1091/mbc.e04-03-0183.

[43] Jiang, P. *et al.* Tumor Cells Genetically Labeled with GFP in the Nucleus and RFP in the Cytoplasm for Imaging Cellular Dynamics. *Cell Cycle* **5**, 1198–1201 (2006) . https://doi.org/10.4161/cc.5.11.2795.

[44] Ersoy, I., Bunyak, F., Chagin, V., Cardoso, M. C. & Palaniappan, K. Segmentation and Classification of Cell Cycle Phases in Fluorescence Imaging. in *Lecture Notes in Computer Science* vol. 5762 LNCS 617–624 (Springer, Berlin, Heidelberg, 2009). . https://doi.org/10.1007/978-3-642-04271-3_75.

[45] Gavet, O. & Pines, J. Progressive Activation of CyclinB1-Cdk1 Coordinates Entry to Mitosis. *Dev. Cell* **18**, 533–543 (2010) . https://doi.org/10.1016/j.devcel.2010.02.013.

[46] Batters, C., Zhu, H. & Sale, J. E. Visualisation of PCNA Monoubiquitination In Vivo by Single Pass Spectral Imaging FRET Microscopy. *PLoS One* **5**, e9008 (2010) . https://dx.plos.org/10.1371/journal.pone.0009008.

[47] Kitamura, A., Nakayama, Y. & Kinjo, M. Efficient and dynamic nuclear localization of green fluorescent protein via RNA binding. *Biochem. Biophys. Res. Commun.* **463**, 401–406 (2015) . https://doi.org/10.1016/j.bbrc.2015.05.084.

[48] Yano, S., Tazawa, H., Kagawa, S., Fujiwara, T. & Hoffman, R. M. FUCCI Real-Time Cell-Cycle Imaging as a Guide for Designing Improved Cancer Therapy: A Review of Innovative Strategies to Target Quiescent Chemo-Resistant Cancer Cells. *Cancers (Basel).* **12**, 2655 (2020) . https://doi.org/10.3390/cancers12092655.

[49] Sakaue-Sawano, A. *et al.* Visualizing Spatiotemporal Dynamics of Multicellular Cell-Cycle Progression. *Cell* **132**, 487–498 (2008) . https://doi.org/10.1016/j.cell.2007.12.033.

[50] Dong, P., Zhang, C., Parker, B.-T., You, L. & Mathey-Prevot, B. Cyclin D/CDK4/6 activity controls G1 length in mammalian cells. *PLoS One* **13**, e0185637 (2018) . https://dx.plos.org/10.1371/journal.pone.0185637.

[51] Jones, Z. W., Leander, R., Quaranta, V., Harris, L. A. & Tyson, D. R. A drift-diffusion checkpoint model predicts a highly variable and growth-factor-sensitive portion of the cell cycle G1 phase. *PLoS One* **13**, e0192087 (2018) . https://dx.plos.org/10.1371/journal.pone.0192087.

[52] Sugihara, K. *et al.* A new perfusion culture method with a self-organized capillary network. *PLoS One* **15**, e0240552 (2020) . https://dx.plos.org/10.1371/journal.pone.0240552.

[53] Panagiotakopoulou, M. *et al.* A Nanoprinted Model of Interstitial Cancer Migration Reveals a Link between Cell Deformability and Proliferation. *ACS Nano* **10**, 6437–6448 (2016) . https://doi.org/10.1021/acsnano.5b07406.

[54] Taubenberger, A. V. *et al.* 3D Microenvironment Stiffness Regulates Tumor Spheroid Growth and Mechanics via p21 and ROCK. *Adv. Biosyst.* **3**, 1900128 (2019) . https://doi.org/10.1002/adbi.201900128.

[55] Vittadello, S. T., McCue, S. W., Gunasingh, G., Haass, N. K. & Simpson, M. J. Mathematical Models for Cell Migration with Real-Time Cell Cycle Dynamics. *Biophys. J.* **114**, 1241–1253 (2018) . https://doi.org/10.1016/j.bpj.2017.12.041.

[56] Jin, W., Spoerri, L., Haass, N. K. & Simpson, M. J. Mathematical Model of Tumour Spheroid Experiments with Real-Time Cell Cycle Imaging. *Bull. Math. Biol.* **83**, 44 (2021) . https://doi.org/10.1007/s11538-021-00878-4.

[57] Sakaue-Sawano, A., Kobayashi, T., Ohtawa, K. & Miyawaki, A. Drug-induced cell cycle modulation leading to cell-cycle arrest, nuclear mis-segregation, or endoreplication. *BMC Cell Biol.* **12**, 2 (2011) . https://doi.org/10.1186/1471-2121-12-2.

[58] Oki, T. *et al.* A novel cell-cycle-indicator, mVenus-p27K−, identifies quiescent cells and visualizes G0–G1 transition. *Sci. Rep.* **4**, 4012 (2015) . https://doi.org/10.1038/srep04012.

[59] Bajar, B. T. *et al.* Fluorescent indicators for simultaneous reporting of all four cell cycle phases. *Nat. Methods* **13**, 993–996 (2016) . https://doi.org/10.1038/nmeth.4045.

[60] Zielke, N. & Edgar, B. A. FUCCI sensors: powerful new tools for analysis of cell proliferation. *Wiley Interdiscip. Rev. Dev. Biol.* **4**, 469–487 (2015) . https://doi.org/10.1002/wdev.189.

[61] Pawley, J. B. Fundamental Limits in Confocal Microscopy. in *Handbook Of Biological Confocal Microscopy* 20–42 (Springer US, 2006). . https://doi.org/10.1007/978-0-387-45524-2_2.

[62] Liu, H. *et al.* Visualizing long-term single-molecule dynamics in vivo by stochastic protein labeling. *Proc. Natl. Acad. Sci.* **115**, 343–348 (2018) . https://doi.org/10.1073/pnas.1713895115.

[63] Taïeb, H. M. *et al.* Osmotic pressure modulates single cell cycle dynamics inducing reversible growth arrest and reactivation of human metastatic cells. *Sci. Rep.* **11**, 13455 (2021) . https://doi.org/10.1038/s41598-021-92054-w.

[64] Krizhevsky, A., Sutskever, I. & Hinton, G. E. ImageNet classification with deep convolutional neural networks. *Commun. ACM* **60**, 84–90 (2017) . https://doi.org/10.1145/3065386.

[65] Long, J., Shelhamer, E. & Darrell, T. Fully Convolutional Networks for Semantic Segmentation. *Proc. IEEE Conf. Comput. Vis. Pattern Recognit.* 3431–3440 (2015). https://openaccess.thecvf.com/content_cvpr_2015/html/Long_Fully_Convolutional_Networks_2015_CVPR_paper.html

[66] Ronneberger, O., Fischer, P. & Brox, T. U-Net: Convolutional Networks for Biomedical Image Segmentation. in *Lecture Notes in Computer Science* vol. 9351 234–241 (Springer, Cham, 2015). . https://doi.org/10.1007/978-3-319-24574-4_28.

[67] Çiçek, Ö., Abdulkadir, A., Lienkamp, S. S., Brox, T. & Ronneberger, O. 3D U-Net: Learning Dense Volumetric Segmentation from Sparse Annotation. in *Medical Image Computing and Computer-Assisted Intervention* vol. 9901 424–432 (Springer International Publishing, 2016). . https://doi.org/10.1007/978-3-319-46723-8_49.

[68] De Fauw, J. *et al.* Clinically applicable deep learning for diagnosis and referral in retinal disease. *Nat. Med.* **24**, 1342–1350 (2018) . https://doi.org/10.1038/s41591-018-0107-6.

[69] Falk, T. *et al.* U-Net: deep learning for cell counting, detection, and morphometry. *Nat. Methods* **16**, 67–70 (2019) . https://doi.org/10.1038/s41592-018-0261-2.

[70] Moen, E. *et al.* Deep learning for cellular image analysis. *Nat. Methods* **16**, 1233–1246 (2019) . https://doi.org/10.1038/s41592-019-0403-1.

[71] Meijering, E., Dzyubachyk, O. & Smal, I. Methods for Cell and Particle Tracking. in *Methods in Enzymology* vol. 504 183–200 (Elsevier Inc., 2012). . https://doi.org/10.1016/B978-0-12-391857-4.00009-4.

[72] Emami, N., Sedaei, Z. & Ferdousi, R. Computerized cell tracking: Current methods, tools and challenges. *Vis. Informatics* **5**, 1–13 (2021) . https://doi.org/10.1016/j.visinf.2020.11.003.

[73] Downey, M., Vance, K. W. & Bretschneider, T. LineageTracker: A statistical scoring method for tracking cell lineages in large cell populations with low temporal resolution. in *2011 IEEE International Symposium on Biomedical Imaging: From Nano to Macro* 1913–1916 (IEEE, 2011). . https://doi.org/10.1109/ISBI.2011.5872783.

[74] Sbalzarini, I. F. & Koumoutsakos, P. Feature point tracking and trajectory analysis for video imaging in cell biology. *J. Struct. Biol.* **151**, 182–195 (2005) . https://doi.org/10.1016/j.jsb.2005.06.002.

[75] Tinevez, J.-Y. *et al.* TrackMate: An open and extensible platform for single-particle tracking. *Methods* **115**, 80–90 (2017) . https://doi.org/10.1016/j.ymeth.2016.09.016.

[76] Ghannoum, S. *et al.* CellMAPtracer: A User-Friendly Tracking Tool for Long-Term Migratory and Proliferating Cells Associated with FUCCI Systems. *Cells*

10, 469 (2021) . https://doi.org/10.3390/cells10020469.
[77] Koh, S.-B. *et al.* Quantitative FastFUCCI assay defines cell cycle dynamics at single-cell level. *J. Cell Sci.* **130**, 512–520 (2016) . https://doi.org/10.1242/jcs.195164.
[78] Roccio, M. *et al.* Predicting stem cell fate changes by differential cell cycle progression patterns. *Development* **140**, 459–470 (2013) . https://doi.org/10.1242/dev.086215.
[79] Lacroix, M., Toillon, R.-A. & Leclercq, G. p53 and breast cancer, an update. *Endocr. Relat. Cancer* **13**, 293–325 (2006) . https://doi.org/10.1677/erc.1.01172.
[80] Linkert, M. *et al.* Metadata matters: access to image data in the real world. *J. Cell Biol.* **189**, 777–782 (2010) . https://doi.org/10.1083/jcb.201004104.
[81] Bradley, D. & Roth, G. Adaptive Thresholding using the Integral Image. *J. Graph. Tools* **12**, 13–21 (2007) . https://doi.org/10.1080/2151237X.2007.10129236.
[82] Tarantino, N. *et al.* TNF and IL-1 exhibit distinct ubiquitin requirements for inducing NEMO–IKK supramolecular structures. *J. Cell Biol.* **204**, 231–245 (2014) . https://doi.org/10.1083/jcb.201307172.
[83] Swartz, M. A. & Fleury, M. E. Interstitial Flow and Its Effects in Soft Tissues. *Annu. Rev. Biomed. Eng.* **9**, 229–256 (2007) . https://doi.org/10.1146/annurev.bioeng.9.060906.151850.
[84] Starling, E. H. On the Absorption of Fluids from the Connective Tissue Spaces. *J. Physiol.* **19**, 312–326 (1896) . https://doi.org/10.1113/jphysiol.1896.sp000596.
[85] Staverman, A. J. The theory of measurement of osmotic pressure. *Recl. des Trav. Chim. des Pays-Bas* **70**, 344–352 (1951) . https://doi.org/10.1002/recl.19510700409.
[86] Kedem, O. & Katchalsky, A. Thermodynamic analysis of the permeability of biological membranes to non-electrolytes. *Biochim. Biophys. Acta* **27**, 229–246 (1958) . https://doi.org/10.1016/0006-3002(58)90330-5.
[87] Ho, S. N. Intracellular water homeostasis and the mammalian cellular osmotic stress response. *J. Cell. Physiol.* **206**, 9–15 (2006) . https://doi.org/10.1002/jcp.20445.
[88] Shorthouse, D. *et al.* Exploring the role of stromal osmoregulation in cancer and disease using executable modelling. *Nat. Commun.* **9**, 3011 (2018) . https://doi.org/10.1038/s41467-018-05414-y.
[89] Guo, M. *et al.* Cell volume change through water efflux impacts cell stiffness and stem cell fate. *Proc. Natl. Acad. Sci.* **114**, E8618–E8627 (2017) . https://doi.org/10.1073/pnas.1705179114.
[90] Miermont, A. *et al.* Severe osmotic compression triggers a slowdown of intracellular signaling, which can be explained by molecular crowding. *Proc. Natl. Acad. Sci.* **110**, 5725–5730 (2013) . https://doi.org/10.1073/pnas.1215367110.
[91] Appelboom, J. W. T., Brodsky, W. A., Tuttle, W. S. & Diamond, I. The freezing point depression of mammalian tissues after sudden heating in boiling distilled water. *J. Gen. Physiol.* **41**, 1153–1169 (1958) . https://doi.org/10.1085/jgp.41.6.1153.
[92] Maffly, R. H. & Leaf, A. The potential of water in mammalian tissues. *J. Gen. Physiol.* **42**, 1257–1275 (1959) . https://doi.org/10.1085/jgp.42.6.1257.
[93] Zhang, W. *et al.* Spatiotemporal Measurement of Osmotic Pressures by FRET

Imaging. *Angew. Chemie Int. Ed.* **60**, 6488–6495 (2021) . https://doi.org/10.1002/anie.202011983.

[94] Havard, M., Dautry, F. & Tchénio, T. A Dormant State Modulated by Osmotic Pressure Controls Clonogenicity of Prostate Cancer Cells. *J. Biol. Chem.* **286**, 44177–44186 (2011) . https://doi.org/10.1074/jbc.M111.262709.

[95] Miermont, A., Lee, S. W. L., Adriani, G. & Kamm, R. D. Quantitative screening of the effects of hyper-osmotic stress on cancer cells cultured in 2- or 3-dimensional settings. *Sci. Rep.* **9**, 13782 (2019) . https://doi.org/10.1038/s41598-019-50198-w.

[96] Thiemicke, A. & Neuert, G. Kinetics of osmotic stress regulate a cell fate switch of cell survival. *Sci. Adv.* **7**, eabe1122 (2021) . https://doi.org/10.1126/sciadv.abe1122.

[97] Beck, F.-X., Dörge, A. & Thurau, K. Cellular Osmoregulation in Renal Medulla. *Kidney Blood Press. Res.* **11**, 174–186 (1988) . https://doi.org/10.1159/000173161e/FullText/173161.

[98] Jung, H. J., Park, J.-Y., Jeon, H.-S. & Kwon, T.-H. Aquaporin-5: A Marker Protein for Proliferation and Migration of Human Breast Cancer Cells. *PLoS One* **6**, e28492 (2011) . https://dx.plos.org/10.1371/journal.pone.0028492.

[99] Burg, M. B. Molecular basis of osmotic regulation. *Am. J. Physiol. Physiol.* **268**, F983–F996 (1995) . https://doi.org/10.1152/ajprenal.1995.268.6.F983.

[100] Bellí, G., Garí, E., Aldea, M. & Herrero, E. Osmotic stress causes a G1 cell cycle delay and downregulation of Cln3/Cdc28 activity in Saccharomyces cerevisiae. *Mol. Microbiol.* **39**, 1022–1035 (2001) . https://doi.org/10.1046/j.1365-2958.2001.02297.x.

[101] Krokowski, D. *et al.* GADD34 Function in Protein Trafficking Promotes Adaptation to Hyperosmotic Stress in Human Corneal Cells. *Cell Rep.* **21**, 2895–2910 (2017) . https://doi.org/10.1016/j.celrep.2017.11.027.

[102] Sharma, G. *et al.* p53 dependent apoptosis and cell cycle delay induced by heteroleptic complexes in human cervical cancer cells. *Biomed. Pharmacother.* **88**, 218–231 (2017) . https://doi.org/10.1016/j.biopha.2017.01.044.

[103] Dimozi, A., Mavrogonatou, E., Sklirou, A. & Kletsas, D. Oxidative stress inhibits the proliferation, induces premature senescence and promotes a catabolic phenotype in human nucleus pulposus intervertebral disc cells. *Eur. Cells Mater.* **30**, 89–103 (2015) . https://doi.org/10.22203/eCM.v030a07.

[104] Berghmans, S. *et al.* tp53 mutant zebrafish develop malignant peripheral nerve sheath tumors. *Proc. Natl. Acad. Sci.* **102**, 407–412 (2005) . https://doi.org/10.1073/pnas.0406252102.

[105] Zhan, Q., Bae, I., Kastan, M. B. & Fornace, A. J. The p53-dependent γ-Ray Response of GADD45. *Cancer Res.* **54**, 2755–2760 (1994). https://cancerres.aacrjournals.org/content/54/10/2755.

[106] Decker, A. M. *et al.* Sympathetic Signaling Reactivates Quiescent Disseminated Prostate Cancer Cells in the Bone Marrow. *Mol. Cancer Res.* **15**, 1644–1655 (2017) . https://doi.org/10.1158/1541-7786.MCR-17-0132.

[107] Chicheportiche, A., Ruat, M., Boussin, F. D. & Daynac, M. Isolation of Neural Stem and Progenitor Cells from the Adult Brain and Live Imaging of Their Cell Cycle with the FUCCI System. in *Methods in Molecular Biology* vol. 1686 69–78 (Humana Press Inc., 2018). https://doi.org/10.1007/978-1-4939-7371-2_5.

[108] Yano, S. *et al.* Spatial–temporal FUCCI imaging of each cell in a tumor demonstrates locational dependence of cell cycle dynamics and chemoresponsiveness. *Cell Cycle* **13**, 2110–2119 (2014) .

https://doi.org/10.4161/cc.29156.
[109] Onozato, Y., Kaida, A., Harada, H. & Miura, M. Radiosensitivity of quiescent and proliferating cells grown as multicellular tumor spheroids. *Cancer Sci.* **108**, 704–712 (2017) . https://doi.org/10.1111/cas.13178.
[110] Kamemizu, C. & Fujimori, T. Distinct dormancy progression depending on embryonic regions during mouse embryonic diapause†. *Biol. Reprod.* **100**, 1204–1214 (2019) . https://doi.org/10.1093/biolre/ioz017.
[111] Barney, L. E. *et al.* Tumor cell–organized fibronectin maintenance of a dormant breast cancer population. *Sci. Adv.* **6**, eaaz4157 (2020) . https://doi.org/10.1126/sciadv.aaz4157.
[112] Vousden, K. H. Switching from life to death: The Miz-ing link between Myc and p53. *Cancer Cell* **2**, 351–352 (2002) . https://doi.org/10.1016/S1535-6108(02)00186-1.
[113] Gillis, L. D., Leidal, A. M., Hill, R. & Lee, P. W. K. p21 Cip1/WAF1 mediates cyclin B1 degradation in response to DNA damage. *Cell Cycle* **8**, 253–256 (2009) . https://doi.org/10.4161/cc.8.2.7550.
[114] Lee, J., Kim, J. A., Barbier, V., Fotedar, A. & Fotedar, R. DNA Damage Triggers p21 WAF1 -dependent Emi1 Down-Regulation That Maintains G2 Arrest. *Mol. Biol. Cell* **20**, 1891–1902 (2009) . https://doi.org/10.1091/mbc.e08-08-0818.
[115] Cheang, M. C. U. *et al.* Ki67 Index, HER2 Status, and Prognosis of Patients With Luminal B Breast Cancer. *JNCI J. Natl. Cancer Inst.* **101**, 736–750 (2009) . https://doi.org/10.1093/jnci/djp082.
[116] Yerushalmi, R., Woods, R., Ravdin, P. M., Hayes, M. M. & Gelmon, K. A. Ki67 in breast cancer: prognostic and predictive potential. *Lancet. Oncol.* **11**, 174–83 (2010) . https://doi.org/10.1016/S1470-2045(09)70262-1.
[117] Corliss, J. O. Locomotion of Tissue Cells. *Trans. Am. Microsc. Soc.* **93**, 290 (1974) . https://doi.org/10.2307/3225317.
[118] Oster, G. F. & Perelson, A. S. The Physics of Cell Motility. *J. Cell Sci.* **1987**, 35–54 (1987) . https://doi.org/10.1242/jcs.1987.Supplement_8.3.
[119] Bray, D., Money, N. P., Harold, F. M. & Bamburg, J. R. Responses of growth cones to changes in osmolality of the surrounding medium. *J. Cell Sci.* **98**, 507–515 (1991) . https://doi.org/10.1242/jcs.98.4.507.
[120] Chen, T. *et al.* Hypotonicity promotes epithelial gap closure by lamellipodial protrusion. *Prog. Biophys. Mol. Biol.* **148**, 60–64 (2019) . https://doi.org/10.1016/j.pbiomolbio.2017.09.021.
[121] Zatulovskiy, E., Zhang, S., Berenson, D. F., Topacio, B. R. & Skotheim, J. M. Cell growth dilutes the cell cycle inhibitor Rb to trigger cell division. *Science (80-.).* **369**, 466–471 (2020) . https://doi.org/10.1126/science.aaz6213.
[122] Ferrara, N. & Davis-Smyth, T. The Biology of Vascular Endothelial Growth Factor. *Endocr. Rev.* **18**, 4–25 (1997) . https://doi.org/10.1210/edrv.18.1.0287.
[123] Valastyan, S. & Weinberg, R. A. Tumor Metastasis: Molecular Insights and Evolving Paradigms. *Cell* **147**, 275–292 (2011) . https://doi.org/10.1016/j.cell.2011.09.024.
[124] Martin, J. D., Seano, G. & Jain, R. K. Normalizing Function of Tumor Vessels: Progress, Opportunities, and Challenges. *Annu. Rev. Physiol.* **81**, 505–534 (2019) . https://doi.org/10.1146/annurev-physiol-020518-114700.
[125] Mohammadi, H. & Sahai, E. Mechanisms and impact of altered tumour mechanics. *Nat. Cell Biol.* **20**, 766–774 (2018) . http://dx.doi.org/10.1038/s41556-018-0131-2.

[126] Northey, J. J., Przybyla, L. & Weaver, V. M. Tissue Force Programs Cell Fate and Tumor Aggression. *Cancer Discov.* **7**, 1224–1237 (2017) . https://doi.org/10.1158/2159-8290.CD-16-0733.
[127] Wirtz, D., Konstantopoulos, K. & Searson, P. C. The physics of cancer: the role of physical interactions and mechanical forces in metastasis. *Nat. Rev. Cancer* **11**, 512–522 (2011) . https://doi.org/10.1038/nrc3080.
[128] Koumoutsakos, P., Pivkin, I. & Milde, F. The Fluid Mechanics of Cancer and Its Therapy. *Annu. Rev. Fluid Mech.* **45**, 325–355 (2013) . https://doi.org/10.1146/annurev-fluid-120710-101102.
[129] Swartz, M. A. & Lund, A. W. Lymphatic and interstitial flow in the tumour microenvironment: linking mechanobiology with immunity. *Nat. Rev. Cancer* **12**, 210–219 (2012) . https://doi.org/10.1038/nrc3186.
[130] Weiss, L., Bronk, J., Pickren, J. W. & Lane, W. W. Metastatic patterns and target organ arterial blood flow. *Invasion and Metastasis* **1**, 126–135 (1981). https://europepmc.org/article/med/7188382
[131] Munson, J. M., Bellamkonda, R. V. & Swartz, M. A. Interstitial Flow in a 3D Microenvironment Increases Glioma Invasion by a CXCR4-Dependent Mechanism. *Cancer Res.* **73**, 1536–1546 (2013) . https://doi.org/10.1158/0008-5472.CAN-12-2838.
[132] Cornelison, R. C., Brennan, C. E., Kingsmore, K. M. & Munson, J. M. Convective forces increase CXCR4-dependent glioblastoma cell invasion in GL261 murine model. *Sci. Rep.* **8**, 17057 (2018) . https://doi.org/10.1038/s41598-018-35141-9.
[133] Al-Mehdi, A. B. *et al.* Intravascular origin of metastasis from the proliferation of endothelium-attached tumor cells: a new model for metastasis. *Nat. Med.* **6**, 100–102 (2000) . https://doi.org/10.1038/71429.
[134] Kienast, Y. *et al.* Real-time imaging reveals the single steps of brain metastasis formation. *Nat. Med.* **16**, 116–122 (2010) . https://doi.org/10.1038/nm.2072.
[135] Kusumbe, A. P., Ramasamy, S. K. & Adams, R. H. Coupling of angiogenesis and osteogenesis by a specific vessel subtype in bone. *Nature* **507**, 323–328 (2014) . https://doi.org/10.1038/nature13145.
[136] Lassailly, F., Foster, K., Lopez-Onieva, L., Currie, E. & Bonnet, D. Multimodal imaging reveals structural and functional heterogeneity in different bone marrow compartments: functional implications on hematopoietic stem cells. *Blood* **122**, 1730–1740 (2013) . https://doi.org/10.1182/blood-2012-11-467498.
[137] Bixel, M. G. *et al.* Flow Dynamics and HSPC Homing in Bone Marrow Microvessels. *Cell Rep.* **18**, 1804–1816 (2017) . https://dx.doi.org/10.1016/j.celrep.2017.01.042.
[138] Chen, M. B., Whisler, J. A., Jeon, J. S. & Kamm, R. D. Mechanisms of tumor cell extravasation in an in vitro microvascular network platform. *Integr. Biol.* **5**, 1262 (2013) . https://doi.org/10.1039/c3ib40149a.
[139] Regmi, S., Fu, A. & Luo, K. Q. High Shear Stresses under Exercise Condition Destroy Circulating Tumor Cells in a Microfluidic System. *Sci. Rep.* **7**, 39975 (2017) . https://doi.org/10.1038/srep39975.
[140] Carlson, P. *et al.* Targeting the perivascular niche sensitizes disseminated tumour cells to chemotherapy. *Nat. Cell Biol.* **21**, 238–250 (2019) . https://doi.org/10.1038/s41556-018-0267-0.
[141] Follain, G. *et al.* Hemodynamic Forces Tune the Arrest, Adhesion, and Extravasation of Circulating Tumor Cells. *Dev. Cell* **45**, 33-52.e12 (2018) . https://doi.org/10.1016/j.devcel.2018.02.015.

[142] Eyer, K., Kuhn, P., Stratz, S. & Dittrich, P. S. A Microfluidic Chip for the Versatile Chemical Analysis of Single Cells. *J. Vis. Exp.* **80**, 50618 (2013) . https://dx.doi.org/10.3791/50618.
[143] Robinson, T., Kuhn, P., Eyer, K. & Dittrich, P. S. Microfluidic trapping of giant unilamellar vesicles to study transport through a membrane pore. *Biomicrofluidics* **7**, 044105 (2013) . https://doi.org/10.1063/1.4816712.
[144] Lorensen, W. E. & Cline, H. E. Marching cubes: A high resolution 3D surface construction algorithm. *ACM SIGGRAPH Comput. Graph.* **21**, 163–169 (1987) . https://doi.org/10.1145/37402.37422.
[145] Chiang, S. P. H., Cabrera, R. M. & Segall, J. E. Tumor cell intravasation. *Am. J. Physiol. Physiol.* **311**, C1–C14 (2016) . https://doi.org/10.1152/ajpcell.00238.2015.
[146] Schindelin, J. *et al.* Fiji: an open-source platform for biological-image analysis. *Nat. Methods* **9**, 676–682 (2012) . https://doi.org/10.1038/nmeth.2019.
[147] Sommer, C., Straehle, C., Kothe, U. & Hamprecht, F. A. Ilastik: Interactive learning and segmentation toolkit. in *2011 IEEE International Symposium on Biomedical Imaging: From Nano to Macro* 230–233 (IEEE, 2011). . https://doi.org/10.1109/ISBI.2011.5872394.
[148] Berg, S. *et al.* ilastik: interactive machine learning for (bio)image analysis. *Nat. Methods* **16**, 1226–1232 (2019) . https://doi.org/10.1038/s41592-019-0582-9.
[149] McQuin, C. *et al.* CellProfiler 3.0: Next-generation image processing for biology. *PLOS Biol.* **16**, e2005970 (2018) . https://doi.org/10.1371/journal.pbio.2005970.
[150] Al-Kofahi, Y., Zaltsman, A., Graves, R., Marshall, W. & Rusu, M. A deep learning-based algorithm for 2-D cell segmentation in microscopy images. *BMC Bioinformatics* **19**, 365 (2018) . https://doi.org/10.1186/s12859-018-2375-z.
[151] Funke, J., Mais, L., Champion, A., Dye, N. & Kainmueller, D. A Benchmark for Epithelial Cell Tracking. in *Lecture Notes in Computer Science* vol. 11134 LNCS 437–445 (Springer, Cham, 2019). . https://doi.org/10.1007/978-3-030-11024-6_33.
[152] Caicedo, J. C. *et al.* Nucleus segmentation across imaging experiments: the 2018 Data Science Bowl. *Nat. Methods* **16**, 1247–1253 (2019) . https://doi.org/10.1038/s41592-019-0612-7.
[153] Stringer, C., Wang, T., Michaelos, M. & Pachitariu, M. Cellpose: a generalist algorithm for cellular segmentation. *Nat. Methods* **18**, 100–106 (2021) . https://doi.org/10.1038/s41592-020-01018-x.
[154] Lee, H. J., Ewere, A., Diaz, M. F. & Wenzel, P. L. TAZ responds to fluid shear stress to regulate the cell cycle. *Cell Cycle* **17**, 147–153 (2018) . https://doi.org/10.1080/15384101.2017.1404209.
[155] Zanconato, F. *et al.* Genome-wide association between YAP/TAZ/TEAD and AP-1 at enhancers drives oncogenic growth. *Nat. Cell Biol.* **17**, 1218–1227 (2015) . https://doi.org/10.1038/ncb3216.
[156] Lei, Q.-Y. *et al.* TAZ Promotes Cell Proliferation and Epithelial-Mesenchymal Transition and Is Inhibited by the Hippo Pathway. *Mol. Cell. Biol.* **28**, 2426–2436 (2008) . https://doi.org/10.1128/MCB.01874-07.
[157] Chang, S.-F. *et al.* Tumor cell cycle arrest induced by shear stress: Roles of integrins and Smad. *Proc. Natl. Acad. Sci.* **105**, 3927–3932 (2008) . https://dx.doi.org/10.1073%2Fpnas.0712353105.
[158] Yankaskas, C. L. *et al.* The fluid shear stress sensor TRPM7 regulates tumor cell intravasation. *Sci. Adv.* **7**, eabh3457 (2021) .

https://doi.org/10.1126/sciadv.abh3457.
[159] Wei, C. *et al.* Calcium flickers steer cell migration. *Nature* **457**, 901–905 (2009) . https://doi.org/10.1038/nature07577.

Appendix A

FUCCItrack User's Guide

Contents

1. Introduction

FUCCItrack is a 2D live cell visualization and analysis software. It allows users to analyze time lapse imaging data sets using the FUCCI/FUCCI2 systems, or any other two-color fluorophores. With the 2D time lapse data, FUCCItrack can perform numerous quantifications to study cell proliferation, migration, changes in nuclear and cell morphology as well as single cell cycle dynamics analysis. The graphical user interface (GUI) makes it easy for non-programming users to segment and track single cells in an automatic manner, while containing manual corrections functions to correct for errors.

Designed with the goal to be a multi-purpose platform, FUCCItrack is one software to visualize, analyze and create high quality visuals for presentation. It is modular by design and different features, or modules could be added to meet user specific needs. It is mainly automatic and therefore efficient in segmentation and tracking single cells, while being easy to use with an intuitive user interface and extensive documentation. FUCCItrack is designed to be open-source and hence has a licensing scheme that gives users the most freedom.

2. Starting the program

Select the FUCCItrack icon from the application menu in MATLAB or launch “FUCCItrack.exe” as a standalone software without MATLAB (for Windows users only). When FUCCItrack is running, a window like the one shown in Figure 1 appears on the screen. This starting page is divided in several major regions:

1) **Module toolbar:** provides quick access to some important modules. See specific module description.
2) **Tools:** allows user to navigate through the timelapse datasets and the single cell during segmentation and tracking.
3) **Status & Visualization** contains a log window to follow what is happening while using the software. It also contains a progress bar and button to create plots related to single cell tracking.

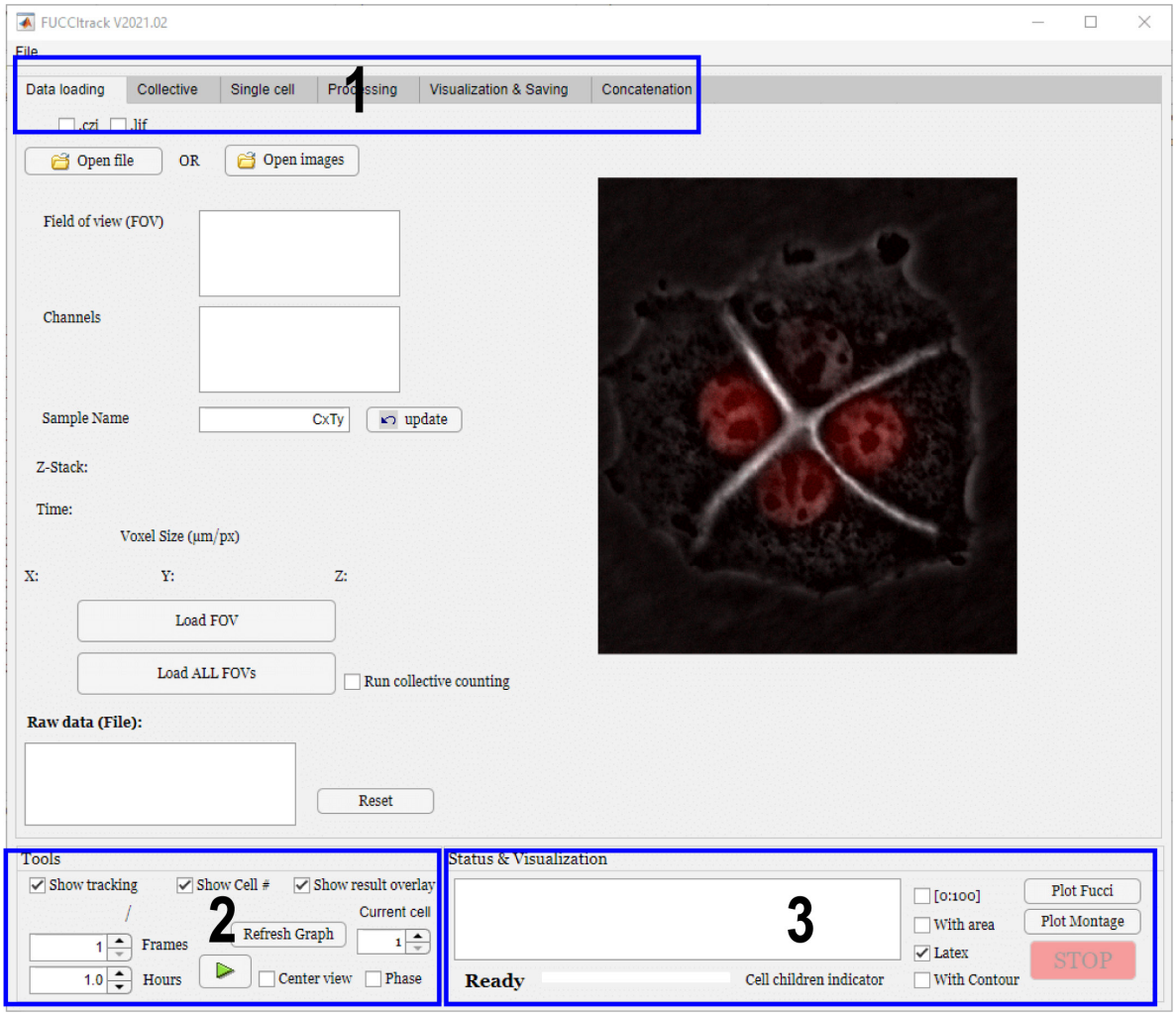

Figure 1. The FUCCItrack start page with three main regions: 1) the module toolbar, 2) the “Tools” panel and the 3) “Status & Visualization” panel.

3. Module description – Data loading

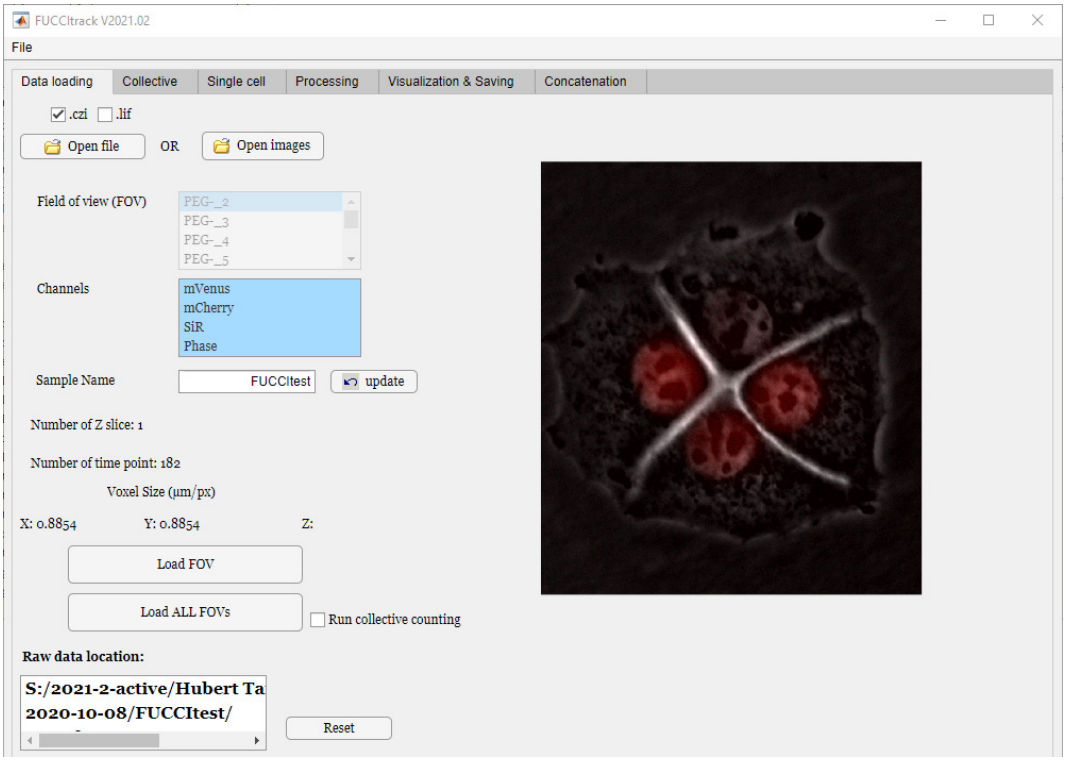

Figure 2. Data loading module

This is the first module that opens after launching FUCCItrack software. It contains all the different buttons and options to load the microscope data with the corresponding metadata. Please note that a minimum of two fluorescence channels (mCherry/mVenus) and one phase contrast or bright field or cell membrane dye (in our case approximated by live F-actin staining) are required for FUCCItrack.

.czi or .lif

User is invited to pick one of the two extensions presented corresponding to Zeiss or Leica microscope.

Open file

After picking the extension, user can press this button and select the location of the raw data file on the computer. This raw data can contain one or more fields of view (FOV).

Upon opening the files, metadata is read directly and updated in the software as presented below:

- "Field of view (FOV)": if the raw data contains several fields of view, it is possible to select the one of interest by directly clicking on the name. This is only possible

with the “Open file” button since “Open images” can only load one field of view at the time.

- “Channels”: this list contains the name of the channels used during the experiment and is updated automatically from the metadata of the raw files or the folder structure.
- “Sample name”: this field lets users choose the sample name corresponding to a specific FOV. All exported data and associated files from the software will start with the sample name as prefix. The “Update” button allows users to later change this sample name and update all files created within the software.
- “Number of Z slice”: this field is updated from the metadata and indicates the number of slices in the z stack. This value should always be 1 since 3D is not yet supported in the current version.
- “Number of time point”: this field enumerates the number of frames corresponding to number of time points in the time lapse experiment.
- “Voxel Size (µm/px)”: this field lists the voxel size in all directions and is updated from the metadata of the raw file. If the “Open images” button is selected, the user should manually input the voxel size.

Open images

This is to be used if the user does not have the raw data in the .czi or .lif format but rather a sequence of images corresponding to one field of view only. In this case, the images to be loaded should be with the .tif extension and organized in folders as follow:

- *Sample_name*/Raw data/mCherry/image_001.tif to image_182.tif
- *Sample_name*/Raw data/mVenus//image_001.tif to image_182.tif
- *Sample_name*/Raw data/Phase/image_001.tif to image_182.tif

With *Sample_name* replaced with the actual sample name, for example “FUCCItest” as seen above. Right after clicking on “Open images”, the user will be asked to select the folder that should be the one with the folder name corresponding to the sample name. The subfolder mCherry, mVenus and Phase have to be called like this.

If the raw data contains more than one FOV, then 2 options are possible.

Load FOV

User can pick the FOV of interest (by clicking on its name from the FOV list) and use the “Load FOV” button. The user will be asked to select a folder that will be used to store the processed data and results from this FOV (under a newly created folder

named after the sample name). The software will then load all the images of this FOV inside the software, with no options to change the FOV afterwards.

Load ALL FOVs

This is intended for raw files that contains more than one FOV.

I. Without “Run collective counting”: this will load in batch all the FOVs from the raw data and for every FOV it will create a folder with the sample name containing three data files: “FUCCItest_tmp_data.mat” (includes all the data from the collective and single cell tracking), “FUCCItest_state.mat” (includes the state of every button of the software for future reloading of a session) and “FUCCItest_im_only.mat” (includes all the images of this FOV).

II. With “Run collective counting”: when this option is selected, the software will load in batch all the FOVs like previously but will also launch the collective module to directly obtain cell proliferation behavior. More details on the collective module are listed in the next section.

4. Module description – Collective

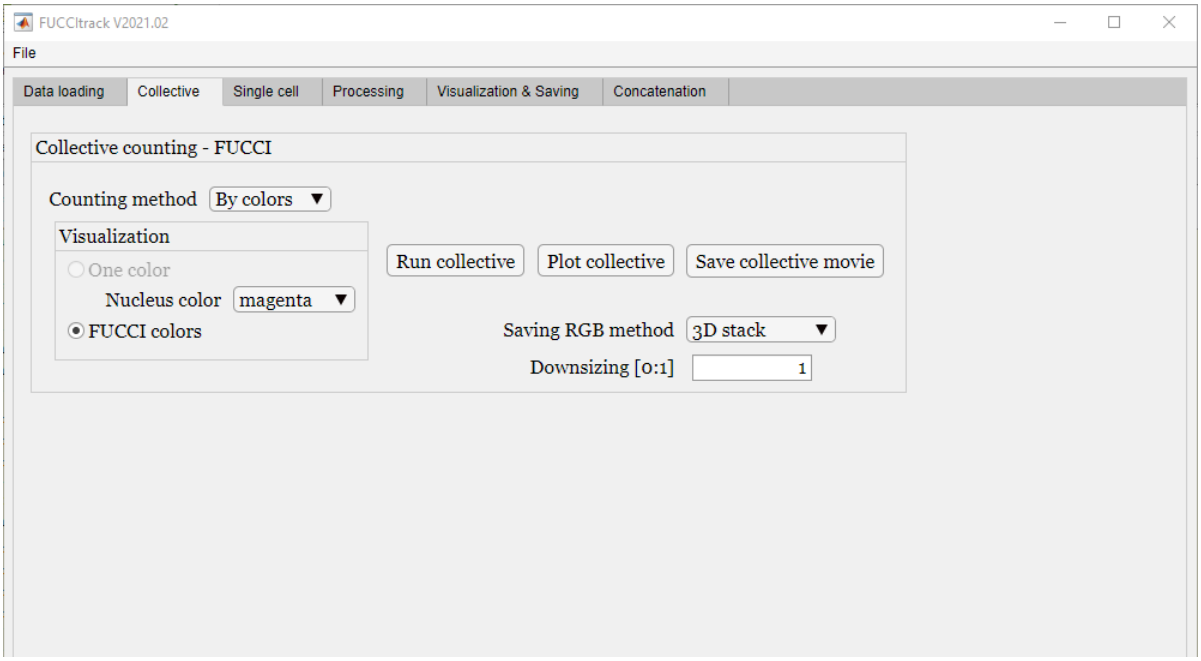

Figure 3. Collective module

The collective module allows user to run an automatic algorithm to segment and count the number of FUCCI/FUCCI2 cells over time.

Counting method

- "By colors": this option enables the counting of the cell but with the information about which channel they belong. This is intended if user is interested in the fraction of mCherry$^+$/mVenus$^-$ (G1 phase) and mVenus$^+$ (S/G2/M phase).
- "Merged": this option counts the cells independently of their channel of origin and gives a total number of cells as a function of time.

Visualization

Upon cell counting, one of the outputs is a time lapse video of the cells with their nuclei colored. There are 2 options as to what colors can appear on this video.

- "One color": user can pick the colors they want the nuclei to be appearing.
- "FUCCI color": the colors used will be the original FUCCI/FUCCI2 color, red and green.

Run collective

After selecting the options for the counting method and the visualization, the user can click this button to start the counting process.

Plot collective

This button will create a plot with the number of cells as a function of time, as well as the fraction of mCherry$^+$/mVenus$^-$ and mVenus$^+$ if the counting method "By colors" was chosen.

Saving RGB method

the software merges the phase and/or cell shape channel with the nuclei segmentation results and saves this RGB composite.

- "3D stack": the output will be one multi-TIFFs file containing all the time points.
- "Sequential": the output will consist in a sequence of tif files corresponding to every time point.
- "Downsizing [0:1]": It is the ratio of the original size to reduced sized (in pixels). The user can pick a value between 0 and 1 and this will be used to downsize the original raw data for saving storage purposes.

Save collective movie

this button creates a movie from the raw images, overlaid with the nuclei segmentation. The color of the nuclei here is defined by the "Visualization" option.

5. Module description – Single cell module

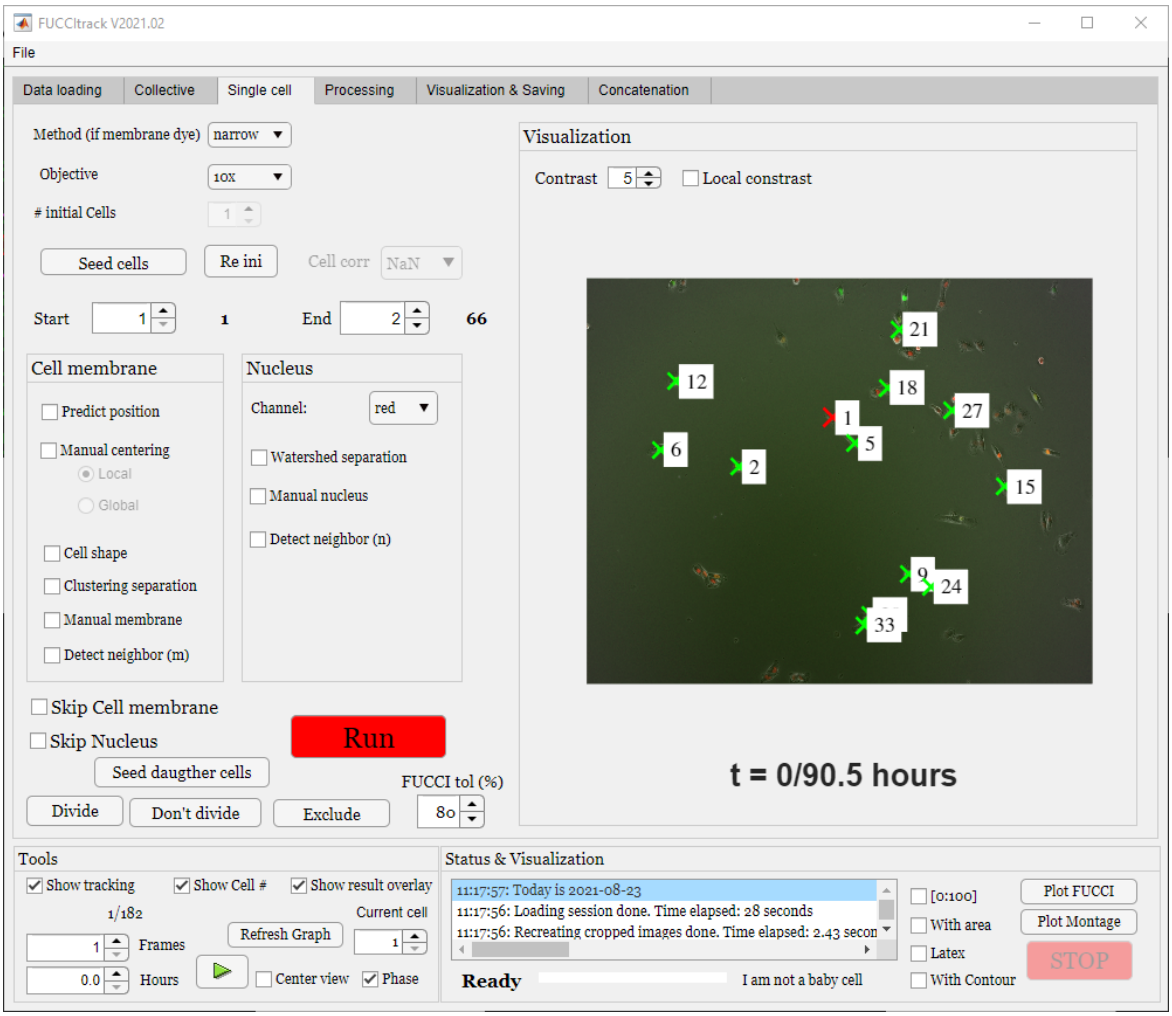

Figure 4. Single cell module with the “Tools” and “Status & Visualization” panels.

5.1 General components

This is the module to perform the segmentation and tracking of the single cells. In addition to the single cell module, the “Tools” and “Status & Visualization” panels are also shown since they are the most useful in this module.

During the segmentation and tracking, there is always a region of interest (ROI) that is defined around the cell of interest. The size of this ROI is defined as follows: cell diameter * margin, both being parameters of the software that can be tuned depending on preferences. The default values are 30 µm for the diameter and 2 for the margin, resulting in a ROI of 60x60 µm, to make sure the ROI captures at least one complete cell.

Method (if cell shape)

This button contains three possible options to perform the automatic cell segmentation (if a fluorescence dye is present). In all three methods, a local thresholding is performed to obtain a binary mask. The methods chosen will yield different threshold values for the segmentation.

- "Narrow": this is the default method. It uses a ROI narrower than the initial ROI (60x60 µm) by 20% (this value can also be tuned by users in the source code) to calculate the threshold value. This is specifically useful when several cells are present in the ROI, resulting in a wrong threshold for the cell of interest.
- "Large": this method uses the whole original ROI (60x60 µm) to compute the threshold value for the cell shape.
- "History": this option is only available when at least one segmentation was done with the cell of interest. Instead of calculating a new threshold value every time point, the software will use the previously calculated threshold value to segment the cell in new time points. This method gives the best results with live stainings that are stable over time and for which a constant threshold value over time is enough to segment the cell shape.

If the user only has phase contrast or bright field, then this field has no impact. Indeed, there is no easy way to perform automatic segmentation on bright field of phase contrast imaging, so the user should only use the "Manual shape" button to manually segment the cell shape.

Objective

This field only has an informative value. Since retrieving this specific information from the metadata was not possible, the user can specify here the value of objective magnification used through this field.

 # initial cells

The first time the dataset is loaded, it is possible to specify how many cells the user wants to select on the first time point. After clicking on the "Seed cells" button, the seeding procedure will be repeated in a row for as many cells as selected in the "# initial cells" field. It is also always possible to seed cells from a later point by clicking the "Seed cells" button in another frame.

Seed cells

This button will start the initialization procedure to select the cell of interest by opening a new window and a dialog box as shown in Fig. 5. The new window contains side by side the images coming from the different channels. First the user must zoom inside the field of view to better see the cell of interest (Fig. 5A). When the magnification is enough to see only the cell of interest, the user should click “Yes” on the dialog box that appeared asking “Done with zooming?” (Fig. 5B). The mouse cursor will change, and the user must click directly over the cell of interest. An initialization process will then start with this cell to segment the nucleus and cell whenever possible for the seeding time point (Fig. 5C).

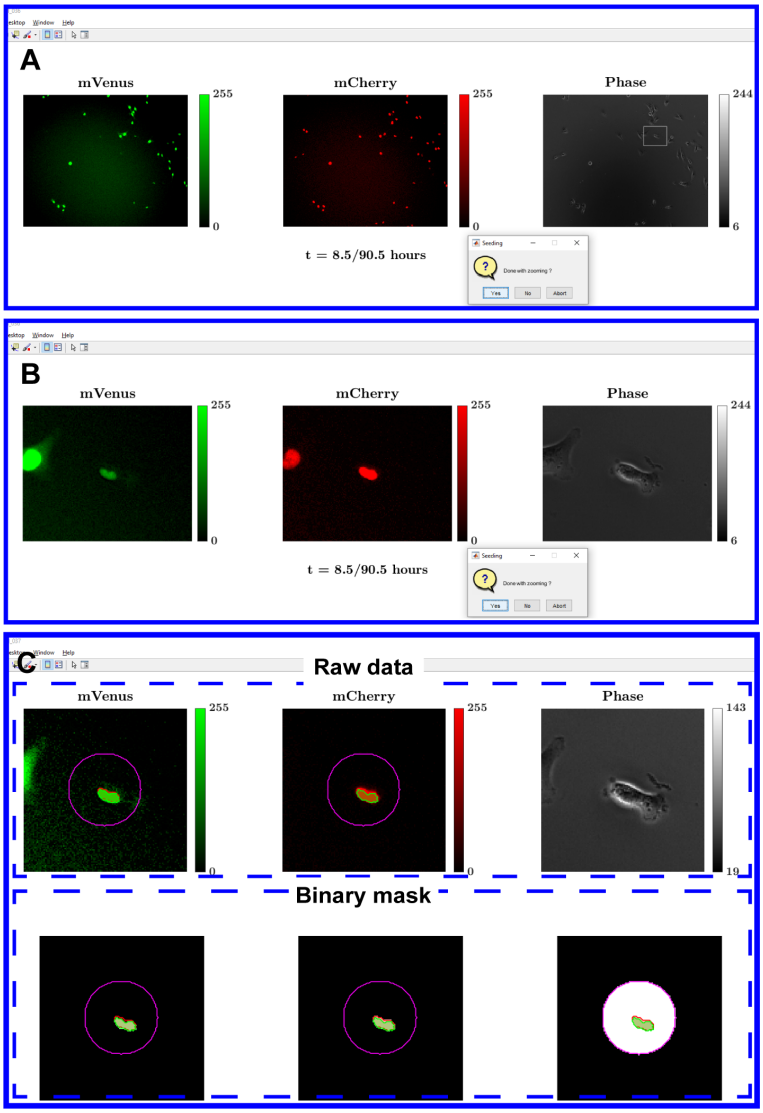

Figure 5. External window for single cell tracking and seeding cell procedure

Re ini

This field stands for “Rerun Initialization” and allows to start again the initialization phase with different settings in case the automatic segmentation failed.

Start and End

These two fields are used together with the “Run” button to specify for which time points the segmentation and tracking should be done. It ranges from 1 to the number of time points in the experiment. Next to these two fields are two numbers written in green that correspond to the beginning and end of the tracking for the current cell selected.

Skip cell shape

This option is only to be used if the segmentation and tracking was already performed and stored. It allows user to run again the segmentation of the nucleus, while keeping the cell tracking information stored. This can be useful if the automatic nucleus segmentation failed for example.

Skip nucleus

This option is an analogue to the previous function and let users run again the segmentation of the cell shape without modifying the cell nucleus segmentation.

Divide/Don’t divide/Exclude

These buttons work together and inform on the status of the current cell (Fig 6). For every tracked cell, a status concerning its cell cycle at the end of the tracking should be assigned by the user upon clicking on one of the three buttons. By default, all cells are considered excluded until a cell performs a division, or don’t divide by the end of the experiment. Exclusion criteria are defined by every user but can be (i) absence of mCherry or mVenus signal in the nucleus, (ii) cells getting out of the field of view during the tracking or (iii) failed division.

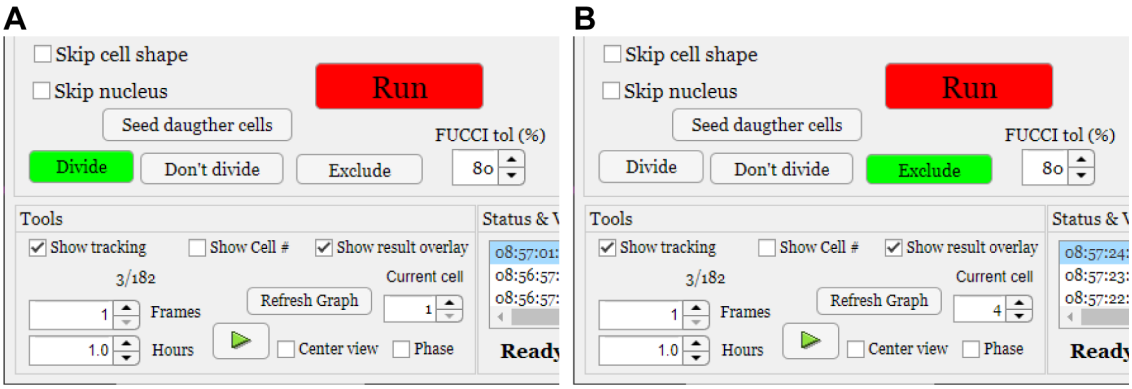

Figure 6. Divide/Don't divide/Exclude example. **A)** User interface for a cell that divides and **B)** for a cell that is excluded.

This buttons only assign cells to a category within the software for the processing module. For example, only cells that divide will be used to calculate the duration of cell cycle.

Seed daughter cells

If the user is interested in tracking the daughter cells of a cell that divided, by pressing this button the seeding of the daughter cells will be done automatically with contrast to the "Seed cells" button that requires manual input. This button is equivalent to "Seed cells", but does not require any inputs from the user since the last frame of the parent cells will be used and considered as the first frame of the two new daughter cells.

FUCCI tol (%)

In the ideal case scenario, the segmentation of the nucleus should be the same in shape and area for mCherry and mVenus channels. However, often the segmentation yields slightly different results for both channels. To address this discrepancy, this parameter (FUCCI tol, meaning FUCCI tolerance) is used to decide how much of the segmented nucleus in mCherry channel should overlap in the mVenus channel. The setting can be defined by the user and is set at 80 % by default. If the tolerance number is low, it means that segmentation in mCherry and mVenus could differ a lot, which will trigger a safety measure that will ask users to manually specify which one of the two channel yields the correct segmentation.

In terms of tracking and segmentation itself, certain options can be selected to assist the automatic tracking or let the user manually perform some tasks. These options are separated in "Cell shape" and "Nucleus" panel, as shown in Fig 7.

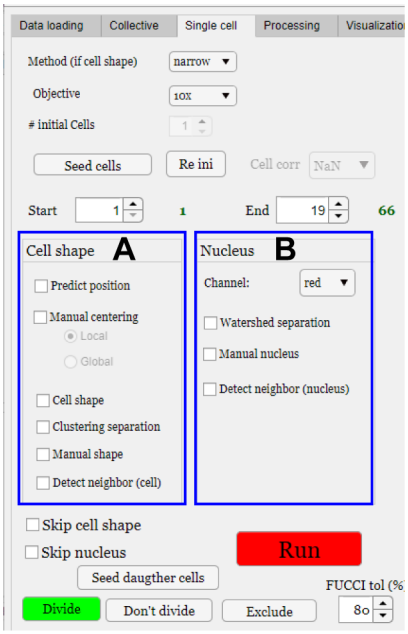

Figure 7. "Cell shape" and "Nucleus" panel

5.2 Segmentation & tracking - Cell shape panel

Please refer to Figure 7A to see where the options are in the GUI.

Predict position

After seeding, the program looks in the search window around the previous position for nuclei signal via automated adaptative thresholding. It then compares several features of the previous nucleus found with the potential candidates. The features used are: (i) area, (ii) distance to previous nuclei, (iii) eccentricity, (iv) mean intensity, (v) standard deviation intensity and (vi) maximum intensity. The software computes the relative difference between the previously correct position and the current candidates and looks for the minimum difference in every feature. The cell chosen will be the one that has the most features with the minimum relative difference to the previous nuclei. If this option is not selected, the tracking starts from the previous position.

Manual centering

If this is selected, it forces the user to manually select the center of the nucleus in case other automated ways do not manage to localize the cell (due to nucleus signal too low, too many neighbor cells). Both the cell and nucleus will have to contain the position input by the user. It can be "local", meaning the search window corresponds to the previous position found. But it can also be "global" in case the cell is out of the search window. In this case, the user can select the nucleus position from the total raw image.

Cell shape

By default, this option is not selected, and this means that FUCCItrack will not try to segment the cell shape. It will create an arbitrary circle around the center of the nucleus already previously found automatically or by user input. The circle is just a proxy for the cell outreach and its diameter can be modified by the user. If “Cell shape” is selected, the segmentation of the cell shape will be performed as shown in Figure 8.

Clustering separation (only relevant if cell shape is selected)

This is useful if you have two or ***k*** cells that are overlapping or touching. It allows to separate the cells using a ***k***-means clustering methods using the pixels from the segmentation as input for the clustering.

Manual shape (only relevant if cell shape is selected):

If the automated segmentation failed the user can manually draw the cell shape to perform the segmentation. This option is particularly necessary for users who whish to obtain cell shape based only on phase contrast or bright field since the automatic segmentation requires a fluorescence channel to perform well.

Detect neighbor (cell) (only relevant if cell shape is selected)

This option is useful if previously segmented cells are nearby the currently tracked cell. This option will delete previously segmented cells to avoid duplicate or wrong segmentation.

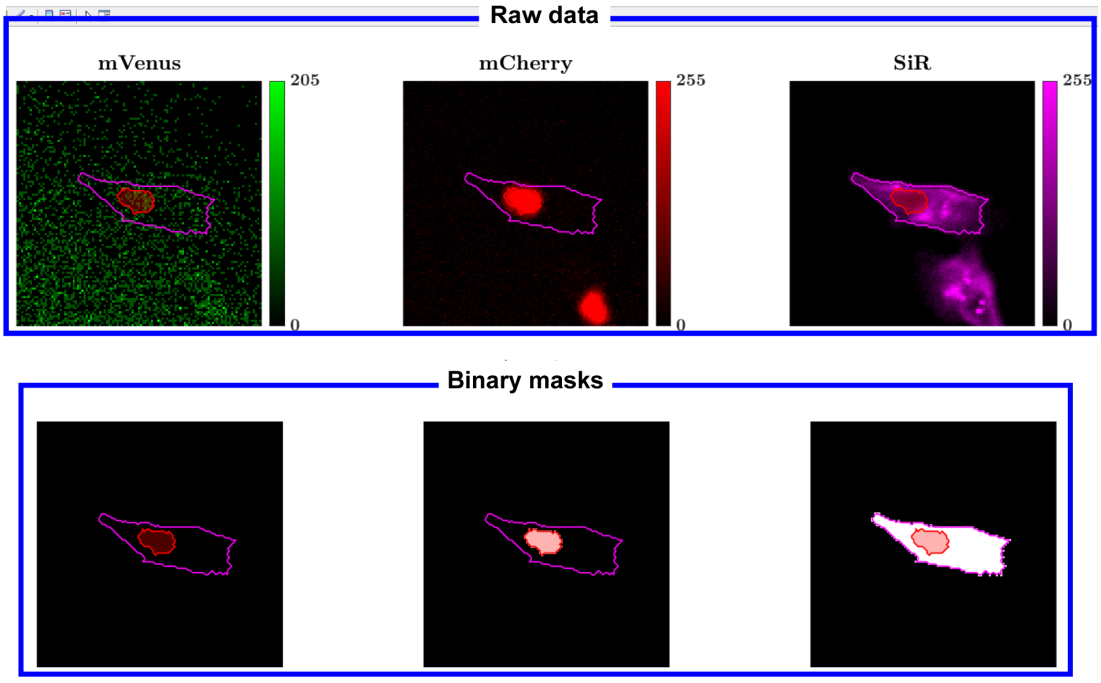

Figure 8. External window with cell shape segmentation

5.3 Segmentation & tracking – Nucleus panel

Please refer to Figure 7B to see where the options are in the GUI.

Channel

This option is to choose from which channel (red for mCherry and green for mVenus) the segmentation options described below should be applied to.

Watershed separation

If two nuclei are touching each other, FUCCItrack will run a watershed algorithm to separate them. The software picks the correct nucleus as the one which has its center of mass the closest to the cell position defined by the tracking.

Manual nucleus

This option allows the user to manually draw the nucleus in case the automatic segmentation failed.

Detect neighbor (nucleus)

This option works as "Detect neighbor (cell)". It will delete any cell nuclei previously found nearby the currently tracked cell, thus improving the automatic tracking performance.

6. Module description – Processing

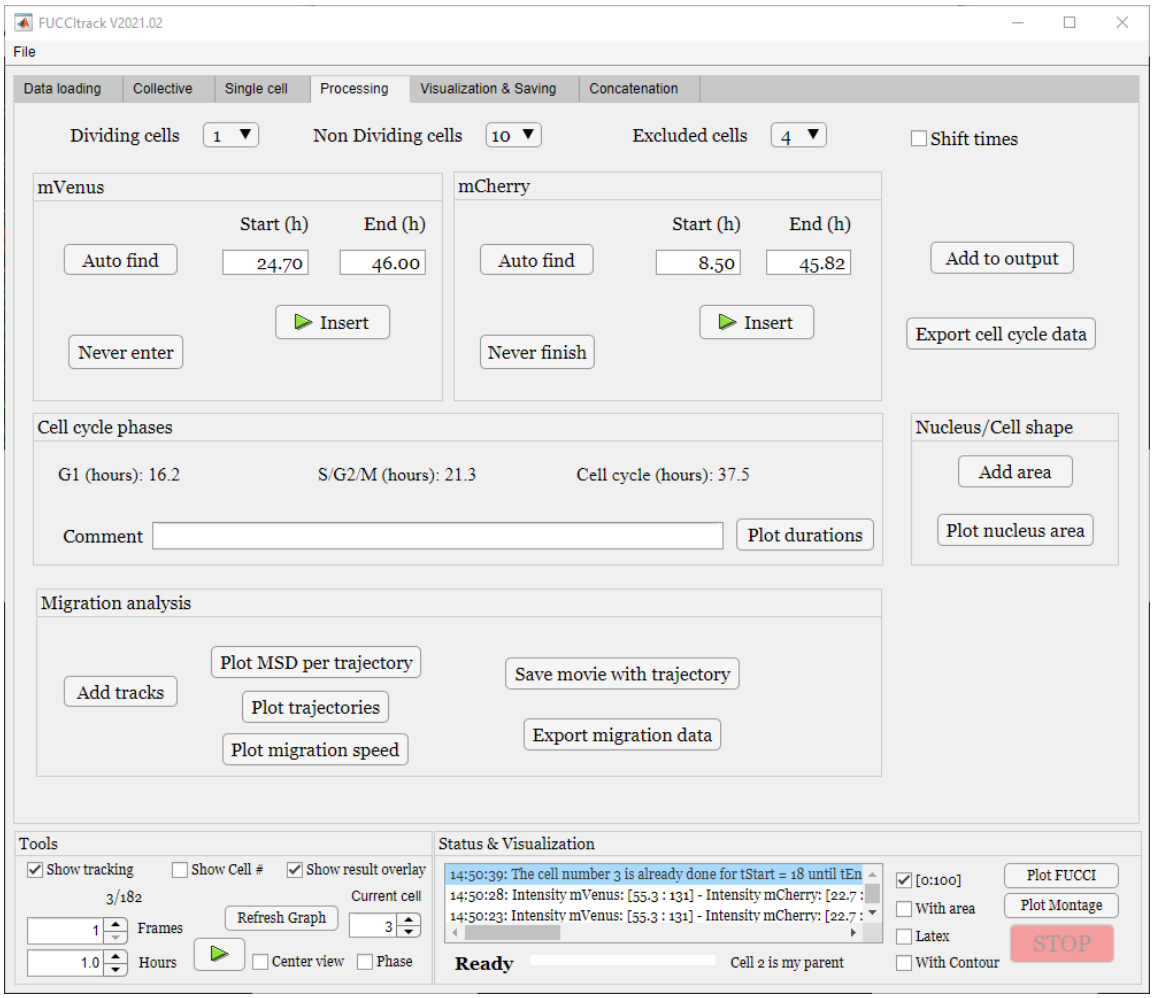

Figure 9. Processing module overview

The processing module allows user to compute and extract cell cycle phases, migration and nucleus/cell shape readouts. Users can go through the tracked cells using the "Current cell" in the Tools panel (see Fig. 12 and section 9 for more details). **It is important to not change the "Current cell" spinner while working on this module since all calculations are specific to the current cell.** Once all the readouts have been extracted for one cell, the users can change the "Current cell" spinner and procced with another cell.

Dividing cells/ Non dividing cells/ Excluded cells

This drop-down menu only summarizes the different status of cells tracked using the single cell module. Also, clicking on a cell number from this dropdown menu will have the same effect as using the "Current cell" spinner and will make the cell number selected the current cell.

Shift times

This option is used if you want to have the FUCCI/FUCCI2 intensity curves starting at 0 hour for every cell, even for the daughter cells that appeared during the experiment.

6.1 Cell cycle analysis

Both mCherry and mVenus panel have the same structure and are used to detect the beginning and end based on a threshold for the intensity defined as 5 % of the maximum intensity (this value can be modified by users).

6.1.1 mVenus panel

Auto find

This button will detect the time point when the mVenus curve goes above 5 % of its maximum intensity and assign the time stamp in the “Start (h)”. By default, it will take the last time point of the tracking as the end for mVenus and assign the time stamp in the “End (h)” field.

Insert

After using the “Auto find”, this field will stay red until pressed once. While red, it indicates that the value has not been saved in the application and users can still modify the field for the “Start (h)” and “End (h)” in case the “Auto find” failed. If the “Auto find” worked, the user will have to press on the button to save the data inside the application.

Never enter

This button can be pressed if cell stayed in G1 for the whole duration of the experiment and never had a signal for mVenus. The cell will not be excluded but considered as “non dividing cell”. It means that the cell was in the category “G1 incomplete” and never started the S/G2/M phase. The field “Start (h)” will be set to the duration of the whole experiment and “End (h)” to 0.

6.1.2 mCherry panel

Auto find

This button works similarly as in mVenus with the exception that it detects the end of mCherry when the intensity drops below the 5 % threshold value and does not take the last time point. If the curve does not go below 5 % before division, the value for the end will be defined as the minimum of the mCherry curve, but only in the range after the start of mVenus.

Insert

This works exactly like previously described and should not be forgotten otherwise the value are not saved within FUCCItrack.

Never finish

This button can be pressed if the cell started the S/G2/M phase (by passing the 5 % mVenus threshold) but did not divide within the experiment. This category of cells is called “G2 incomplete”.

6.1.3 Exporting the data

Comment

Users can write comments on the currently analyzed cell and this will be added to the exported file. For example: “Cell escapes field of view” etc...

Add to output

When the two “Insert” buttons and additional “Comment” have been added, the user can press this button to write the data into the output field that is exported.

Export cell cycle data

When the cell cycle analysis has been performed on all the tracked cells, the user can press this button to create the output files (one output file in .xlsx format and another in .mat format). The data present in this file is: cells and their parent identification number, beginning and end time of the mCherry and mVenus phase as well as the calculated t_{G1}, $t_{S/G2/M}$ and $t_{Cell\ cycle}$ in hours. It also contains the category of the cell (divided, did not divide, excluded) and the comments section that users may enter.

Plot durations

When more than one cell is tracked and the cell cycle analysis has been performed for all cells, the user can click on this button to create a boxplot with the duration of the different cell cycle phases (G1, S/G2/M and total division). The data corresponding to this plot can be seen after clicking the “Export cell cycle data” too.

6.2 Migration analysis

FUCCItrack uses the msdanalyzer package to store the migration related parameters such as trajectory, velocity and mean square displacement (MSD).

Add tracks

This button will use the tracking information and load this into the msdanalyzer class for every cell tracked. It is important to click on this button before any other in the “Migration analysis”. It also creates a “.mat” file that contains the class.

Plot MSD per trajectory

This button will compute and plot the mean square displacement (MSD) for every cell as a function of time.

Plot trajectories

This button will use the position data of every cell tracked and superpose their trajectories in a new figure.

Plot migration speed

This button will compute and plot the median of instantaneous speed over the trajectory of each cell in a boxplot format.

Save movie with trajectory

This button will create a movie containing the full trajectory of the cell (Supporting Movie 1).

Export migration data

This button will plot the other migration related metrics such as total distance, displacement and directionality in individual plots and export all of the data into an excel file.

6.3 Nucleus/Cell shape

This last panel can be used to compute and plot the nucleus projected area and the cell, if applicable.

Add area

This button will compute the nucleus area for every tracked cell and store the data inside the application.

Plot nucleus area

This button will create a new figure that contains the nuclear area as a function of time obtained by the “Add area” button previously.

7. Module description – Visualization & Saving

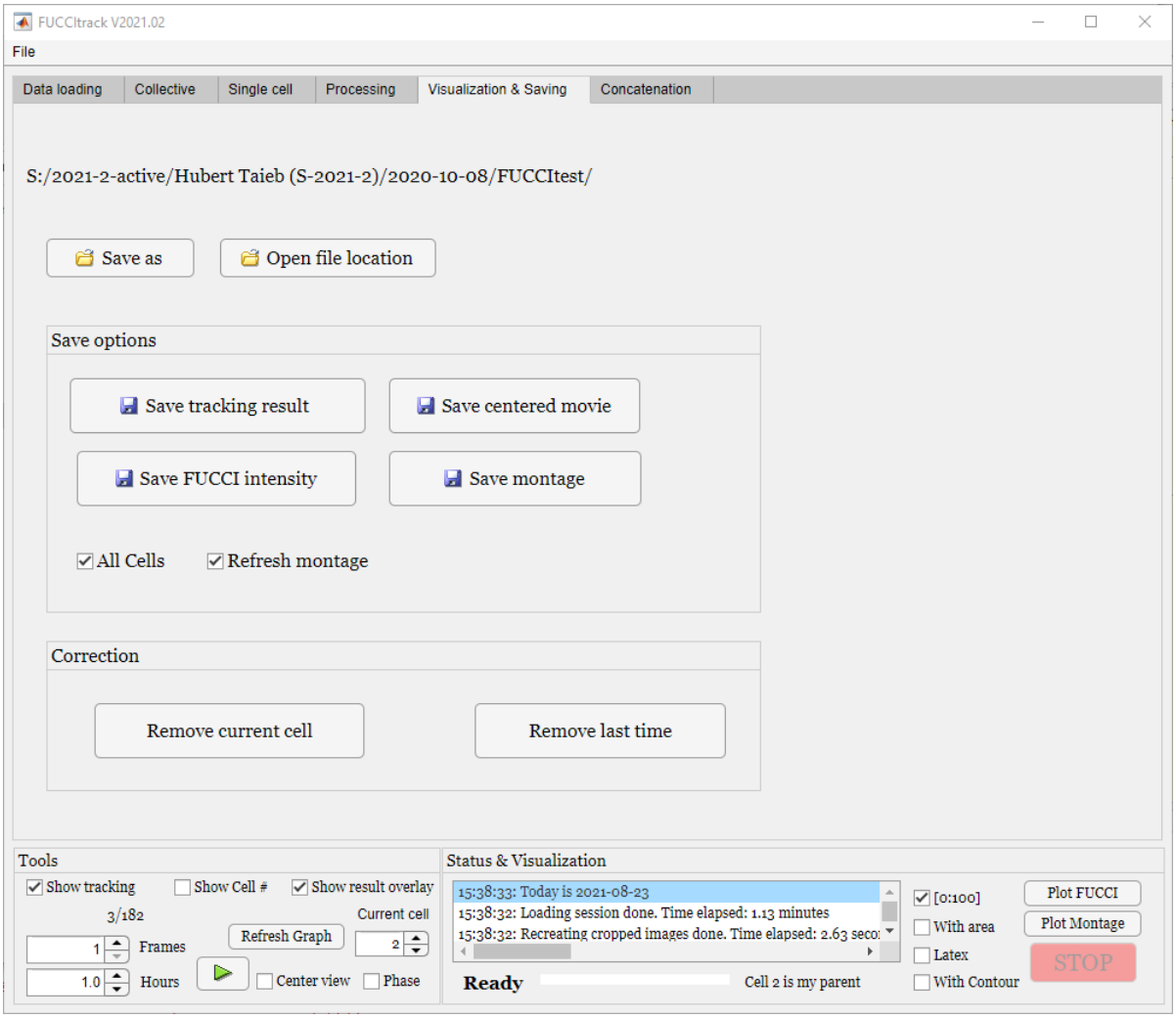

Figure 10. Visualization & Saving module

This part of the software (Fig. 10) is intended to be used to create a set of figures or movies concerning single cells.

Save as

The user is invited to select a location to save the FUCCItrack associated files ("tmp_data.mat", "im_only.mat" and "state.mat") to recreate the session in the future.

Open file location

This button opens the explorer where all the data related to this field of view is stored.

Save tracking result

This button takes a screenshot of Fig. 8 for every time point and saves this under the current cell specific folder.

Save centered movie

This button saves a movie that has the current cell centered over time during the tracking.

Save FUCCI intensity

This button will save the plots generated by “Plot FUCCI” in both pixel-based and vectorized format. In addition, the original MATLAB figure will be saved which contains the data of the intensity.

Save montage

This button will save the figure generated by the “Plot montage” button, also in both pixel-based and vectorized format. If the figure was already generated previously, then it will not recreate it, except if the “Refresh montage” option is selected.

- “Refresh montage”: this option will recreate the figure with the montage before saving it on to the computer.

All cells

If this option is selected, the saving of FUCCI intensity or montage will be done on all tracked cells instead of only the current cell.

Remove current cell

This button allows users to delete the current cell from the application data in case an error or a problem was associated with this cell.

Remove last time

This button will delete the data associated with the last time point of the currently tracked cell.

8. Module description – Concatenation

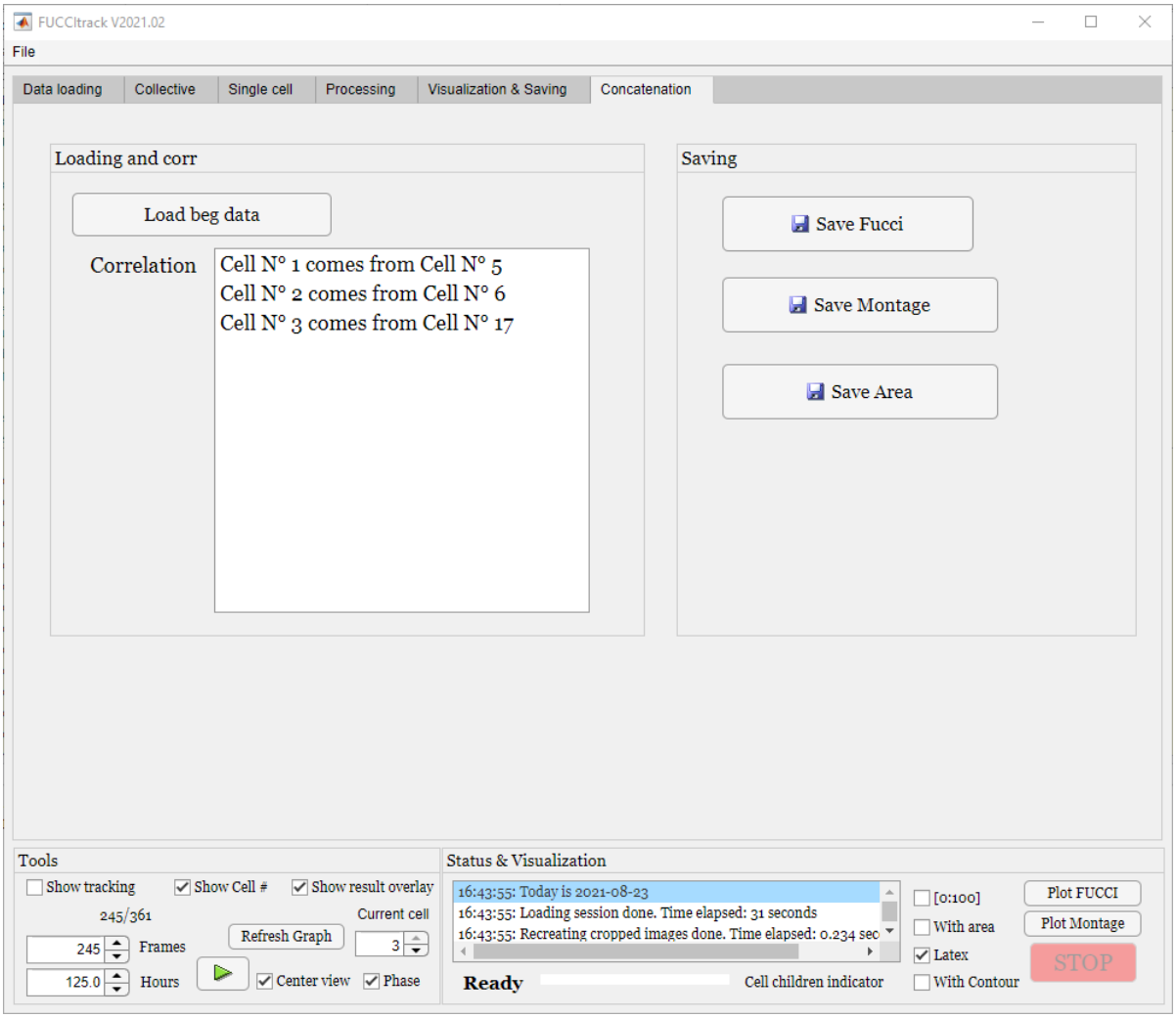

Figure 11. Concatenation module

The concatenation module (Fig. 11) is designed for users who have two set of files corresponding to the same field of view. The layout is simple and contains two main panels:

Load beg data

By clicking on this button, the data from the previous experiment will be loaded into the application.

Correlation

This is the part that links the two datasets. The line “Cell N°1 comes from Cell N°5” means that the current cell number 1 open in the current dataset is the same as the cell number 5 in the previous dataset. When the user clicks on the texts in this panel, the plots for FUCCI intensity, montage and area over time are generated.

Save FUCCI intensity

Like the processing module, this saves the FUCCI intensity with the two datasets concatenated.

Save montage

This button saves the montage across the two datasets.

Save area

This button saves the plot corresponding to the area over time from the two datasets.

9. Panel description – Tools

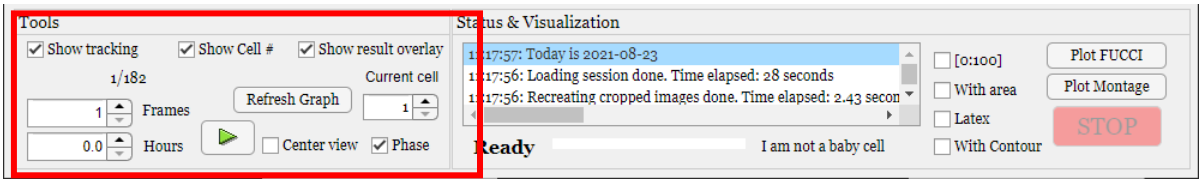

Figure 12. "Tools" and "Status & Visualization" panel

One important panel is the "Tools" panel, which is always present at the bottom of the app.

Show tracking

This option controls the visibility of the external window (Fig. 8). If the option is selected, the external window is visible, and hidden otherwise. Tracking and segmentation results process faster if this option is not selected at the cost that the user cannot follow in real time the tracking for eventual errors.

Show cell #

Figure 13. Internal visualization panel with all channels overlaid

This option will show or hide the cell number label on the internal “Visualization” panel (Fig. 13).

Show result overlay

This option will show or hide the result of the segmentation as an overlay on the raw and binary masks on the external viewer (Fig. 8, in magenta and red).

Current time point/total time point (1/182 here)

This will inform the user of the current time point and the total number of time points (here it is the first frame out of 182 time points).

Frames

This is a spinner and lets the user navigate through the time lapse by clicking on the up and down arrows. The user can also write a value directly on the text field on the left side.

Hours

This is a spinner connected to “Frames”. It translates the frame number to the actual time of experiment in hours. Users can also navigate through the time lapse by picking a specific hour or using the up and down arrows.

Play button

It will open the external window and show all time points that have been evaluated for the current cell, one by one until the end of the tracking.

Refresh graph

This button will open the external window for the current cell at its first time point. It is needed to have the external window open before using the “Run” button. The refresh graph can be useful if the current external window gets frozen during utilization by just recreating it.

Current cell

This spinner allows the user to go through the tracked cells and corresponds to the cell number or its unique identifier. It always starts at 1. While tracking a particular single cell, this spinner should always stay the same and user should not modify this during the tracking.

Center view

This option centers the internal visualization panel around the currently tracked cell instead of using the full field of view.

Phase

this option allows user to switch the internal and external viewers between phase and cell fluorescence channel if present (see Fig. 14).

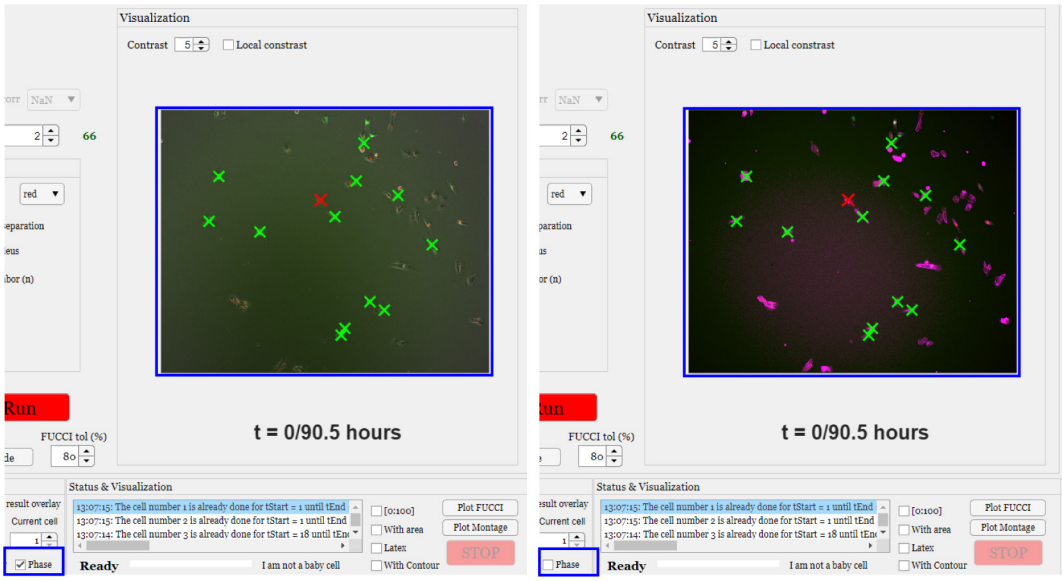

Figure 14. "Phase" option behavior**.** On the left panel, the "Phase" option is selected so that the phase contrast image is used for visualization. On the right panel, the "Phase" option is not selected, and the SiR-Actin channel is then visible.

10. Panel description - Status & Visualization

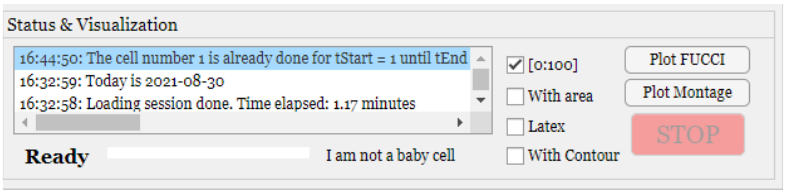

Figure 15. Status & Visualization panel

This panel contains a log field which is continuously updated (Fig. 15) . Every entry is recorded with its timestamp in the format "hh:mm:ss" to keep track of what has been done with FUCCItrack. There is also a progress bar (white at 0% and green when running) below the log field. Other fields related to status are:

Ready (or Busy)

This label field is an indicator that FUCCItrack is currently running operations in the background. When "Busy" is displayed in red, the user should wait and not click any button or perform operations.

"Cell children indicator" or "I am not a baby cell" or "Cell 1 is my parent":

This label field change its text depending on the current cell selected. The label field will be updated upon tracking and gives user the information about the lineage of the current cell in the context of the single cell tracking.

- "Cell children indicator": this is the default text when no single cell tracking data exists.
- "I am not a baby cell": this will be displayed if the current cell was added by the "Seeding cells" button, with no information about its parent cell.
- "Cell XX is my parent": this will be displayed (with the actual number XX depending on the experiment and current cells) when the current cell was added by the "Seed daughter cells" button, since the origin of the cell can be traced back to its parent.

The "Status & Visualization" panel also contains button and options to create two important plots: the FUCCI intensity and the montage of nucleus over time (Fig. 16).

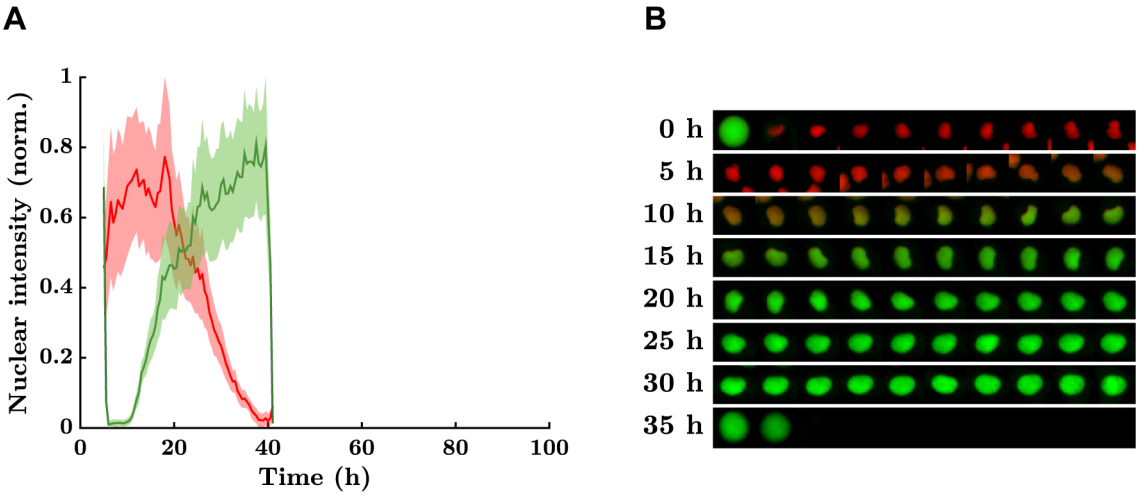

Figure 16. FUCCI intensity curves and corresponding nucleus montage.

Plot FUCCI

This button will create a new graph with the FUCCI intensity curves of the current cell (Fig. 16A). Two related options can be used before clicking on this button:

- "[0:100]": this defines the limits of the x axis (in hours) for visualization the FUCCI intensity curves. It is recommended to use this option if you want to compare FUCCI intensity curves belonging to different cells. If unselected, FUCCItrack will automatically determine the limit in hours corresponding to the current cell. The upper boundary can be modified by the user if necessary.

- "With area": when this option is selected, the FUCCI intensity plot will contain a second y axis on the right depicting the projected area of the current nucleus over time.
- "Latex": this option allows users to have latex style writing for all visualization plots. If not selected, the default font will be arial.

Plot montage

This button will create the figure corresponding of the concatenation of the nuclei of a cell over time (Fig. 16B). If the option "With contour" is not selected, then only the mCherry and mVenus channel will be visible. But if "With contour" is selected, the cell shape channel will also be present in the montage.

STOP

This button enables users to stop several functions of FUCCItrack while running. For example, if the tracking is started for 20 time points but it fails at an earlier time point, then user can press "STOP" and apply corrections.

11. Saving FUCCItrack associated data and state

FUCCItrack works with sessions that allows users to work on it, save it for later and reopen the application exactly where they left.

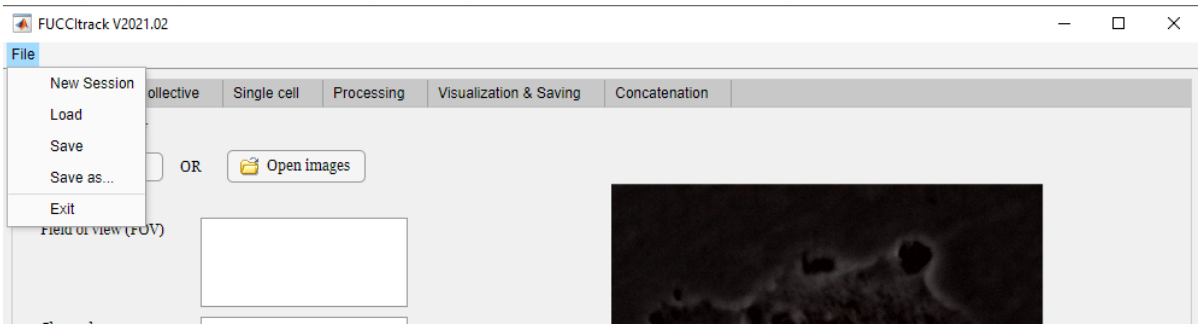

Fig 17. The File menu

New Session

This will reset the application to when the user opens it. Do not forget to use the "Save" button before clicking on this since all the data will be lost otherwise.

Load

The users will be invited to open the "tmp_data.mat" file of a previous session to load everything back to its saved state.

Save

This button will save the 3 associated MATLAB files (“tmp_data.mat”, “im_only.mat” and “state.mat”), the files contain the necessary information for reloading the application as well as all the raw, tracking and segmentation data.

Save as ...

This button allows users to move all the MATLAB associated files to another location if needed.

Exit

This button terminates the software and closes it.

Appendix B

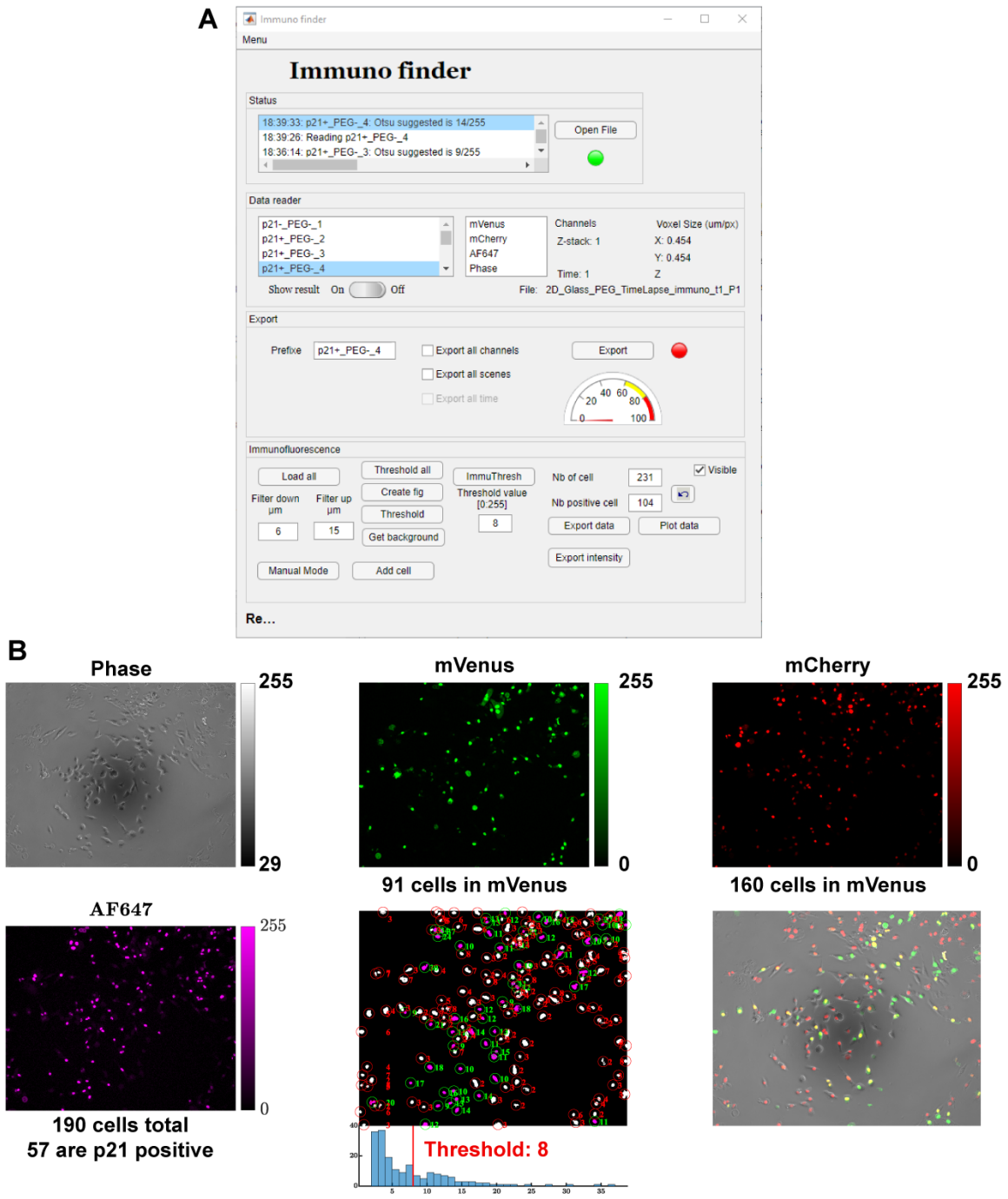

Appendix B. ImmunoFinder – a software to quantify immunofluorescence data. (**A**) Graphical user interface developed to work with immunofluorescence images along with FUCCI2. (**B**) External figure showing the nuclei segmentation with mVenus and mCherry as well as the counting of p21$^+$ cells.